AN INTEGRATED COMPUTATIONAL FRAMEWORK FOR THE ACCELERATED DEVELOPMENT OF TAILORED ADDITIVELY MANUFACTURED METALS

A Dissertation

by

MEELAD RANAIEFAR

Submitted to the Graduate and Professional School of
Texas A&M University
in partial fulfillment of the requirements for the degree of

DOCTOR OF PHILOSOPHY

Chair of Committee,	Raymundo Arróyave
Committee Members,	Edwin J. Schwalbach
	Ibrahim Karaman
	Alaa M. Elwany
	Patrick Shamberger
Head of Department,	Ibrahim Karaman

May 2022

Major Subject: Materials Science & Engineering

ABSTRACT

Additive manufacturing (AM) is a disruptive technology leveraging innovations of the past and present to enable the design and fabrication of the new standard for components across industries. However, the successful application of the AM process to achieve desired results is in part made possible through the exploitation of inherent material properties and characteristics. Consequently, this process-structure-property-performance relationship must be understood and leveraged within AM to reliably and effectively continue development for improved performance through materials design. The improved performance and functionality of AM components thus necessitates a framework for accelerated materials design and development. For this purpose, a physics-based and data-driven integrated computational materials engineering (ICME) framework is developed, leveraging the utility and efficiency of simulations with experimentation to drive forward materials design and discovery. This is achieved by querying the complex AM PSPP relationships to inform and guide experiments for the cost-effective design of NiTi-based shape memory alloys (SMAs).

In this regard, NiTi-based SMAs are prone to Ni loss under the conditions afforded by the AM process and are subject to a strong correlation between Ni content and transformation temperature (TT). Additionally, these materials suffer from difficulty in fabrication through standard manufacturing processes while exhibiting desirable functional properties. For this reason, the first study of this work takes a critical inspection on the vaporization of alloys during the welding and AM process. This is followed by a second study where an ICME framework consisting of a thermal model, a multi-layer model, and a differential evaporation model, is developed to screen for PSPP trends and inform experiments for the laser powder bed fusion (LPBF) AM of metal alloys. This framework is calibrated and validated against experiments for NiTi SMA, utilizing process parameters to predict Ni content and TT in agreement with experimental measurements and trends. The third study leverages optimization techniques alongside the ICME framework to solve the inverse design problem and predict design parameters required for desired component specifications. The fourth study expands the utility of the framework to the NiTiHf system where, after calibration and validation, model predictions for TT were found to be in good agreement with experiments. The fifth study provides a summary of the work and its contributions towards the accelerated development and design of LPBF AM metals, as well as an outlook on future work for expanded utility and application of the ICME framework.

ACKNOWLEDGMENTS

I would like to thank my advisor Raymundo Arróyave for advising and supporting me towards the development of this work. I would also like to thank my committee members Alaa Elwany, Ibrahim Karaman, and Patrick Shamberger for their support and feedback. This work was also made possible by the mentorship and contributions provided by Edwin Schwalbach, enabling the adaption of the thermal model as part of the model framework. Further, I would like to thank Pejman Honarmandi for all of the encouragement, advice, and contributions towards this dissertation.

I would also like to thank my peers for their input and knowledge, helping me grow and learn over the course of this work. I owe special thanks to Daniel for dedicating so much time towards teaching myself and others recommended practices for programming and helping me build the groundwork needed to succeed in computational research. This goes as well for Richard and Tanner who were always willing to help answer any of my computational and programming questions.

My family, friends, Jess, thank you for being there, helping me through the challenges, and celebrating the triumphs. This has been quite the journey, and I'm glad for you and all those who joined me along the way.

CONTRIBUTORS AND FUNDING SOURCES

Contributors

This work was supported by a dissertation committee consisting of Dr. Raymundo Arróyave (advisor), Dr. Ibrahim Karaman, and Dr. Patrick Shamberger of the Department of Materials Science & Engineering, Dr. Alaa Elwany of the Department of Industrial and Systems Engineering, and Dr. Edwin Schwalbach of the Air Force Research Laboratory Materials and Manufacturing Directorate.

The thermal model adapted in Chapter 2, Chapter 3, and Chapter 4 was provided by Dr. Edwin Schwalbach of the Air Force Research Laboratory. The thermal model calibration in Chapter 2 and Chapter 4 was conducted by Dr. Pejman Honarmandi of the Department of Materials Science and Engineering. The differential evaporation model calibration in Chapter 4 was conducted by Jiahui Ye of the Department of Industrial and Systems Engineering. The experimental work in Chapter 2 and Chapter 4 was conducted by Lei Xue and Chen Zhang of the Department of Materials Science and Engineering and the Department of Industrial and Systems Engineering, respectively.

All other work conducted for the dissertation was completed by the student independently.

Funding Sources

Graduate study was supported by a College of Engineering fellowship from Texas A&M University (TAMU) and the Air Force Research Laboratory (AFRL) through the AFRL/TAMU Data-Enabled Discovery and Design of Materials (D^3EM) Minority Leadership Program, under subcontract No. UTC-165852-19F5830-19-02-C1. Portions of this research were conducted with the advanced computing resources provided by Texas A&M High Performance Research Computing.

TABLE OF CONTENTS

Page

LIST OF FIGURES

FIGURE Page

LIST OF TABLES

1. INTRODUCTION

1.1 Overview

Additive manufacturing (AM) plays a pivotal role in the future growth of industries by providing a means for the rapid fabrication of components with complex geometries, less waste, and improved performance. However, the complex process-structure-property-performance relationship (PSPP) of AM materials must be further understood to fully realize AM's potential. Of particular interest is powder-based AM, where the application of a heat source enables the welding of abutting metallic species, contributing to the unresolved phenomena of vaporization of alloying elements from the melt pool and associated changes in properties. This chapter is a critical inspection of information on the vaporization of alloys and their elements due to the fabrication process. Being that AM is essentially a more complex extension of the welding process, sources from both fields are examined in this endeavor. Both experimental and theoretical results are investigated with focus maintained on vaporization, key processing parameters, and associated composition change in alloys. Numerical models for transient temperature and velocity field profiles, used for vapor flux and mass loss calculations, are also inspected. It is then shown that laser power, speed, and the properties of the alloying elements are determinants of vaporization and can have a significant effect on the composition of an additively manufactured material. This is followed by an outlook on future work, resolutions to current issues involving the vaporization of alloying elements in additive manufacturing, and a justification for the improved comprehension of the vaporization process in regards to the progressive development of structurally tailored metallic materials in additive manufacturing and the ensuing PSPP relationship.

1.2 Introduction

As technological advancements further the integration of data and machine learning with manufacturing tools and processes, additive manufacturing (AM) sits at the forefront of development in materials design. Additive manufacturing has taken complex designs and streamlined their fabrication into a single step process, where a digital model is referenced to construct components layer upon layer and can be applied towards the development of a variety of materials ranging from metals to polymers to composites [1, 2]. Although AM has come a long way in the pat several decades, only recently growing in popularity, it has found its place as a tool to save time and money across industries through the expedited production of difficult to fabricate and higher performing fit-for-purpose parts. However, AM faces a series of challenges before it can be leveraged to its fullest potential. These challenges can be largely attributed to a lack of understanding of the complex process-structure-property-performance (PSPP) relationships inherent to the AM process and materials design space, resulting in defects, inconsistencies across builds, and hurdles in the application of AM for high-risk systems. In turn, this field warrants further investigation and development for the accelerated design and development of additively manufactured materials.

One important avenue of focus is on the development of AM metallic components due to their high demand and utilization compared to other materials [3], as well as their application for critical structural and functional materials for the biomedical, automotive, and aerospace industries [4]. These industries seek to utilize AM towards a solution for the inverse design problem, expediting the production of reliable fit-for-purpose parts, however, the expansive design space and complex PSPP relationships afforded by AM does not make this an easy or readily achievable task. Also a contributing factor is limitations on the printability of metallic alloys, dependent on material chemistry, feedstock, sufficient fusion, scan strategy, and part geometry [5]. This also corresponds to issues involving the formation of common defects such as residual stress, solidification cracking, lack of fusion, delamination, composition change, and porosity [2, 3, 5, 6].

By improving the clarity and understanding of processing parameters and their respective relationship with the structure of materials, significant advancements can be made in the AM process and promote the controlled fabrication of enhanced materials. Although a direct and brute force experimental approach may lead to solutions, a more efficient means for accelerated material design and development can be achieved by leveraging experimentation with computational modeling to provide a solution to the forward PSPP problem. This physics-based and data-driven integrated computational engineering framework (ICME) would enable the rapid screening of PSPP across a variety of materials and could be used to inform and guide experiments for expedited materials design. In combination with optimization tools, a systematic and efficient solution to the inverse design problem could also be realized.

As part of the development of an ICME framework, an understanding of the physical processes underlying AM is required to provide adequate background knowledge for the accurate representation and integration of required physics. Numerous models of ranging fidelity presently exist to model various aspects of the AM process, however one physical process inherent to the AM process, only recently gaining attention yet critical to the PSPP relationship of numerous metallic components, is differential evaporation. Differential evaporation can bring about compositional changes, influencing the structure and properties of a part on a location-specific level. Significant and uncontrolled vaporization can result in reduced tensile strength, fatigue strength, corrosion resistance, loss of strain hardened structure, and porosity [7, 8]. Additionally, this reinforces the complexity of AM and corresponding phenomena where the adjustment of a single processing or material factor involved in AM can cause deviations in fabrication and changes in the structure and properties of a part. Furthermore, due to similarities in processing conditions, the rich history of welding literature provides a fruitful and beneficial resource that can be leveraged towards the understanding of PSPP relationships in AM.

1.2.1 Motivation

There is a knowledge gap in the understanding of underlying mechanisms inherent to the AM process due to the wide variations of process parameters for material systems, variations in material properties, and variations in the printability feedstock, resulting in inconsistencies and lack of control over the structure and properties of fabricated parts and making them unreliable components for high-risk systems [9]. In this regard, the vaporization of alloying elements during the AM process is one of the prominent mechanisms causing variation in the quality of AM parts and must be further studied [7–11].

This is reinforced by Moon and Metzbower and their examination of the PSPP relationship of welded aluminum 5456 [7]. They discovered diminished properties in the welds, as compared to the base metal, due to the evaporation of magnesium, the consequent reduction of strain-hardened structure, and the formation of porosity. Similar findings were made by El-Batahgy and Kutsuna for aluminum alloys 5052, 5083, and 6061, and by Cieslak and Fuerschbach for aluminum alloys 5456 and 5086 [10, 11]. Figure 1.1 shows that the loss of volatile components results in a change in the composition of the weldment [12]. This affects weld properties, and is a severe problem that can be related to the fabrication of many important engineering alloys in AM.

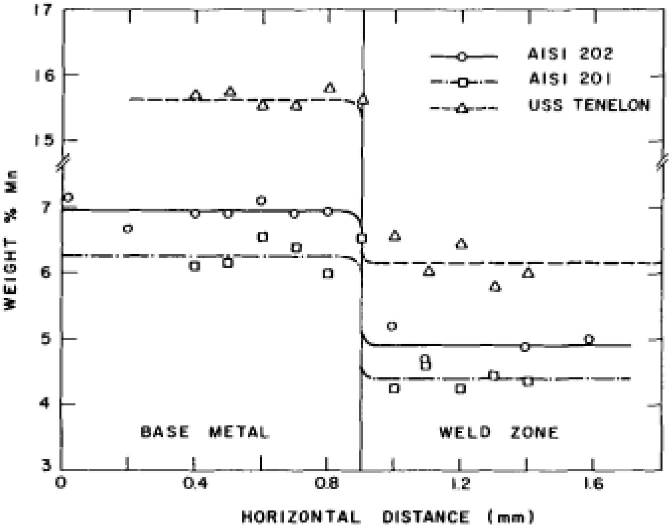

Fig. 1.1. Weight percent manganese in the base metal and weld zone of AISI 201, AISI 202, and USS Tenelon stainless steel. Parameters: Laser power – 560 W; Welding speed - 3.5×10^{-3} m/s; Shielding gas flow rate - 1×10^{-4} m^3/s; Sample thickness - 7×10^{-4} m (reproduced with permission from [12]).

Vaporization, imperfections, and associated variations in the properties of AM components could then correlate to the reduced reliability, reduced quality, and reduced service life of components, significantly impacting the development and production of components for the automotive, aerospace, and medical industries [7, 13]. It is important in these industries that a component developed through AM is capable of consistent high-performance. For AM to continue its relevance in the industry, its mechanisms, the role of vaporization, must be understood and controlled. This comprehension of

PSPP relationships will provide insights into how vaporization affects the performance, service life, reliability of AM components, and how vaporization can be leveraged to control location-specific properties for the improved and reliable performance required by high-risk industries [2, 9, 14].

By mapping the vaporization of a part through the AM process, resulting changes in structure and properties can be linked to process parameters. Once the relationship between laser power, scan pattern, scan speed, and alloy properties is established, then enhanced control of the AM of a part can be achieved. As well as advancing the aerospace industry, an understanding of vaporization could also aid the electronics industry in the processing of components in a cleanroom environment. By constructing an informed input and path strategy to minimize the evaporation of alloying elements, contamination of parts can be reduced, properties improved, and production benefited [15]. In essence, with the comprehension of vaporization mechanisms and subsequent application towards the development of pre-planned scan strategies, compositional changes caused by the vaporization of alloying elements can be exploited as a tool to manipulate and drive change for designable and controllable material properties.

1.2.2 Objective

The purpose of this chapter is to provide an understanding of the fundamental mechanisms of vaporization and its contribution to the process-structure-property-performance relationship of metallic components fabricated through AM. This is achieved through an extensive review of vaporization: the contribution of key mechanisms towards the development of vaporization, heat transfer and fluid flow, experimental measurement of vaporization, modeling of vaporization contributions, expulsion, and the effect of parameters such as laser power, scan speed, and material properties. Along with an assessment of the current state of the field, disparities in scientific knowledge and necessary research for an improved understanding of vaporization in the AM of metallic components are presented.

1.3 The Origin of Vaporization

Vaporization encompasses both evaporation and boiling, where evaporation can occur at all temperatures, but only at the surface, and boiling occurs only at a specific temperature when the vapor pressure of the substance is equal to the atmospheric pressure [16]. In multi-component alloy systems, the total evaporation rate can be described through the sum of the evaporation rate of alloying components, discussed further in Section 1.4.2. During the powder-based fabrication of additively manufactured metallic parts, extreme temperatures resulting from the application of an energy source can result in unassailable vaporization of volatile alloying elements from the melt pool [12, 15, 17–25]. In order for evaporation to occur at the melt pool, the thermal motion, kinetic energy, of the molecules must overcome the surface tension and proceed to enter the surrounding environment, where they form a vapor plume [26]. With the exit of these higher kinetic energy molecules from the system, the average kinetic energy of the system is reduced, and evaporative cooling takes place. If enough energy is applied to the system, the vapor pressure can become sufficiently large enough for bubbles to form and for boiling to occur. It should be noted that the temperature at which vaporization occurs for a material is dependent on the material's properties along with the environment. This means that a higher atmospheric pressure results in a higher boiling temperature due to the requirement of higher vapor pressure from the system needed to match the atmospheric pressure. Consequently, working in a vacuum, with shielding gas, or at varying elevations could affect vaporization and the associated compositional change that occurs during the AM process. This further contributes to the importance of determining accurate thermal histories for fabricated parts, since vaporization and its influence on structure and properties are dependent on temperature.

1.3.1 Heat Transfer and Fluid Flow

The application of a heat source, to weld adjoining elements, is a cornerstone in the powder-based fabrication of AM metallic parts. Figure 1.2 provides a schematic for AM process where the laser provides a heat source which follows a scan path and provides a spatially varying thermal output. In turn, this results in variations to the melt pattern and the corresponding solidification and cooling for each point in the part [5, 27]. These uncontrolled variations, stemming from the thermal history, are part of what leads to the failure and undesired outcome of AM metallic parts, and can be detrimental for highly specialized parts such as those used in the space industry and aeronautics [9]. However, this scenario can be controlled through the insightful application of knowledge towards adjusting input parameters during the AM process. If input parameters and the alloying elements are understood, then the resulting microstructures, melt pool geometries, and print quality could be linked to a set of parameters and an ideal AM fabrication strategy to achieve a desired design specification could be formulated.

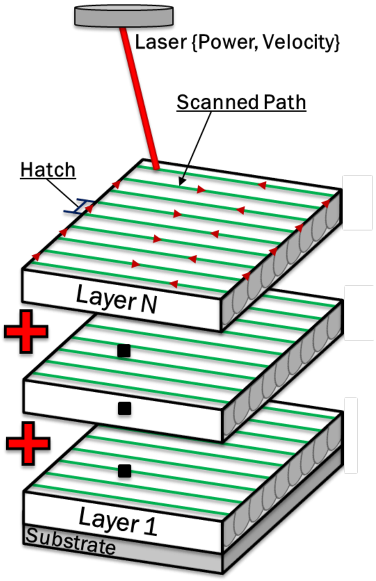

Fig. 1.2. Sample schematic of a laser powder bed fusion additive manufacturing process, consisting of multiple layers, the application of a laser as an energy source, and a snaking scan strategy.

When analyzing the thermal cycle during fabrication, one could first consider the energy source to be a stationary point source. As the energy source comes into contact with the metal powder, the heat applied to the localized area will result in a melt pool, subject to a sufficient quantity of supplied energy based on the material's properties. From here, heat will be conducted throughout the part. The rate and magnitude at which this heat spreads through the part are dependent on material properties such as thermal conductivity and absorptivity, resulting in a thermal gradient [28]. Displayed in Figure 1.3 is an example of a melt pool, where the most extreme temperature is located directly underneath the heat source [29].

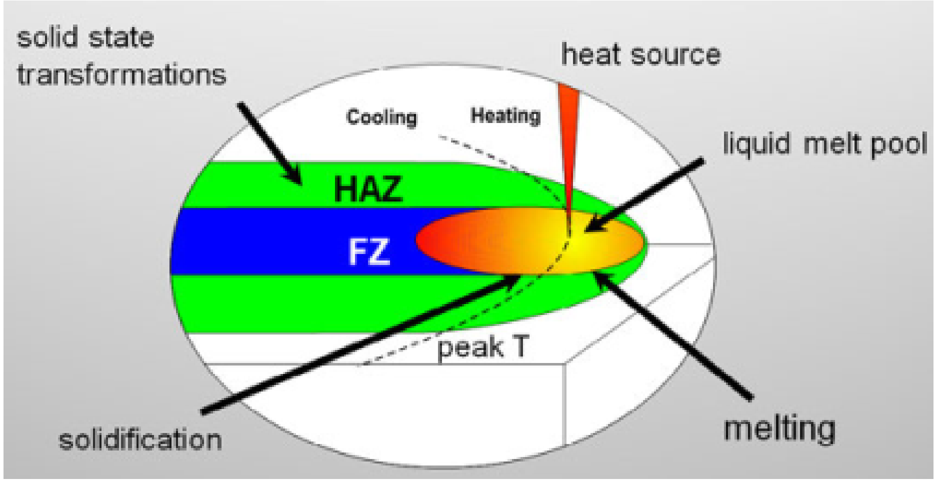

Fig. 1.3. Representation of a localized melt pool formed by a moving heat source. The front and sides of the pool experience melting, while solidification and solid-state cooling transformations occur at the back. This creates the fusion and heat affected zone (FZ, HAZ, respectively) (reproduced with permission from [6]).

As the metal is heated, low heat conduction between layers and rapid heating of the top surface of a part lead to the formation of a steep thermal gradient [28, 30]. The region directly underneath the energy source will experience peak temperatures, and temperatures will steadily decrease as the energy source moves past. Based on factors such as the specific location on the part, the laser speed, layer number, and hatch distance, a unique and complex thermal cycle of the part will form. Depending on these process and material parameters, the fabrication process produces a wide range of temperatures, making it possible for a single layer to experience multiple phases and different magnitudes of evaporation and boiling.

1.3.1.1 Expulsion

Tied together with vaporization and corresponding changes in composition is the expulsion of liquid metal from the melt pool. Basu and Debroy experimentally and theoretically studied the parameters for starting the liquid-metal rejection during laser processing. They proposed that if the vapor recoil force, F_r, exceeds the surface tension force of the liquid metal at the periphery of the melt pool, F_s, liquid expulsion takes place [15, 31]. This relationship can be described by:

$$F_r = 2\pi \int_0^{r_B} r\Delta P(r)\mathrm{d}r \tag{1.1}$$

and

$$F_s = 2\pi r_0 \sigma \tag{1.2}$$

where r_B is the radial distance that the surface attains boiling temperature. Dependent on the radial distance from the beam axis, $\Delta P(r)$ is the variance of local equilibrium vapor pressure with the atmospheric pressure, r_0 is the radial distance for the melting temperature, and σ is the corresponding surface tension coefficient. Figure 1.4 illustrates this relationship between surface tension and recoil force for a study on stainless steel [15].

Here the recoil force begins to exceed the surface tension of the melt pool at a time of approximately 1.4 ms through a 3 ms laser pulse, enabling expulsion. In AM this can be a compounding effect for each layer, also considering that the molten projectile may land elsewhere on the working layer and further contribute variations in composition.

1.4 Vaporization of Metal Alloys in Additive Manufacturing

Due to the complexities of the AM process, there is great variation in the thermal history across the layers and specific locations within the layers which comprise a fabricated component [32]. Figure 1.5 illustrates the AM process and a sample thermal history for two separate points. A point at the middle of the track in green, and a point at the end of a track in blue. Each point will

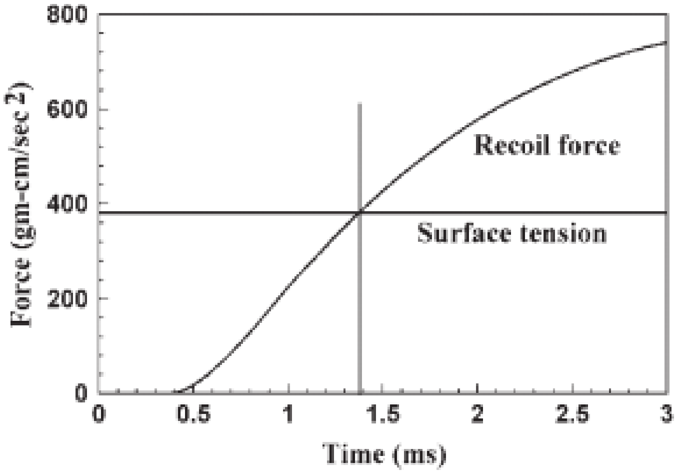

Fig. 1.4. Relationship between recoil force and surface tension as a function of time. Laser power – 1067 W; Pulse duration – 3.0 ms; Beam radius – 0.225 mm (reproduced with permission from [15]).

experience different heating and cooling, where a point at the end of the track will have direct heating and a short pause before it is reheated as the laser starts on the next track, giving it a second slightly higher peak that may experience more evaporation compared to a point at the middle of the track, where there is a long gap between the direct and adjacent laser passes which allows for extended cooling at the point. This is important because vaporization is tied with temperature, so each point may experience different amounts of vaporization, and the associated chemistry change.

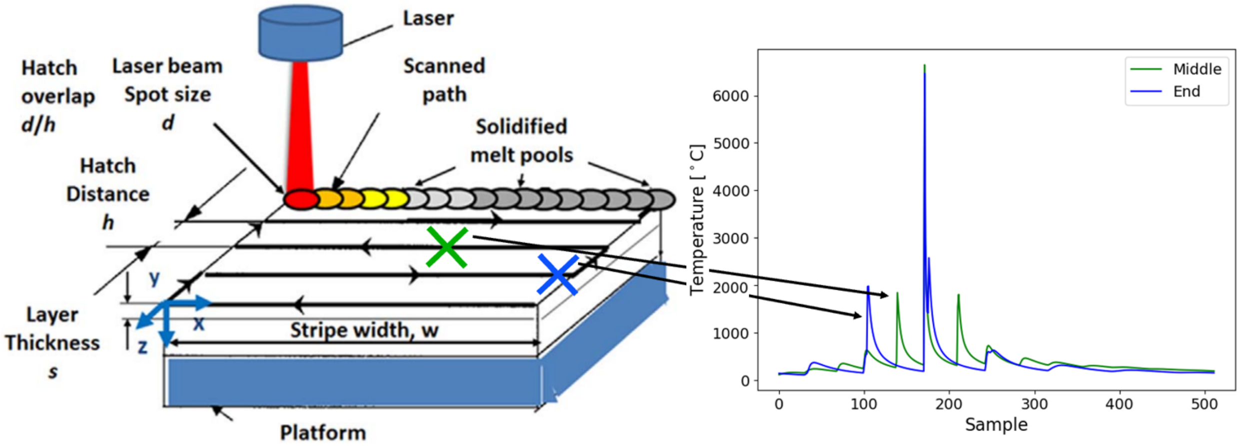

Fig. 1.5. Left: Diagram of AM process (reproduced with permission from [32] (with alterations)). Right: Sample thermal curve for points at the middle and end of track

However, the measurement of the vaporization and chemistry change that occurs at each point and each layer during fabrication is a difficult task. The degrees of freedom allowed during the AM process pose a problem for in-situ measurement, leading to the utilization of indirect measurement techniques. Modeling techniques to predict vaporization have also been established to aid in estimating the chemistry change a part experiences.

1.4.1 Experimental Measurement

For a better understanding of the vaporization that occurs in a fabricated part during AM, accurate experimental measurements are required. Experimental measurements accounting for the weld geometry and mass loss of a material can be achieved through several methods. Matthews et al. used a setup consisting of a high-speed camera, microscope optics, and a bandpass filter to capture the melt pool formation [19]. The melt pool depth and width can also be determined by taking several collinear welds and measuring their longitudinal cross-sections, by optical microscopy [33]. For calculating mass loss, one method calls for the placement of a quartz tube over the sample and having the laser beam focus on the material within the exposed portion of the tube. Vaporized elements will gather against the interior of the tube as condensation, which can then be measured by an electron microprobe x-ray analyzer. This works well for laser pulse processing, however, the degrees of freedom of AM would not allow for a quartz tube to continuously encompass the laser and capture meaningful results to describe vaporization and composition change throughout the build.

Weight measurements can also be taken of the sample before and after welding to compare and account for the mass loss of the material [34]. However, unless this is for a pure metal, additional tools would be required to determine the composition loss of specific alloying elements. In regards to AM, using weight measurements to determine mass loss is infeasible. However, an experiment could be designed to re-melt a pre-determined contour multiple times, in order to produce a quantifiable mass loss [35]. This information can then be used to estimate the vaporization and mass loss for a single path scan. In another case, He and DebRoy used an electron microprobe to determine the concentration of alloying elements in stainless steel across the radial path of the melt pool [20]. For calculating the vaporization rate, the interaction time of the laser and material surface could be recorded with an electric chronometer [22]. However, in experiments, there is still difficulty in getting accurate and consistent readings of the transient temperature profile associated with a moving energy source. One potential issue could be the plasma surrounding the relatively small-sized melt pool, creating difficulty in taking direct and dependable temperature profile measurements due to interference [12]. Figure 1.6 depicts vaporization through the laser processing of shape memory alloy (SMA) NiTi [36]. In section ‘a,’ it is shown that the base content of nickel, approximately 50.07 atomic percent, is reduced to approximately 48.36 atomic percent in the processed region, with the vapor plume containing 75.5 and 24.5 atomic percent nickel and titanium, respectively. These measurements were attained by placing a quartz tube co-axial to the incident beam and analyzing the chemistry with a scanning electron microscope equipped with an energy dispersive x-ray analysis aperture. Seen in section ‘b,’ the processed region also experienced a structural change from austenite to martensite, and section ‘c’ shows that Ti_2Ni precipitates were also found in this region due to the insolubility of Titanium in the Nickel depleted region. The change composition and formation of precipitates result in different transformation temperatures for the sample and altered performance.

1.4.2 Modeling

Industries wishing to take full advantage of what AM has to offer require increased comprehension of influential processing elements and the ability to leverage PSPP relationships toward the consistent fabrication of reliable and cost-effective components [2]. A method to predict vaporization in a fabricated part would aid in this endeavor by providing values and allowing analysis of the part that could not be easily achieved otherwise. However, due to difficulties with in-situ measurements, the modeling of heat transfer and fluid flow phenomena of material during AM are required for further analysis of the parameter-structure relationship [37]. These models are essential to aid in the measurement of material defects and compositional change by providing quantitative and visual representations of the development of a part. By comparing experimental and computational information, trends such as a decreasing temperature of the melt pool with increasing

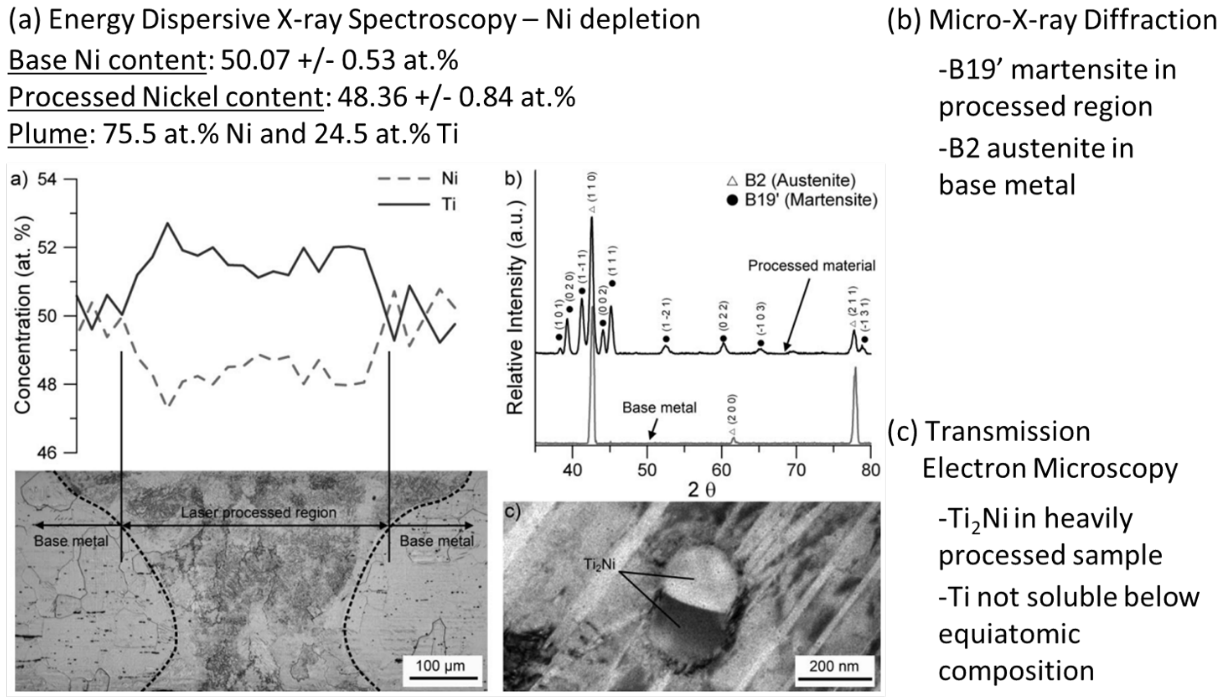

Fig. 1.6. Experimental results for laser processed SMA NiTi (reproduced with permission from [36] (with alterations)).

radial distance from a laser, increasing melt pool depth with increasing energy and decreasing feed rate, increasing recoil force with increasing temperature, and increasing vaporization rates with increasing temperature have been verified [12, 24, 27].

Computational measurements must then consider numerous parameters when modeling the heat and fluid flow during AM to improve accuracy and enable the prediction of the parameter-structure relationship, followed by validation with experimental measurements. Figure 1.7 illustrates an energy input and the variety of phenomena that must be accounted for at the melt pool to ensure an accurate heat and fluid flow model.

For this reason, there are several approaches for modeling heat and fluid flow in AM, to aid with calculations for vaporization rate and composition change. These techniques range from low fidelity to high fidelity, as shown in Table 1.1, and may be chosen based on factors such as required accuracy, time, and cost.

By utilizing low fidelity analytical methods, measurements can be made quickly and easily,

Table 1.1. Methods and characteristics of heat and fluid flow models in AM (adapted from [6]).

Method	Characteristics	Refs.
Analytical	Simplifying Assumptions → Faster calculations → Less expensive/accurate Implements → Rosenthal's heat conduction equation Returns → Temperatures → Cooling rates → Workpiece dimensions	[38, 39]
Finite Element Method – Heat Conduction	Neglects convective flow in the melt pool → Easy implementation → Not too accurate Implements → Equation for convective and radiative boundary conditions for steady-state or transient energy conservation Returns → Workpiece dimensions → 3D steady-state or transient temperature distribution	[40]
Finite Difference Method – Heat Transfer and Fluid Flow	Simplifying assumptions → Flat melt pool surface Considers the effects of melt pool flow → Accurate temperature distribution Implements → Equation for 3D transient conservation of energy, momentum, and mass Returns → Workpiece dimensions → 3D velocity or transient temperature distribution → Solidification parameters	[41, 42]
Level Set Method (LSM)	Intensive computations, non-conservation of mass → Good agreement with experiments Implements Tracking of the melt pool's free surface Returns → 3D velocity and temperature distribution of the mass with a free curved surface	[43]
Finite Difference Method - Volume of Fluid	Similar to LSM, but the mass is conserved	[44]
Lattice Boltzmann Method, arbitrary Lagrangian-Eulerian	Intensive computations → Modeling of particle kinetics and velocities for 2D and 3D methods Implements -Free surface boundary conditions Returns → Melt pool geometry → Predicts build geometry	[45]

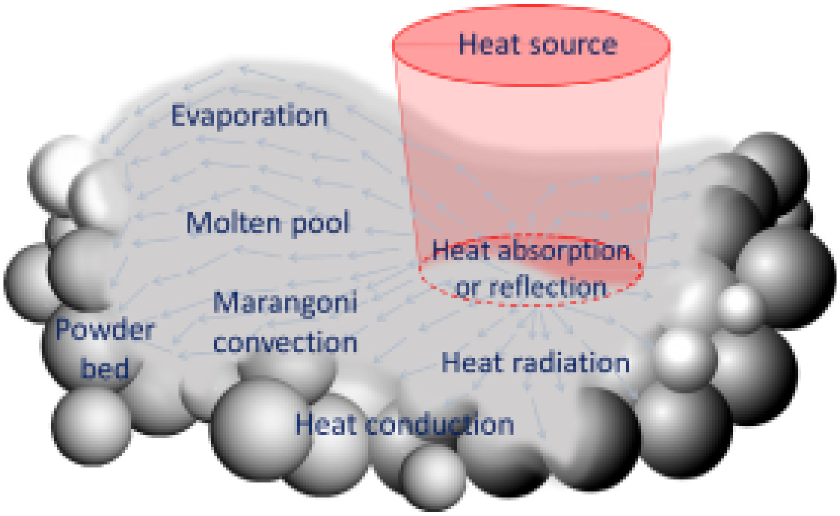

Fig. 1.7. Powder-based AM: Heat transfer and melt pool dynamics (reproduced with permission from [6]).

allowing for a broadened view of the parameter relationships. There are also a variety of finite element method approaches, more computationally expensive than analytical models, but providing improved accuracy and capable of accounting for a variety of heat transfer and fluid flow physics. Beyond this, models such as the Lattice Boltzmann Method provide improved accuracy, accounting for particle kinetics, but become computationally intensive and expensive.

When considering the vaporization which occurs during high-temperature metal processing, X He et al. discussed several equations for modeling the overall vaporization and change in weight due to vaporization during welding [15]. The total vaporization flux of species i in an alloy, J_i, can be described by:

$$J_i = J_{ci} + J_{pi} \tag{1.3}$$

where J_{ci} is the diffusion-driven vaporization flux of element i, accounting for vaporization due to the concentration gradient between a melt pool and shielding gas, and J_{pi} is the pressure driven vaporization flux of element i, accounting for vapor molecule velocity through the Knudsen layer and shielding gas above a melt pool surface [22]. Additionally, a positive flux means the evaporation loss of material from the system.

The total vaporization rate of all alloying elements, G, can be described by [46]:

$$G = \sum_{i=1}^{n} \iint_{s} J_i \, \mathrm{d}x \, \mathrm{d}y \tag{1.4}$$

where the total vaporization flux of each element i is integrated across the melt pool surface, s, and summed.

The concentration change of an element i can be found through the calculation of the total weight loss of element i, ΔW_i, given by:

$$\Delta W_i = \sum_{t} \iint_{s} J_i \, \Delta t \, \mathrm{d}x \, \mathrm{d}y \tag{1.5}$$

which is similar to the total vaporization rate calculation, but calculates loss by incorporating a time step Δt.

Another method for calculating the vaporization of species i in an alloy, J_i, can be defined by a variation of the Langmuir equation:

$$J_i = \frac{\lambda_c \, P_i}{\sqrt{2 \, \pi \, M_i \, R T}} \tag{1.6}$$

where λ_c is a unitless constant between zero and one that accounts for the condensation of a fraction of vaporized atoms, P_i is the equilibrium vapor pressure of an element i over the liquid alloy, M_i is the molecular weight of element i, and T is the surface temperature, and R is the universal gas constant [47]. At 1 atmospheric pressure, the Langmuir calculated vaporization flux tends to overestimate the actual rate by an order of magnitude, but can be alleviated by adjusting λ_c [12, 15]. This vaporization flux formulation is derived from the Kinetic Theory of Gases, which has two assumptions [48]:

1. Matter is made up of extremely small molecules
2. Molecules of a gas are in constant motion

In the Langmuir equation, the pressure term, P_i, can be determined through Raoult's law which states that the equilibrium vapor pressure of an element i over the liquid alloy is a function of the mole fraction of the element, χ_i and equilibrium vapor pressure of the element over the pure liquid, P_i^0:

$$P_i = \chi_i P_i^0 \tag{1.7}$$

The Antoine equation is used to calculated this equilibrium vapor pressure of a species i over the pure liquid, and depending on the reference used, can vary slightly in form. These equations are unique to each element and are typically described through a logarithmic function over a specified range of temperatures, T, with several fitting parameters (A_i, B_i, C_i) [49]:

$$\log P_i^0 = A_i - B_i/(T + C_i) \tag{1.8}$$

Shown in Figure 1.8, Mukherjee et al. utilized the Langmuir equation to predict composition change in weight percent for the volatile element of five different alloys [3].

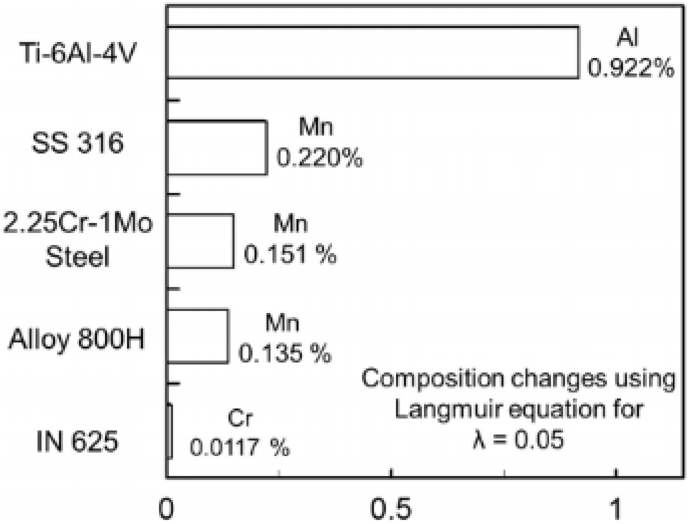

Fig. 1.8. Predicted values of composition change for the most volatile elements of several alloys. Laser power- 1000 W; Beam radius – 0.5 mm; Scanning speed – 12.5 mm/s; Layer thickness – 0.38 mm; Substrate thickness – 4 mm (reproduced with permission from [3]).

1.4.3 Process-Structure-Property Relationship

Drawing from welding literature, laser welding can be described by either of two fundamental modes, conduction welding and keyhole welding, based on the beam power, configuration, and its intent concerning the workpiece [21, 50]. In conduction mode welding, the beam is defocused and remains above the surface, and the power density remains too weak for boiling to occur at the respective welding speed [51]. As laser intensity and period of the applied laser pulse increase, conduction mode welding will transition to keyhole welding. Keyhole welding begins with the beam being focused beneath the surface and providing adequate energy per unit area for evaporation to occur. With rapid evaporation, a high enough back pressure can allow for the creation of a cavity [52]. Due to the formation of the cavity, the keyhole acts as a black body where the radiation enters the hole, and several reflections are incurred before it exits [25]. This correlates to an increased energy absorption efficiency, increased vaporization, and increased change in composition in keyhole welding as compared to conduction welding. This process parallels the AM process, where a continuous wave laser is applied and beam focus, laser power, and laser speed, among other parameters, can be modulated to enter either conduction or keyhole mode processing regimes.

The vaporization rates of different elements can be primarily dictated by two factors, the composition of the melt pool and the temperature distribution at its surface [37]. The temperature distribution can then be defined by features such as the beam energy absorption rate of the workpiece, natural convection, and the Marangoni number, Ma, describing convection driven by surface tension gradient, in the liquid region [33]. A larger Ma tends to signify a larger melt pool with a high aspect ratio, correlating to improved interlayer bonding and low porosity in fabricated parts [53]. The beam energy absorption rate is then reliant on the composition of plasma surrounding the melt pool, which is again determined by the melt pool's surface temperature distribution [12]. Several other factors affecting absorption in AM include the laser beam power density and wavelength, and the powder particle size and feed rate [54]. Also to be considered are properties of the workpiece, such as heat capacity and thermal diffusivity, where alloys with smaller heat capacity and larger thermal diffusivity are subject to increased melt pool volume and thermal gradients leading to more substantial thermal strain [55]. In the melt pool, both conduction and convection mechanisms dictate heat transfer, with their overall relative importance evaluated from the Peclet number, Pe:

$$\mathrm{Pe} = \frac{\text{convection}}{\text{conduction}} = \frac{L_R\, v\, \rho\, C_\mathrm{p}}{k} \tag{1.9}$$

where $\mathrm{L_R}$ is characteristic length taken as the pool width, v is the typical liquid velocity, ρ is density, $\mathrm{C_p}$ is specific heat, and k is thermal conductivity [53]. Convective heat transfer is the primary mechanism when Pe > 1, and a Pe » 1 can be associated with increased penetration depth in the weld, affecting the melt pool aspect ratio and vaporization. At the early stages of heating, proportionate contributions from conduction and convection result in a low Pe, but over time increasingly dominant convection effects equate to an increased Pe, quickly dropping once the heat source is removed [54]. This relationship demonstrates the importance of considering convective heat flow in a model. Otherwise, discrepancies in calculated and experimental melt pool geometry can occur and compound into vaporization and composition change calculations. Frewin and Scott experienced this when examining the pulsed laser welding of 1006 steel by predicting, with a finite element model that neglected convection, a fusion zone width of 0.68mm, and a depth of 0.46mm when the experimental results showed a width and depth of 0.89mm and 0.4mm, respectively [56]. These results and simplifications would have led to inaccuracies in vaporization and composition change calculations.

As part of an examination of high-manganese stainless steel welded by carbon dioxide lasers, Khan et al. found a considerable variation in the composition of the base and weld metal, chiefly due to the evaporation of manganese [23]. In a separate study, X He et al. examined the vapor composition and change in mass, for the laser spot welding of 304 stainless steel, caused by vaporization of alloying elements, and utilized the finite difference method to produce a 3-D transient numerical model [15]. The total vaporization flux considered both diffusion and pressure driven vaporization. The higher power density and pulse duration of the beam allowed for a peak temperature greater than the boiling point of 304 steel, at a point directly under the laser. This region experienced concentrated vaporization and surface vapor pressure exceeding ambient pressure. The convective flux of vaporized elements is then driven by excess pressure. The high power density and pulse duration significantly affected the transient temperature profile due to increased peak temperature, fluid velocity, and convective heat transfer. However, the computed vapor loss and measured mass loss did not match, until consideration was made for the expulsion of metal droplets caused by the recoil force of the excess pressure. The discrepancy in calculated and experimental weight loss values are shown in Figure 1.9.

As for the melt pool, the fluid motion was predominantly driven by the surface tension force and slightly by the buoyancy force. It was also noted that the vaporization heat loss was minimal and had no significant effect on computed surface temperatures [15]. Moon and Metzbower examined the composition and property change for the welding of aluminum 5456, utilizing a continuous CO2 laser and Helium gas shield [7]. After application of the beam, there was a noticeable depletion of Magnesium in the weld as compared to the base material, described by Table 1.2. This depletion of Magnesium at the weld site resulted in the loss of strain hardened structure, and porosity in the welds led to degraded tensile properties, both in strength and ductility, relative to the base metal.

Table 1.2. The difference in the composition of aluminum 5456 alloying elements at the base metal and weld center [7].

Element	Base Metal	Weld Center
Al	94.15	95.07
Mg	5.3	4.4
Mn	0.45	0.55
Cr	0.1	0.13

Cieslack and Fuerschbach similarly examined the change in properties of Aluminum 6061, 5456, and 5086 after pulsed and continuous laser welding [11]. Shown in Figure 1.10, alloy samples demonstrated a reduction in Mg content after each case of pulsed and continuous welding.

As with Moon and Metzbower, Magnesium depletion due to vaporization correlated to a decrease of solid solution strengthening and precipitation hardening in the alloys [7, 11]. When comparing

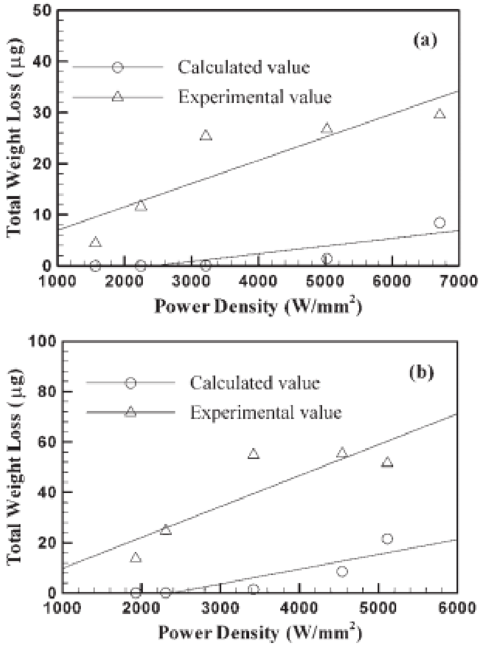

Fig. 1.9. Comparison of calculated vaporization loss with the measured mass loss for various power densities. (a) Laser power - 1067 W; Pulse duration - 3.0ms. (b) Laser power - 1967 W; Pulse duration - 3.0ms (reproduced with permission from [15])

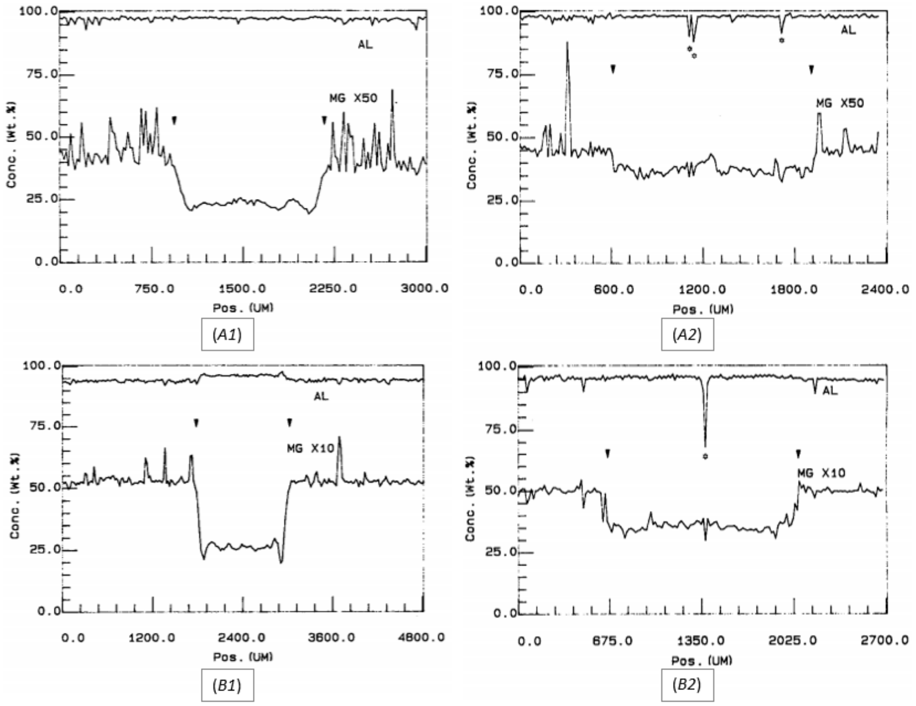

Fig. 1.10. Microprobe profile over Aluminum 6061 and 5456 weld, with arrows marking the fusion line. (A1) Alloy 6061: continuous weld; (B1) Alloy 5456: continuous weld; (A2) Alloy 6061: pulsed weld; (B2) Alloy 5456: pulsed weld (reproduced with permission from [11])

the pulsed with continuous laser beam, it was seen that both alloys experienced Mg loss, but only the pulse welded alloy displayed signs of hot cracking. This additional deficiency can be explained by a rapid solidification and cooling rate related to the pulsed laser welding. This is because the quickly growing thermal shrinking strains from solidification are too large for the weld metal to handle without cracking. This accountability for keeping a steady solidification and cooling rate to avoid deformations is one more aspect that should be kept in mind when looking to manipulate input parameters to achieve specific vaporization rates and composition changes in a fabricated part.

1.5 Conclusion

The fundamental understanding of vaporization in metals fabricated through AM is an essential component for the development of process-structure-property-performance relationships. There is a range of consequences AM components may experience due to vaporization, including composition change, which could result in reduced performance through material properties outside of design tolerances, reduced corrosion resistance, and reduced strength [6]. Vaporization must be considered appropriately in order to drive its impact on the parameter-structure-property relationship and improve the performance of a part. However, AM is a complex process with numerous processing parameters and a vast potential of materials with unique properties that must be considered. By investigating welding literature, the complex phenomenon involved with AM and inherent vaporization is analyzed at a smaller scale. From improved clarity and understanding of input parameters and their respective relationship with the structure of materials, significant advancements can be made in the AM process and leveraged to promote the controlled fabrication of enhanced materials. This can be realized through analytical models that have been developed to calculate vaporization rate and composition change in metallic alloys due to the application of an energy source, utilizing the principles of thermodynamics, transport phenomena, and kinetics. This will enable the production of metal-based AM parts with tailored spatially-dependent functional and structural properties in a systematic and controllable fashion, through the control of differential evaporation. The change in the composition of a metallic species in AM can be directly associated with its change in mass. Meaning, if input parameters (including laser power, pulse duration, and the alloying elements) and their effect on vaporization can be further understood and ultimately controlled, then the composition of an AM fabricated metallic species can be controlled and tailored for optimal structure, property, and performance. Table 1.3 provides a summary of several important factors to consider for evaporation.

Table 1.3. Brief summary of important factors relating to evaporation in AM. Factors can be influenced by beam power, beam speed, hatch spacing, scan strategy, material properties, and material composition.

Pressure	Smaller force on the surface ⇒ ↑ evaporation
Surface Area	Large surfaces ⇒ ↑ evaporation because more surface molecules can escape
Temperature	Higher temperature and average kinetic energy of molecules ⇒ ↑ evaporation
Density	Higher density ⇒ ↓ evaporation
Concentration	High concentration of substances in the atmosphere ⇒ ↓ evaporation
Activity	Measure of "effective concentration" of a species in a mixture
Vapor Pressure	Component of higher vapor pressure evaporates faster than lower vapor pressure components

Furthermore, vaporization within AM can be described by the relative contribution of three generalized steps [12, 18, 57]:

1. Alloying species from inside the melt pool are transported to the surface due to the fluid motion in the melt pool.
2. At the surface, the vaporization rate is influenced by the alloying element's local concentration, the exposed surface area, the surface temperature distribution, and by determinants such as surface agitation and plasma affecting the interface with the melt pool.
3. The vaporized alloying species will move from the melt pool surface to the bulk gas phase at a rate dependent on the boundary layer condition and the element's respective diffusivity.

When the vaporization of an alloying species occurs, this causes a deviation in the composition, structure, and properties of the part. For a suitable measurement of vapor pressures at high temperatures, two methods that can be tuned for different environmental inputs, Langmuir and Knudson, are applied towards modeling and calculating the vaporization flux [34, 40, 45, 58]. The contributions of the pressure gradient and concentration gradient towards vaporization flux may also be considered in calculations [17, 59]. Total vaporization can then be shown to play an essential role in the AM process and contribute to the composition change of a fabricated part. Although this is commonly viewed as a detriment when hoping to maintain the feedstock composition and corresponding properties, proper understanding of process-structure-property-performance relationships could enable the advantageous use of vaporization to tailor location-specific structure, composition, and properties [9]. Hopefully, this review of vaporization has taken the field one step closer to answering the main question of how one can eventually solve the inverse problem: for the desired property range of an AM part or at a location of the AM part, which process parameters and scan strategies, among many, should be selected to reach that property range reliably and repeatedly, with the available range of process parameters? However, it should be understood that vaporization in AM is just one milestone in linking materials chemistry and processing parameters to post-processed properties.

1.5.1 Future Work

Another important concept that AM realizes is the possibility of creating functionally graded materials (FGM) and components. In FGMs, composition (and microstructure/properties) are gradually changed as the component is being printed. The successful fabrication of FGMs, however, is limited by the formation of undesirable phases and difficulties in planning material gradients that avoid these phases [60, 61]. In high-dimensional alloy systems, avoidance may be impossible or require absolute precision and control over the printing path. A significant factor that compromises the controllability of compositions deposited is differential evaporation. This can be remedied by considering differential evaporation and predicted chemistry changes during AM. Integrating an evaporation model with a path planning algorithm will provide the means to predict chemistry changes from uncontrolled evaporation and to correct for them as an FGM path is being defined. This will enhance path planning capabilities and the ability to print a higher order of FGMs successfully.

When examining the aeronautical industry, the enhanced performance, and increased reliability of space technologies is a significant hurdle toward improved spacecraft capabilities and missions of planetary exploration. These criteria are most effectively addressed through weight reduction and fusion of parts, resulting in reduced fuel usage, fuel tank size, cost, and fewer points of failure. Through the advent of AM, both are realized by melding multifarious parts, such as rocket engines, and reducing the need for fasteners. However, due to vaporization and chemistry change during fabrication, there is uncontrolled variability in the composition and properties throughout the part, translating into an unreliable and suboptimal product. This is detrimental for the mission-critical nature of space technologies, where it is essential to have dependable, high-quality parts that uphold their functional and structural requirements. However, by applying an evaporation model towards computationally designing materials and an increasingly systematic and controlled fabrication process, chemistry changes can be predicted pre-production and adjustments made to the powder stock and processing parameters to ensure uniformity between the designed and printed component. This directly translates into improved performance, reliability, and safety. The improved designability of AM components, enabled by an evaporation model, concurrently results in savings of time and money, by allowing a more extensive range of advanced parts to take advantage of AM's short lead time and weight-reducing precision.

By including an evaporation model in a computational material design framework, there is the additional benefit of tailoring spatially-dependent functional and structural properties. This will impact SMA actuators, joints, nozzles, pressure vessels, and future AM tailored alloy design by enabling localized microstructure design of functional materials, structural materials, and FGMs. Increased control over the composition of additively manufactured SMA actuators ensures that target functional properties are met and provides the ability to systematically vary the composition and properties throughout the part. Similarly, this increased control may be used in conjunction with path planning models to reduce defects, improve performance, and improve the reliability of additively manufactured FGMs for joints, nozzles, and pressure vessels.

2. A DIFFERENTIAL EVAPORATION MODEL TO PREDICT CHEMISTRY CHANGE OF ADDITIVELY MANUFACTURED METALS*

2.1 Overview

The desire for increased performance and functionality has introduced additional complexities to the design and fabrication of additively manufactured (AM) parts. However, addressing these needs would require improved control over local properties using in-line feedback from fast-acting low-fidelity models during the fabrication process. In this regard, differential evaporation is an inherent characteristic in metal AM processes, directly influencing local chemistry, material properties, functionality, and performance. In the present work, a differential evaporation model (DEM) is presented for laser powder bed fusion (LPBF) AM to predict and control the effect of evaporation on chemistry and properties on local and part-wide scales. The DEM model is coupled with an analytical thermal model that is calibrated against 51.2 Ni [at.%] nickel titanium shape memory alloy (NiTi SMA) single-track experiments and a multi-layer model that accounts for the AM part's multi-layer design and the inherent melt pool overlap and chemistry propagation. The combined hierarchical model, consisting of the thermal, evaporation, and multi-layer components, is used to predict location-specific chemistry for LBPF AM fabrication of $Ni_{50.8}Ti_{49.2}$ [at%] SMAs. Model predictions are validated with values obtained from multi-layer experiments on a commercial LPBF system, resulting in a root mean square error (RMSE) of 0.25 Ni [at.%] for predicted Ni content. Additionally, martensitic transformation temperature, M_s, is calculated and compared with empirical data, resulting in an RMSE of 18.6 K. A practical account of the cumulative and propagative thermal-induced evaporation effect on location-specific chemistry is made through this linkage of models. Fundamentally, this model chain has also provided a solution to the forward modeling problem, enabling steps to be taken towards resolving the inverse design problem of

---

[*] Republished with permission from Ranaiefar, M., Honarmandi, P., Xue, L., Zhang, C., Elwany, A., Karaman, I., Schwalbach, E.J. and Arroyave, R., 2022. "A Differential Evaporation Model to Predict Chemistry Change of Additively Manufactured Metals." *Materials & Design*, 213, p.110328 [14] under an open access Creative Commons license. No changes were made to the original document.

determining processing parameters based on desired location-specific properties.

2.2 Introduction

Additive manufacturing (AM) of functional and structural materials has received increased attention to meet the demand for specialty components in the aerospace, automotive, and medical industries [62–65]. Through design optimization and improved control over the AM process, components with improved performance and functional properties have been successfully fabricated from materials such as Ti-6Al-4V, stainless steels, and NiTi shape memory alloys (SMAs), among many others. AM has been traditionally regarded as a manufacturing method that can be used to fabricate components with high degrees of geometric complexity. While this is certainly true, much larger (and rather underutilized) potential lies in achieving material complexity through effectively modulating and controlling underlying mechanisms associated with the complex AM process. One such mechanism that can be harnessed to achieve location-specific control of properties and improved component quality of AM tailor-designed parts is differential evaporation.

Several studies involving laser processing of Ti-6Al-4V and stainless steels have shown that differential evaporation influences the post-process composition of a part [66–68], leading to a change in functional and structural properties. In the case of NiTi, Khan et al. demonstrated that laser processing of NiTi (50.07 at.% Ni) SMA resulted in Ni depletion and an outcome of $(48.36 \pm 0.84)\,[\mathrm{at\,\%}]$ Ni [69]. The processed region also experienced a microstructural change from austenite to martensite, and Ti_2Ni precipitates were found in the processed region due to Ti's insolubility in the Ni depleted region. The significant influence of evaporation on functional properties is then exhibited through changes of 1 [at.%] Ni resulting in $(80\text{–}100)\,\mathrm{K}$ changes in transformation temperature for Ni compositions above 50 at.% [70, 71]. Ma et al. [72, 73] captured this process-structure-property relationship in NiTi by changing hatch spacing during laser-based AM from $35\,\mu\mathrm{m}\text{–}120\,\mu\mathrm{m}$ for two sections of a monolithic NiTi part. This alteration and the change in the resulting volumetric energy density (VED) input translates to a distinct difference in thermal history, the magnitude of evaporation, and post-process chemistry. Indeed, this resulted in a difference of 60 K in transformation temperature for each section of the part, demonstrating the effect of evaporation on the chemistry and functional properties of an AM NiTi part [74].

Advancing the capability for tailored AM design would then require a comprehensive understanding of vaporization and the process-structure-property-performance (PSPP) relationship in AM. Figure 2.1 illustrates the complexity of this PSPP relationship for SMA NiTi vaporization in AM. An AM part's final chemistry and properties are the culmination of a set of processing parameters and the repeated thermal processing of the initial powder composition, building track-after-track and layer-upon-layer. In principle, by controlling the process conditions at each location of the part, it would be possible to alter the local thermal history and affect the (differential) evaporation process. In the case of functional materials, such as NiTi-based SMAs, that are extremely sensitive to chemical and microstructural changes, such degree of local control could enable, for example, 4D printing of metallic components[72, 75].

To explicitly leverage *differential evaporation* as a tool to provide location-dependent control over chemistry, microstructure, properties and behavior, it is necessary to develop formal design tools capable of transforming a desired (local) chemistry/microstructure into a required (local) processing protocol. The first necessary ingredient of such a design tool would be a suitable chain of *forward* models capable of connecting process conditions, thermal histories and chemistry changes due to differential evaporation. Experimental approaches to building such connections are impractical. High-fidelity numerical models are extremely costly, particularly when considering that simulations must be able to capture local changes in chemistry at the part level. One solution to this forward problem is the utilization of fast-acting, physically-rich (semi) analytical models calibrated and validated with experiments to provide relatively accurate simulations of the PSPP relationship for the sake of AM product design.

In order to quantify the effect of evaporation, the thermal history of an AM part must first be simulated through numerical or analytical solutions. These simulations can be performed to varying degrees of complexity and fidelity, with the tradeoff of computational cost. High-fidelity models have arisen from the need to address complex coupling present in the various mechanisms in place during AM. Such models may employ finite element [76–85], finite difference [86], or finite

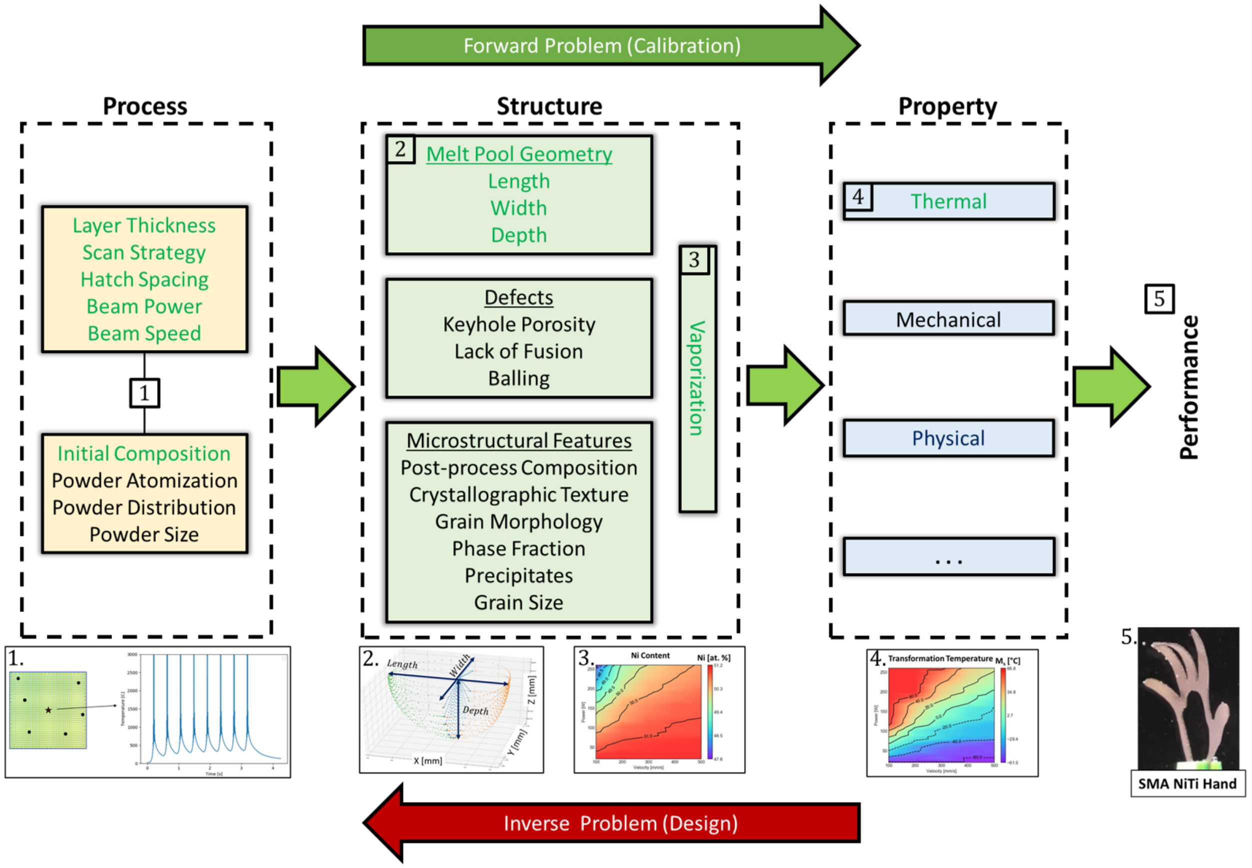

Fig. 2.1. Process-Structure-Property-Performance diagram toward the location control of properties and tailored design of AM fabricated parts. Components considered by the computational model in this work are highlighted in green. Modeling components include: Process to Structure - (1) Thermal Model; Structure to Property - (2) Multi-Layer Model, (3) Differential Evaporation Model, and (4) Ni-Transformation Temperature Relation. Property to Performance coupling can then be performed based on desired specifications and experiment results (5).

volume [87–89] methods. However, these high-fidelity solutions come at a high computational cost, limiting their utility for the AM design process [90, 91] and parameter calibration [92]. For comprehensive exploration of the AM design space, a fast analytical model yielding an acceptable degree of fidelity and accuracy presents a desirable approach [93]. Linking this fast-acting thermal model with a cost-effective structural and property-based model in an integrated computational materials engineering (ICME) framework then enables the screening of trends in the (forward) PSPP of AM parts and can also aid the reverse PSPP linkage in product design.

In this study, a fast-acting thermal-history coupled differential-evaporation model is developed to predict the change in chemistry for laser powder bed fusion (LPBF) AM parts, as highlighted in green alongside corresponding depictions in Figure 2.1. A follow-up study will then further explore and exploit this model to solve the inverse design problem, where inexpensive physically-rich models are applied to guide experiments. Model assumptions are presented, simulation and calibration of melt pool geometry discussed, a mass balance analysis is conducted, and considerations for evaporation rate are presented. In conjunction, an assessment of a multi-layer model accounting for geometric effects is provided. Model predictions for location-specific chemistry (Ni [at.%]) are then validated with experiments and linked to material properties (martensite transformation temperature, M_s) - providing a complete path through the PSPP relationship and a solution to the forward design problem. NiTi SMA was chosen as the model material for this work due to its industrial relevance, functional properties, and vapor pressure difference among the alloying components ensuring a measurable change in post-process composition.

2.3 Thermal Model Calibration

2.3.1 Thermal Model

The thermal model used in this study, a fast-acting analytical discrete source model (DSM), was developed and described in detail by Schwalbach et al. [94]. In the current work, directly relevant aspects of the DSM will be described briefly, but the reader is referred to the reference for more details. Additionally, this inexpensive low-fidelity model will be calibrated similar to [95], providing sufficiently accurate results for the purpose of this work. Although the individual models comprising the ICME framework in this study are generally modular, where a higher-fidelity model could instead be substituted in, this does not necessarily alleviate all calibration requirements, and computational cost must be balanced against fidelity requirements for the purposes of rapid design iterations.

2.3.1.1 Assumptions

This model's development begins with the generation of assumptions used to describe and simplify the physics involved in thermal history simulation and corresponding melt pool geometry during LPBF AM. These assumptions are broadly similar to those of the Rosenthal model of fusion welding, with the main exceptions that the heat source is allowed to move in an arbitrarily complex path, and that its shape is an elliptical 3D gaussian. The main model assumptions include:

1. Thermophysical properties are considered temperature independent, enabling model simplification. From a previous study by Schwalbach et al. [94], temperature dependency of material properties has a minimal effect on predicted melt pool characteristics. However, the distributions associated with their effective values are obtained after probabilistic model calibration against experiments to cover for any possible uncertainties resulting from this assumption.
2. Latent heat due to phase change is assumed to be less than the sensible heat during the thermal process. It is indirectly considered through a calibrated effective heat capacity parameter.
3. Heat transfer is directly governed by the heat conduction equation in the model, while the effects of radiation, evaporation, and convection to the gas are indirectly considered in the form of a tuning parameter called the efficiency parameter—which accounts for the material absorption efficiency as well. Moreover, the physically complex convection in the liquid and its effect on the melt pool shape is also indirectly implemented in the model through the consideration of a shape factor, i.e., the depth to width ratio of the volumetric heat source [96]. This ratio requires calibration for each individual experimental condition, but is assumed to be

constant and equal to 1 in this work for simplicity. Accordingly, a physical depth correction factor is considered and calibrated against experiments for cases that the keyhole criterion is met—based on NiTi alloy printability maps [97]—in order to account for the significant effect of convection in these cases.

4. Scanning speed and power input are constant, as in the experimental setup, although the DSM is capable of handling arbitrary changes in these quantities if required.

Through these assumptions, a reduction in both fidelity and cost are incurred. This results in a model ideal for the purpose of screening for trends that will be used as a basis for experiments and materials design. However, in the interest of analyses requiring extreme precision, the DSM may be exchanged with a thermal model of higher fidelity, but typically at increased cost.

2.3.1.2 Thermal History

In general, the DSM predicts the temperature at any specifically given position ($\vec{r}_j$) and process time (t) during the thermal process. It does this by considering the thermal energy input at the position from a series of volumetric discrete heat sources ($\vec{s} = \{s_1, \ldots, s_N\}$ that activate one by one during the process at $\vec{\tau} = \{\tau_1, \ldots, \tau_N\}$, respectively) and the energy conduction throughout the material, as follows:

$$\frac{\partial T}{\partial t} = D\nabla^2 T + \sum_{i=1}^{N} \frac{\hat{s}_i(\vec{r}_j, t)}{\rho C_p} \tag{2.1}$$

where T, ρ, and C_p are temperature, mass density, and mass specific heat capacity, respectively. D is thermal diffusivity, a temperature-independent parameter, and correlated to thermal conductivity (κ) as $D = \frac{\kappa}{\rho C_p}$.

Assuming the discrete heat sources have spherical normal-distribution shapes centered at $\vec{r}_i$ with standard deviations equal to σ, Equation 4.1 becomes:

$$\frac{\partial T}{\partial t} = D\nabla^2 T + \sum_{i=1}^{N} \frac{2\eta_i P_i \Delta t}{\rho C_p (2\pi\sigma^2)^{1.5}} exp\left(- \frac{R_{ij}^2}{2\sigma^2} \right) \delta(t - \tau_i) \tag{2.2}$$

where η_i, known as efficiency, accounts for the material's energy absorptivity and, upon activation of the heat source i, energy losses due to radiation and evaporation. $\eta_i P_i$ is the effective power of heat source i, where P_i is the actual power of the heat source. It should be noted that η_i and P_i are assumed to be constant in this work, denoted as η and P. Δt is the source discretization time, $R_{ij} = |\vec{r}_j - \vec{r}_i|$ is the distance of the given position from source i, and δ is the Dirac delta function.

Solving Equation 2.2 for an infinite uniform medium with initial temperature T_0 results in the temperature prediction at any given position and process time:

$$T(\vec{r}_j, t) = T_0 + \sum_{i=1}^{N} \left\{ \frac{\eta_i P_i \Delta t}{\rho C_p \sqrt{2} \pi^{1.5}} \Theta(t - \tau_i) \big(\sigma^2 + 2D(t - \tau_i)\big)^{-1.5} \exp\left(- \frac{R_{ij}^2}{2\big(\sigma^2 + 2D(t - \tau_i)\big)} \right) \right\} \tag{2.3}$$

where Θ is the Heaviside step function. For more details about the model formulation, see [94].

2.3.1.3 Melt Pool Geometry

The melt pool formed through the previously described interaction of the laser and material can define a controlled volume in the printing process, a vital step for evaluating the effect of evaporation. For the remainder of the work, it should be noted that the beam propagates along the Z-direction, and traverses the XY-plane of the powder bed along the X-direction. Assuming a quasi-steady state, the melt pool's extent at any location of interest is then determined based on solidification time. A radial vector search pattern centered about the location of interest provides a resolved 2D cross-section of the YZ-plane (width and depth) along with intermediary points, as shown in Figure 2.2 (A). The solidification time for each coordinate, $t_{solid,yz}$, and laser velocity, u, may then be used to determine a length, L_B, representing the back portion of the melt pool:

$$L_{B,yz} = (t_{solid,yz} - t_{solid,min})u \tag{2.4}$$

where $t_{solid,min}$ is the minimum solidification time from all points in the 2D cross-section. Following this, the length of the melt pool front, L_F, is determined by evaluating the melting time of each coordinate, $t_{melt,yz}$, in the 2D cross-section:

$$L_{F,yz} = (t_{solid,min} - t_{melt,yz})u \tag{2.5}$$

Figure 2.2 (B) then illustrates the derived 3D melt pool, where length, width, and depth correspond to x, y, and z coordinates, respectively. These points may be represented as a convex hull, allowing the melt pool volume to be determined. It should be noted that the resolution of this convex hull is dependent on the number of 2D intermediary points considered. However, the calculation of additional points will increase computational cost and approach a diminishing return regarding the convex hull volume.

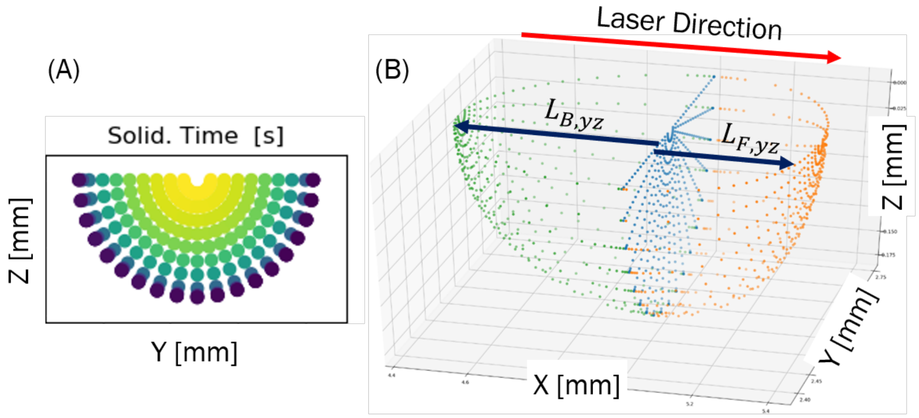

Fig. 2.2. Melt pool schematic. (A) YZ-melt pool extent (B) 3D melt pool projection

2.3.1.4 Keyhole Depth Correction

Our previous work [95] with similar analytical models showed that these models typically underestimate the melt pool depth for the print conditions with particular combinations of high laser powers and low laser velocities that correspond to the keyhole mode. In these cases, high linear energy density ($LED = \frac{P}{u}$) input from the laser beam and lack of time for the substrate to dissipate energy via heat diffusion mechanism across the material cause heat accumulation in the melt pool and a local rise in temperature above the material boiling temperature, inducing substantial elemental evaporation. This large evaporative effect imposes an opposite force on the melt pool surface, known as the recoil pressure, which results in deeper penetration of the molten material, considerably increasing the melt pool depth under these conditions [98]. Since the physics associated with the keyholing phenomenon is not considered in such analytical thermal models, the model response for depth is corrected for the print conditions experiencing keyholing, as proposed in [95]. This depth correction is performed based on a simplified model proposed by Gladush and Smurov [99], providing a general solution for keyhole depth, d_k. Derivation involves solving the heat conduction equation for a semi-infinite slab under the assumption of cylindrical keyhole formation with radius σ resulting from the laser beam interaction:

$$d_k = \frac{\eta P}{2\pi\kappa T_b} \ln\left(\frac{\sigma + \frac{D}{u}}{\sigma}\right) \tag{2.6}$$

where T_b is the boiling temperature.

The differences between the melt pool depths predicted by the thermal model and their experimental counterparts are assumed to be proportional to the formulation in Equation 2.6 when the input variables fall into the keyholing regime. Therefore, a correction factor, C, multiplied with this formulation is added to the predicted depth for each print experiencing the keyholing regime. The probabilistic calibration of parameter C and other uncertain material properties in the thermal model against available experimental data for melt pool width, w_{exp}, and depth, d_{exp}, is discussed in Section 2.3.4. It should be noted that an experimentally-derived criterion [90, 91], i.e., $\frac{w_{exp}}{1.5} \leq d_{exp}$, is considered in this parameter calibration to find the experiments with the keyholing effect, where the depth correction is required to be applied in their corresponding model predictions. This keyholing criterion can also be used to identify the corresponding Power-Velocity region in the processing space of NiTi SMAs, which indicates whether or not a prediction needs the keyhole depth correction based on the print input conditions.

2.3.2 Experimental Procedures

Gas-atomized $Ni_{51.2}Ti_{48.8}$ [at.%] powder with $d80$ (the 80th percentile of the powder size distribution) of 32 μm provided by *Nanoval GmbH & Co. KG* is used to manufacture the single tracks in this work. Samples are printed using a 3D Systems ProX DMP 200 Laser Type (fiber laser with a Gaussian profile λ = 1070 nm, and a beam size (4σ) of 80 μm) with a powder layer thickness (q) of 30 μm (~$d80$). These single-track prints are performed on equiatomic NiTi substrates cut from larger cylindirical bars using wire electro-discharge machining (EDM). The printed single tracks are sectioned orthogonal to the direction of beam travel, and the cross sections are polished up to a 0.25 μm water-based diamond solution. They are then etched in one part HF, three parts HNO_3, and ten parts of DI water for 15 seconds to reveal the melt pool shape. Using optical microscopy (OM) images, the depth and width of melt pools are measured in three YZ-plane cross-sections in each single-track. Their averages, listed in Table 2.1, are utilized for the calibration and validation of the thermal model. In Figure 2.3, some of the OM cross-section images are shown for prints performed at different laser powers and velocities, which result in different print modes during the LPBF process.

2.3.3 Calibration Approach

An adaptive Markov Chain Monte Carlo (MCMC) procedure is applied to conduct Bayesian parameter inference. In this calibration framework, the prior belief (or distributions) for uncertain parameters are updated to their posterior distributions, given the available experimental data represented by a likelihood function. In this context, solving the intractable integrals for the statistical inference of parameters necessitates a sampling method. Pseudocode detailing this adaptive MCMC algorithm is shown in Figure 2.4.

The process starts with an initial guess for the parameter values, represented by prior distributions, and then proceeds by the sequential sampling of parameter vectors from a proposal posterior distributions. In this work, the proposal distribution is considered a multivariate normal distribution centered at the previous parameter vector in the MCMC chain with a variance-covariance

Table 2.1. Average measured melt pool width and depth for single-track prints, measured from $Ni_{51.2}Ti_{48.8}$ powder at different process conditions. Experimental measurements are separated for the thermal model calibration and validation.

P (W)	u (mm/s)	LED (J/m)	$\bar{w}$ (μm)	$\bar{d}$ (μm)
Experimental Data Used for Thermal Model Calibration				
40	80	500.0	135.11 ± 18.46	25.90 ± 8.67
80	330	242.4	129.65 ± 1.41	32.55 ± 1.91
120	580	206.9	101.52 ± 22.52	27.03 ± 5.48
200	580	344.8	149.26 ± 6.64	85.14 ± 8.65
120	830	144.6	101.84 ± 16.16	26.40 ± 6.87
160	830	192.8	112.10 ± 0.43	48.69 ± 8.30
240	830	289.2	136.52 ± 9.33	77.14 ± 8.92
160	1080	148.1	109.63 ± 19.63	16.49 ± 4.71
200	108	185.2	114.01 ± 11.52	37.37 ± 3.51
240	1080	222.2	115.92 ± 7.96	57.75 ± 5.92
200	1330	150.4	110.72 ± 15.83	24.77 ± 2.29
240	1580	151.9	107.96 ± 5.20	35.98 ± 3.26
60	205	292.7	114.23 ± 14.67	41.40 ± 8.99
60	455	131.9	78.70 ± 5.28	21.73 ± 4.38
100	455	219.8	117.06 ± 9.96	60.82 ± 17.78
160	80	2000.0	326.84 ± 0.68	376.65 ± 38.90
200	80	2500.0	377.51 ± 12.04	469.21 ± 53.69
240	80	3000.0	417.41 ± 20.31	511.68 ± 38.77
160	330	484.8	160.93 ± 5.71	139.49 ± 46.69
200	330	606.1	176.22 ± 12.650	207.64 ± 43.66
240	330	727.3	201.84 ± 21.32	283.93 ± 13.06
240	580	413.8	148.27 ± 8.40	195.40 ± 10.87
100	205	487.8	165.11 ± 5.88	119.60 ± 19.16
140	205	682.9	179.19 ± 5.30	251.66 ± 1.77
140	455	307.7	138.43 ± 4.95	140.13 ± 26.36
Experimental Data Used for Thermal Model Validation				
80	80	1000.0	230.79 ± 9.65	143.10 ± 11.58
160	580	275.9	124.06 ± 16.72	42.11 ± 20.77
200	830	241.0	126.04 ± 1.56	72.61 ± 6.65
240	1330	180.5	109.66 ± 3.49	32.60 ± 14.15
200	1830	109.3	61.39 ± 19.01	19.06 ± 10.08
240	1830	131.1	97.58 ± 4.13	40.86 ± 8.26
120	80	1500.0	291.66 ± 4.92	248.01 ± 15.73
120	330	363.6	138.36 ± 3.63	108.28 ± 7.01

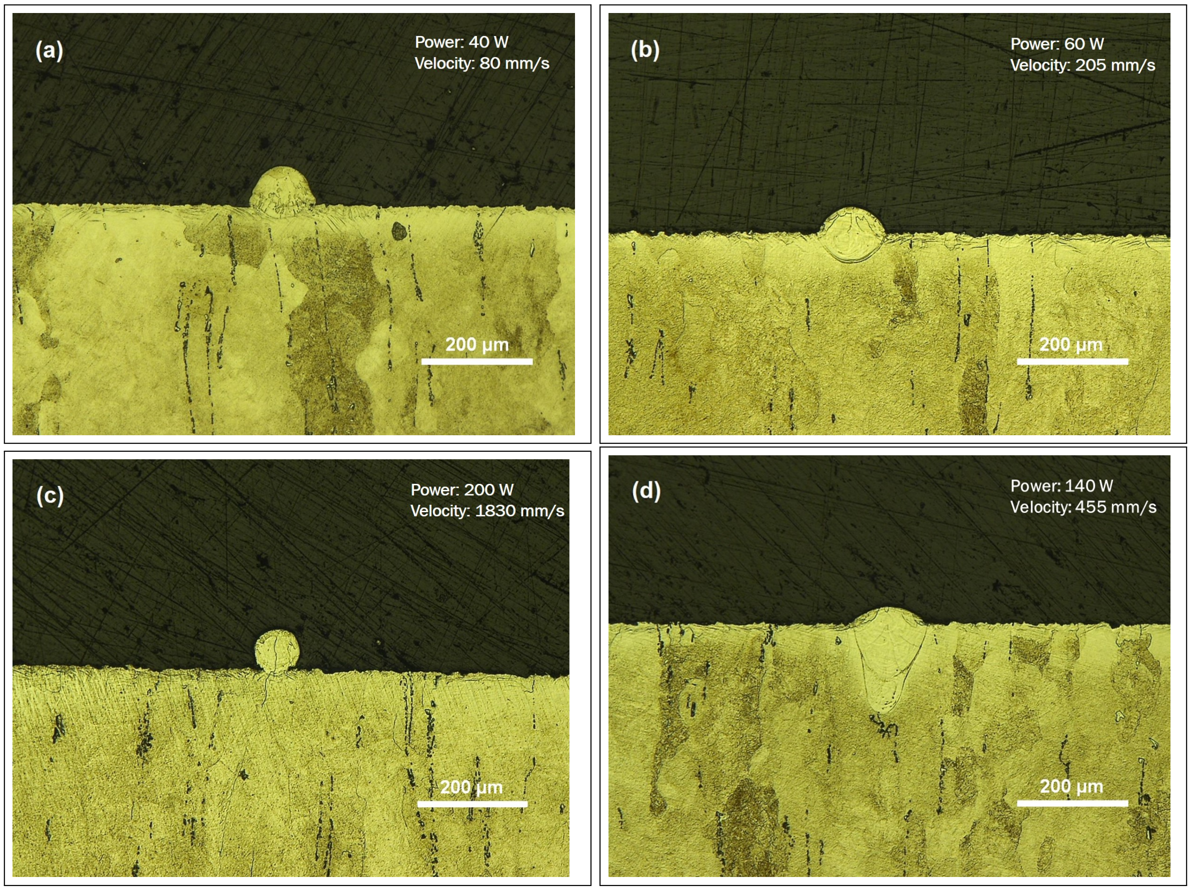

Fig. 2.3. Cross-section print images obtained from optical microscopy for different print conditions during the LPBF process, indicating different print modes, a) lack of fusion, b) good quality, c) balling, and d) keyholing modes.

```
Algorithm 1: Adaptive MCMC algorithm used in this work
input:
  - Initial guess for parameters $\boldsymbol{\theta}^0$, lower bounds $\boldsymbol{\theta}_{min}$, upper bounds $\boldsymbol{\theta}_{max}$, prior density $p(\boldsymbol{\theta})$,
    and number of samples $N_s$
  - Data $\boldsymbol{D} \leftarrow \{\boldsymbol{D}^k\}_{k=1}^K$ and a diagonal variance-covariance matrix fixed for all data $\boldsymbol{\Sigma}_{\boldsymbol{D}^k} \leftarrow \boldsymbol{\Sigma}_{\boldsymbol{D}}$
  - Initial guess for the proposal variance-covariance matrix $\boldsymbol{\Sigma}^0$

output:
  - Generated samples $S = \{\boldsymbol{\theta}^0, \dots, \boldsymbol{\theta}^{N_s}\}$ and posterior density of the parameters $p(\boldsymbol{\theta}|\boldsymbol{D})$

Initialize
  $S \leftarrow \emptyset$
  for $i \leftarrow 1$ to $N_s$ do
      if $i = 1$ then
          $q(\boldsymbol{\theta}|\boldsymbol{\theta}^0) \leftarrow \mathbb{N}(\boldsymbol{\theta}^0, \boldsymbol{\Sigma}^0)$
      else
          Adapt the proposal posterior density:
          $q(\boldsymbol{\theta}|\boldsymbol{\theta}^{i-1}) \leftarrow \mathbb{N}(\boldsymbol{\theta}^{i-1}, \boldsymbol{\Sigma}^{i-1})$ s.t. $\boldsymbol{\Sigma}^{i-1} \leftarrow S_d[\boldsymbol{\Sigma}^{i-2} + \varepsilon I_d], S_d \leftarrow \frac{2.4^2}{d}$, and $\varepsilon > 0$
      end if
      Draw a candidate from the proposal posterior density: $\boldsymbol{\theta}^{cand} \sim \mathbb{N}(\boldsymbol{\theta}^{i-1}, \boldsymbol{\Sigma}^{i-1})$
      Calculate Metropolis-Hastings ratio:
          $MH \leftarrow \frac{p(\boldsymbol{\theta}^{cand})p(\boldsymbol{D}|\boldsymbol{\theta}^{cand})}{p(\boldsymbol{\theta}^{i-1})p(\boldsymbol{D}|\boldsymbol{\theta}^{i-1})} \frac{q(\boldsymbol{\theta}^{i-1}|\boldsymbol{\theta}^{cand})}{q(\boldsymbol{\theta}^{cand}|\boldsymbol{\theta}^{i-1})}$ s.t. likelihood $p(D|\theta) \leftarrow \prod_{k=1}^K \mathbb{N}(\boldsymbol{D}^k, \boldsymbol{\Sigma}_{\boldsymbol{D}})$
      Draw a random number from a uniform distribution in the range of 0 to 1: $u \sim \mathrm{Unif}[0, 1]$
      if $MH > u$ then
          Accept the candidate: $\boldsymbol{\theta}^i \leftarrow \boldsymbol{\theta}^{cand}$
      else
          Reject the candidate: $\boldsymbol{\theta}^i \leftarrow \boldsymbol{\theta}^{i-1}$
      end if
      Update the sample chain: $\boldsymbol{S} \leftarrow \boldsymbol{S} \cup \{\boldsymbol{\theta}^i\}$
  end for
  Remove the burn-in period: $\boldsymbol{S}_{post} \leftarrow \boldsymbol{S} - \boldsymbol{S}_{burn}$
  Determine the parameter posterior density: $p(\boldsymbol{\theta}|\boldsymbol{D}, \boldsymbol{S}_{post})$
```

Fig. 2.4. Pseudocode describing the implementation of the adaptive MCMC algorithm.

matrix adapted in each sampling iteration by the variance-covariance matrix of previous samples based on [100]. The parameter samples are accepted or rejected during the sequential process, using the Metropolis-Hastings criterion that accepts the new sample with a probability equal to min{MH,1} in each iteration. Here, MH is the Metropolis-Hastings ratio that compares the joint probability (prior*likelihood) of the new sample with the previous one in the chain, as well as the probability of moving from the previous to the new sample with the probability of the reverse move. If the new sample is rejected, the previous sample repeats in the chain. It should also be noted that the prior and likelihood were considered as uniform distributions and a multivariate normal distribution, respectively, centered at the independent experimental data with a constant diagonal variance-covariance representing the average experimental uncertainty for width and depth measurement. The mentioned sampling process stops when the proposal distribution reaches a stationary state as the parameter convergence occurs. At the end of this process, the samples before the parameter convergence, known as the burn-in period, are removed from the chain in order to represent the posterior frequency/probability distributions of model parameters and their statistical characteristics (see [101–108] for further details about the applied MCMC calibration approach).

2.3.4 Calibration Results

Generally, all models are surrogates of reality with their specific assumptions and approximations, regardless of their fidelity and cost. Therefore, their probabilistic calibration against data is required in order to provide the most plausible predictions within their uncertainty bounds. It should also be noted that Bayesian calibration is not hindered by limited data, providing the best inference corresponding to the current state of knowledge. In this work, modeling of the melt pool geometry is one of the main components to the modeling of the print as a whole, emphasizing the importance of calibrating the thermal model. The DSM calibration is conducted using the results obtained from 33 single-tracks listed in Table 2.1 (split into 25 training and 8 test data points), printed using $Ni_{51.2}Ti_{48.8}$ powder, as described in Section 2.3.2. Melt pool widths and depths measured from these prints at different combinations of laser power and velocity are used simultaneously in a multi-objective optimization scheme, based on the adaptive MCMC described in Section 2.3.3, to provide a probabilistic estimation of the model parameters. The calibration parameters are then η, effective κ, effective C_P, and C, while other parameters remained constant. Additionally, by utilizing data from both conduction and keyhole regions, the model is effectively homogenized for both modes through the calibrated model parameters and any uncertainties related to this are covered in the uncertainty quantification.

After generating 20,000 MCMC samples for the mentioned parameters and removing the burn-in period, the marginal probability density functions (PDFs) were plotted for each parameter in Figure 4.4. The average and standard deviations of these parameter samples were also reported in Table 4.2, representing the parameter plausible optimal values and uncertainties. As shown in Figure 4.5, the correlation between parameter pairs can also be studied qualitatively and quantitatively through the 2D joint PDF plots and the Pearson linear coefficient, $\rho_{X,Y} = \frac{cov(X,Y)}{\sigma_X \sigma_Y}$, respectively. In the plots in Figure 4.5, the colors represent the density of parameter samples in the joint parameter spaces, and the linearity of color features qualitatively demonstrates the degree of linear correlation between each parameter pair. The Pearson linear correlations, ρ, shown at the bottom right corner of each plot can change from -1 to 1, with a value close to -1 or 1 indicating strong correlation and a value close to 0 indicating weak correlation between the parameters. It is worth noting that the negative and positive signs show the correlation direction. Here, the ρ values suggest a strong correlation between the thermal model parameters. This can be expected due to the linear correlation between heat capacity and thermal conductivity [109] and due to the efficiency parameter acting as a tuning metric. Additionally, a very weak correlation is seen between the thermal model parameters and C, implying an independent effect of parameter C and its non-substitutability with the other three parameters. These correlations help explain a trend observed in Figure 4.4, where the probability for η increases as the upper bound is approached, implying a peak value greater than 0.8. However, this high efficiency is physically impossible, and could be a result of the missing physics in the model and the uncertainties in the experimental measurements. Addressing these issues in future work would then allow the posterior peak for η to shift to a reasonable range for this parameter. Two other model parameters observe similar trends due to their high linear correlation with η, κ with ρ = 0.93

and more prominently in C_P with $\rho = 0.99$. However, as an extrinsic factor, C can independently peak around an optimal value due to its low linear correlation with the other parameters.

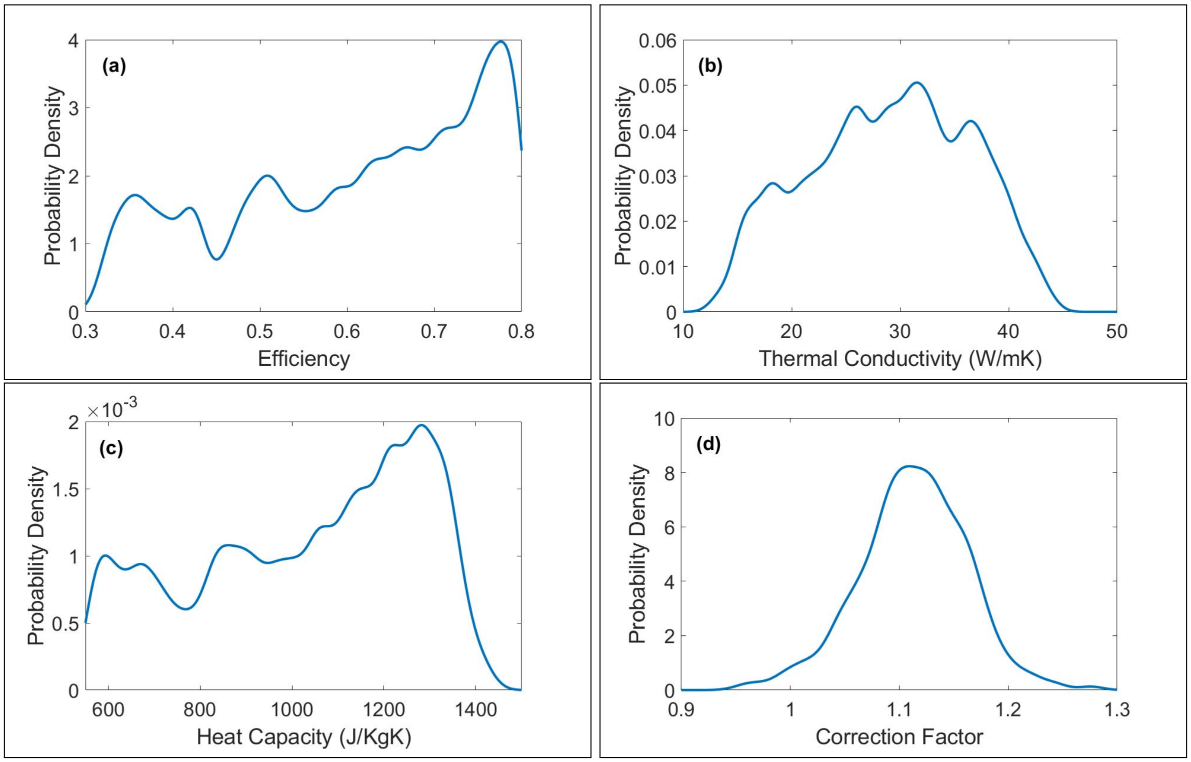

Fig. 2.5. Marginal posterior density functions of parameters in the DSM thermal model after the MCMC-Bayesian calibration with $Ni_{51.2}Ti_{48.8}$ SMA single-track experiments.

Table 2.2. MCMC-Bayesian calibrated parameters in the DSM thermal model: mean values and one standard deviation of MCMC samples after removing the burn-in period.

η	κ (W/m K)	C_p (J/kg K)	C
0.61 ± 0.14	28.9 ± 7.3	1033.6 ± 243.6	1.11 ± 0.05

The mean values and uncertainties of the parameters in Table 4.2 were propagated to the model outcomes used for the calibration, i.e., melt pool width and depth, using forward model analysis. In

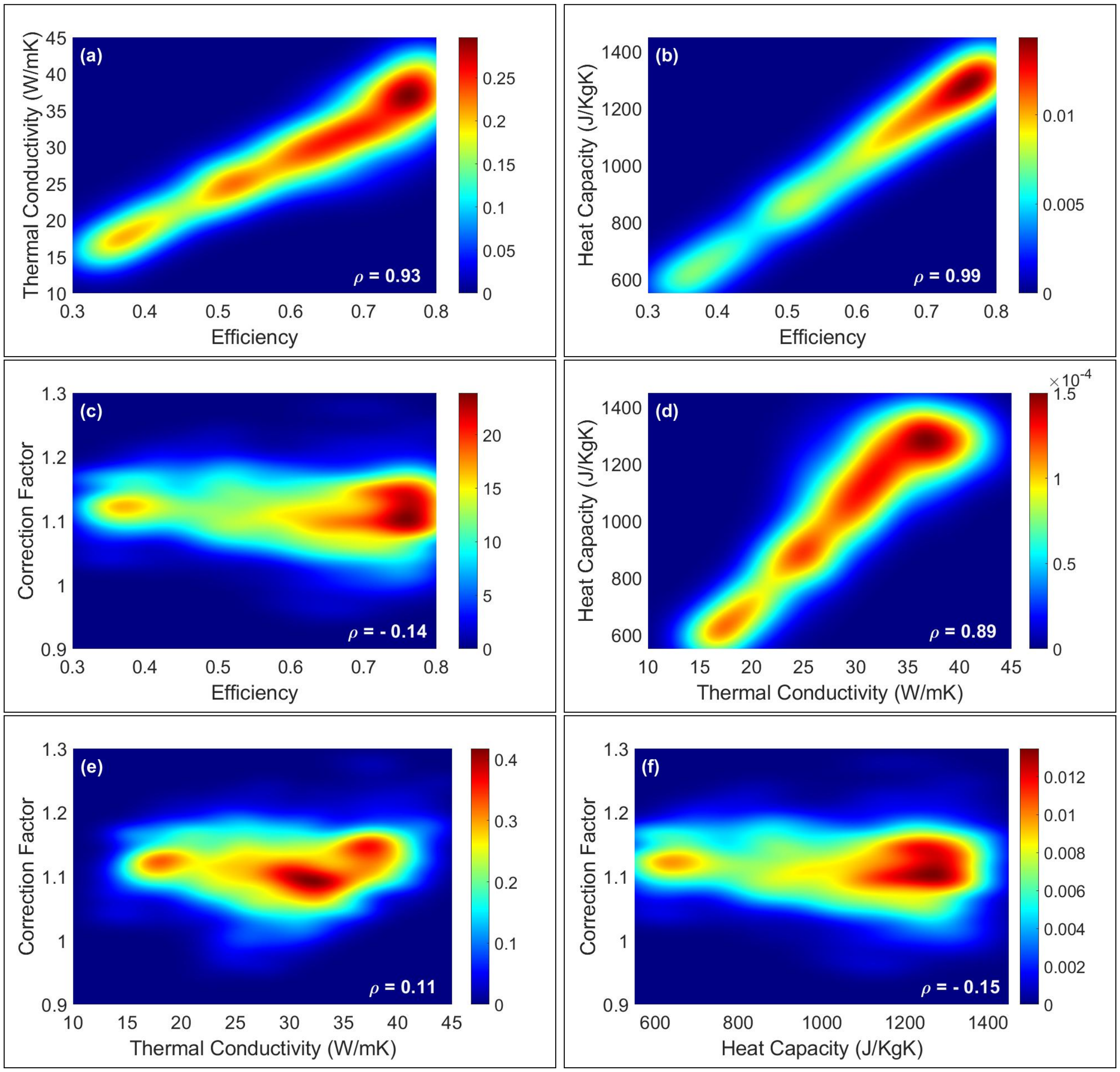

Fig. 2.6. Joint posterior density functions of parameter pairs in the DSM thermal model after the MCMC-Bayesian calibration with $Ni_{51.2}Ti_{48.8}$ SMA single track experiments. ρ represents the Pearson linear correlation.

this uncertainty propagation (UP) method, the MCMC converged samples are run through the model with the keyhole depth correction to obtain the corresponding output samples for melt pool width and depth. Then, 2.5% of the samples are removed from both ends of the sorted output samples to find 95% credible intervals for each output. Figure 4.6 shows the comparison between the calibrated model results and their corresponding experimental data for each training- and test-experimental conditions. In this figure, colors indicate LED values. In part (a) and (b) of this figure, it can be observed that there is excellent agreement between the mean values for the calibrated model results and training-experimental measurements, as deduced from high R^2 values of 0.97 and low RMSE values less than 25 μm. The comparison results for test-experimental conditions in part (c) and (d) also imply good validation of the calibrated model. Therefore, despite missing physics in the model and uncertainties in the experimental data, the calibrated thermal model, utilizing mean parameter values reported in Table 4.2, can be used in Section 2.4 to estimate the evaporation flux and final composition of the matrix after the multi-track multi-layer prints at different process conditions. In this regard, it should be noted that changes in the calibrated material properties due to the change in powder composition from 51.2 to 50.8 Ni [at.%] in Section 2.4 are small and can be ignored.

2.4 Predicting Location-Specific Composition

Illustrated in Figure 2.8, user input, consisting of process parameters and material properties, informs the hierarchical model, enabling chemistry predictions across an AM part. The chemistry of the part can then be linked to properties and performance. The resolution of this hierarchical chain, also known as the forward problem, is an essential task in design under the ICME scheme.

2.4.1 Multi-Layer Model

The Multi-Layer Model (MLM) enables part-level simulation of the LPBF-AM process by utilizing thermal history and geometric relations to replicate the build from the substrate up. In a Cartesian coordinate system, the MLM constructs a 2D slice projected into 3D. The DSM generates melt pool cross-sections along the YZ-plane for multiple tracks and layers, and melt pool lengths are projected in the x-direction to determine melt pool volume. Additionally, if the keyhole

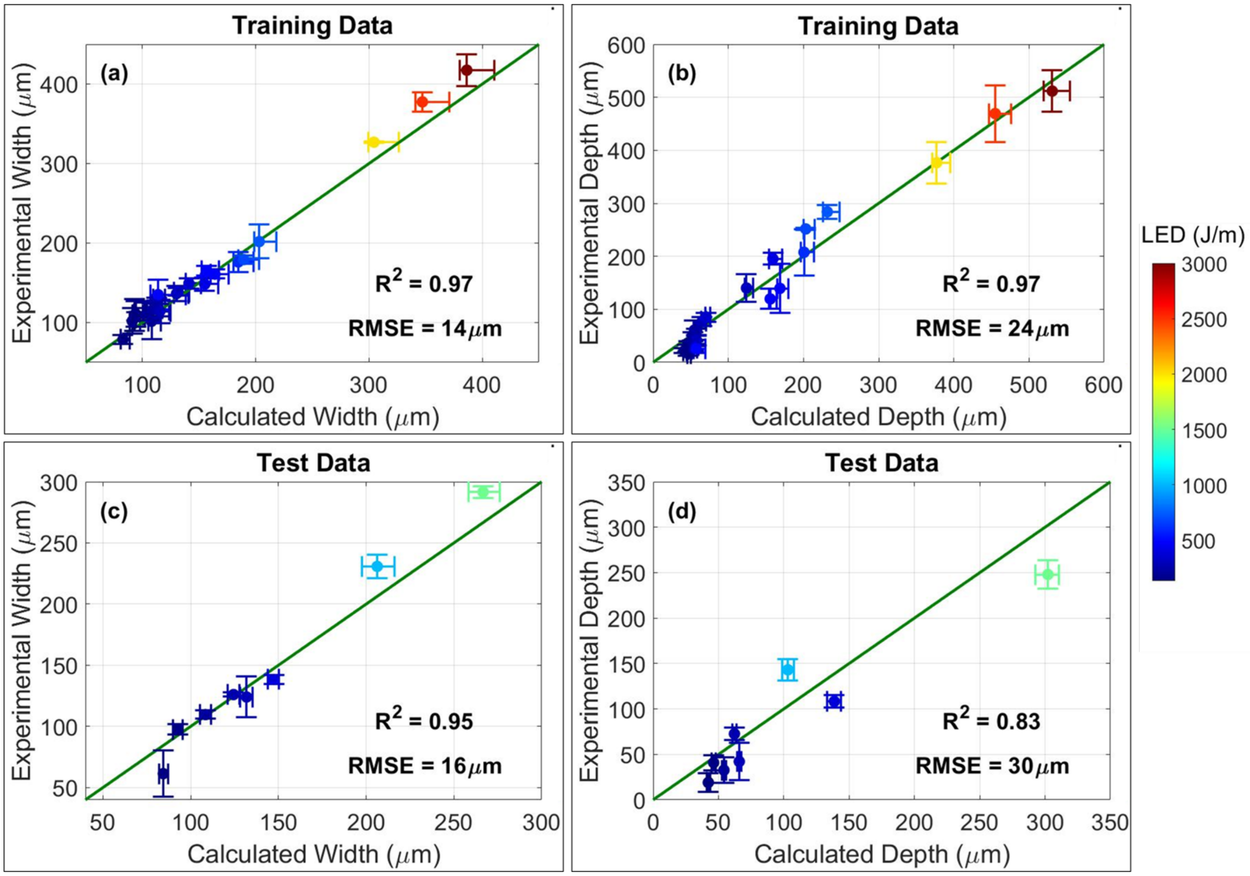

Fig. 2.7. Calibrated model predictions vs. experimental data for the melt pool width and depth produced during the single-track prints of the given $Ni_{51.2}Ti_{48.8}$ SMA. Colors indicate the LED values based on the given experimental input conditions.

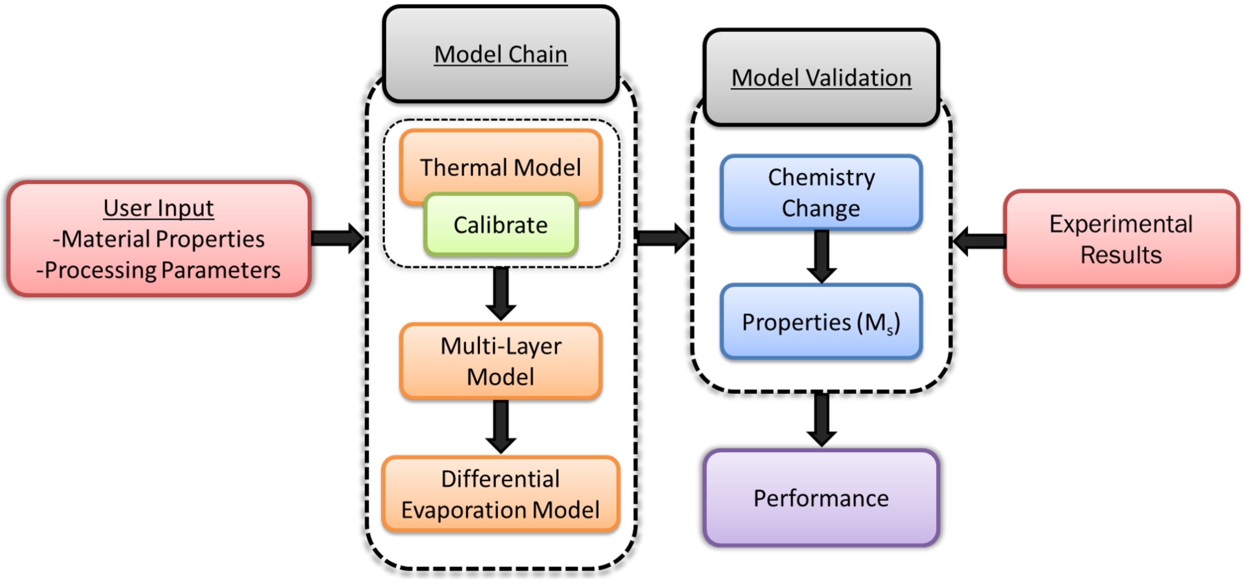

Fig. 2.8. Model methodology. User input is fed into the model chain comprised of the calibrated thermal model, the multi-layer model, and the differential evaporation model. This is followed by model validation with experimental results to determine location-specific chemistry and properties, and ends with an evaluation of performance.

depth correction criteria is met, as discussed in Section 2.3.1.4, adjusted melt pool depths will be utilized by the MLM. Based on processing conditions, portions of each track and layer can also be categorized into steady-state and dynamic regions. In the case of a conventional hatching scan strategy with constant processing parameters and sufficient length, a melt pool generated in the center of a track, a steady-state region, could be extended in either direction to represent the entire steady-state region. However, regions where the process may be more dynamic, such as near the start or end of a track, could have a different thermal history than a steady-state region and should have separate MLM predictions generated. Through the MLM, a 2D slice across the cross-section of multiple tracks and layers in the steady-state region could then represent a substantial portion of the 3D AM part. Additionally, the MLM retains chemistry information for every point within the simulated 3D projection, enabling location-specific chemistry to be predicted and tracked through time, further aiding in location-specific property predictions across the part.

2.4.1.1 Assumptions

Modeling the AM process on a part-level can be taxing on resources, but is necessary for an accurate translation to part properties. In this regard, several assumptions are made in the MLM to improve computational efficiency and retain adequate resolution. These assumptions and their corresponding justification are expressed below; this is proceeded by a more detailed discussion.

1. The intralayer preheat effect is automatically captured by the DSM and drives changes in melt pool dimensions from one track to the next. However, once the difference in dimensions of the current and previous track reaches the desired tolerance, i.e., 10e-15 μm, it is assumed that these steady-state melt pool dimensions can be applied to the remaining tracks in the print layer for the sake of reducing computational cost. This approach could be revised based on scan strategy.
2. The interlayer preheating is assumed to be constant for all layers deposited due to previous experimental work [97, 110] showing homogeneity within an AM part at different print layers, confirming there is sufficient time between layers to reduce preheating effects in our experiments. However, in the case that preheating is significant, it can be implemented in the DSM by adjusting the parameter for background temperature.
3. If the melt pool overlap formed by track N and an adjacent track is sufficiently small, e.g., less than 1% cross-sectional area overlap, the chemistry propagation is considered negligible.

In the case of a single-layer with multiple tracks, the diffusion of heat from one track acts as a preheat for adjacent tracks. This results in a slight variation in melt pool size, affecting several tracks depending on part geometry and process parameters before steady-state dimensions are reached. In the steady-state regions, thermal history, respective melt pool geometry, and melt pool overlap remain approximately constant. Due to this symmetry, a single melt pool can be projected along the steady-state length of a track. The MLM implemented in this study utilizes individual melt pool geometry from the first track until steady-state, whereafter the remaining melt pool dimensions have equivalent dimensions, allowing several melt pools to model an entire layer. Additionally, preheating effects between layers are not considered. This means that melt pool dimensions in each layer are identical to corresponding tracks in the previous layer, and a single layer can be used to model all build layers. Consequently, the steady-state region of the print can be modeled with several melt pools and a significant reduction in computational cost. Furthermore, the cross-sectional area of melt pool overlap with adjacent tracks varies based on processing parameters and intralayer preheating. As the overlap area decreased, the chemistry propagation between the melt pools also decreases. When a melt pool overlap region is sufficiently small, this effect becomes negligible. This simplification aids in reducing the number of melt pool overlaps that need to be evaluated for determining chemistry propagation, through each track and layer. Melt pool overlap is discussed in greater detail in the following section.

2.4.1.2 Melt Pool Overlap

The MLM provides insight on the chemistry propagation throughout a part by constructing the sample from the substrate up and tracking composition for every track and layer. The average composition of each melt pool is calculated based on overlap with melt pools from previous tracks in the same layer, and overlap with tracks in previous layers and/or the substrate. Figure 2.9 illustrates this general relationship between melt pools on adjacent tracks and layers.

In the simplest scenario, Case A, the first melt pool corresponds to the first layer and first track of the build, MP_{L1T1}. This melt pool has an average composition, χ_{L1T1}, given by the volume fraction of powder, $V_{p,L1T1}$, with composition χ_p, and the volume fraction overlap with the substrate, $V_{Ovlp,L1T1|s}$, with composition χ_s. Here, layer thickness is used to define the boundary between the powder and substrate region. Case B then introduces the second melt pool of layer 1, MP_{L1T2}, which overlaps with MP_{L1T1} and the substrate. At this point in time, the entire length of the first track has been processed, meaning the volume encompassed by maximum cross-sectional overlap of MP_{L1T2} with MP_{L1T1} is represented by the volume fraction $V_{Ovlp,L1T2|L1T1}$ having composition χ_{L1T1}. Now, the overlap of MP_{L1T2} with the substrate, $V_{Ovlp,L1T2|s}$, not contained within $V_{Ovlp,L1T2|L1T1}$ must be determined. This can be achieved through Equation 2.7.

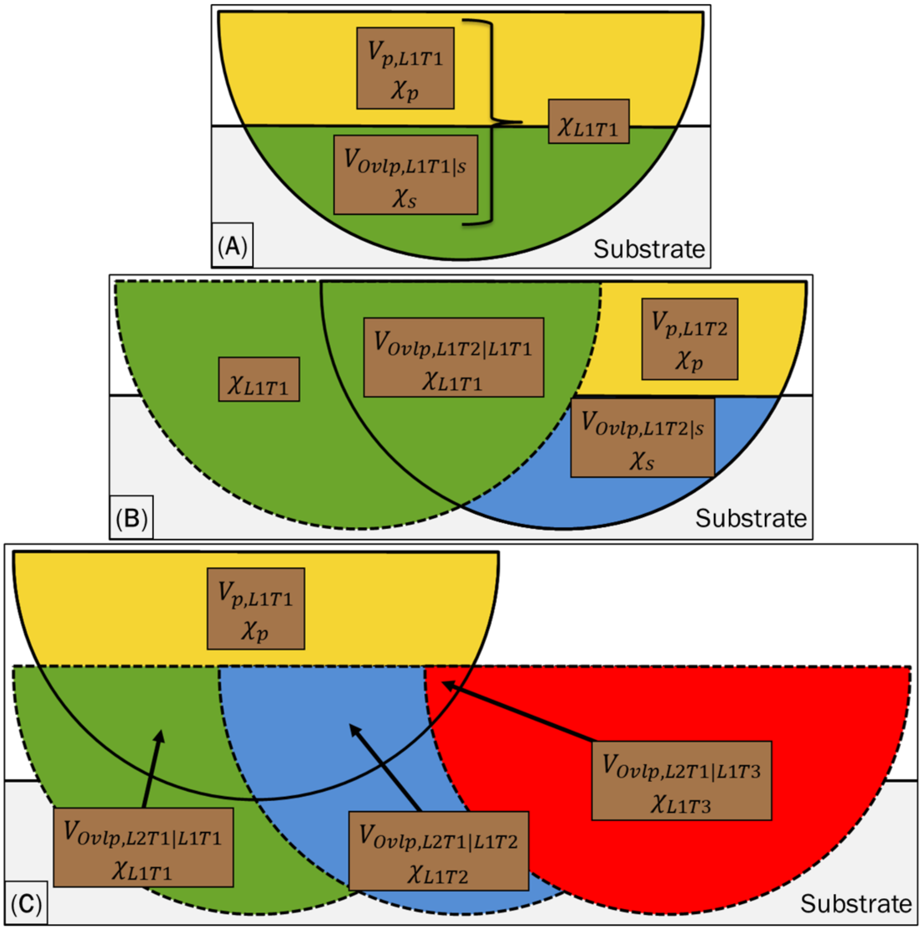

Fig. 2.9. Melt pool overlap and chemistry propagation general relationship. The terms are as follows: V - volume, χ - composition, p - powder, s - substrate, $Ovlp$ - overlap, L - layer, T - track, | - 'with'

$$V_{Ovlp,L1T2|s} \leftarrow V_{Ovlp,L1T2|s} - (V_{Ovlp,L1T2|s} \cap V_{Ovlp,L1T2|L1T1}) \tag{2.7}$$

Here, the intersecting region of the substrate overlap with $V_{Ovlp,L1T2|L1T1}$ is removed from $V_{Ovlp,L1T2|s}$ to redefine the volume fraction overlap of the substrate with MP$_{L1T2}$. The overlap and powder volume fractions and corresponding compositions are then used to determine the average composition of MP$_{L1T2}$,χ_{L1T2} . When considering a conventional snake scan strategy, and constant processing parameters, this procedure for calculating melt pool volume fraction and composition can be extended for the remainder of tracks in the first row. Even though the build process could result in a melt pool overlapping with multiple tracks, it is important to recognize the development of a time hierarchy, where the most recent event in time would be the influencing track. This means that, for any track in the first layer, $L1TN$, it is only necessary to consider overlap with the most recent adjacent track, $V_{Ovlp,L1TN|L1TN-1}$ and substrate, $V_{Ovlp,L1TN|s}$.

Case C follows a similar procedure, but there is added complexity in accounting for overlap with multiple melt pools in a previous layer instead of a constant substrate with constant composition. However, as with same-layer track overlap in a conventional snake scan strategy with constant processing parameters, multi-layer overlap is handled on a time hierarchy. Even though there might be overlap extending through several layers, the only necessary layer overlap to consider is with the layer directly preceding the current position. For MP_{L2T1}, this means consideration of the powder, MP_{L1T3}, MP_{L1T2}, MP_{L1T1}, and their respective volume fraction and composition. $V_{Ovlp,L2T1|L1T3}$ can be determined directly, however $V_{Ovlp,L2T1|L1T2}$ and $V_{Ovlp,L2T1|L1T1}$ require an adjusted application of Equation 2.7. This process can become increasingly complex depending on process parameters, with the number of overlaps and overlap volume fraction strongly dependent on power, velocity, hatch, layer thickness, and material properties. This directly affects the chemistry propagation through the tracks and layers of the simulated part determined by the MLM. However, another important factor affecting composition and warranting consideration is the evaporation of material from the melt pool.

2.4.2 Differential Evaporation Model

The differential evaporation model (DEM) serves to account for the loss of material due to evaporation during the printing process and provide increased accuracy in predicted compositions. The DEM takes direct input from the thermal model, generates a melt pool, and applies a formulation for evaporation to account for material loss and provide an evaporation adjusted predicted chemistry. When utilizing the MLM, the average initial chemistry of each melt pool is fed into the DEM and the resulting chemistry fed back to the MLM. This linkage fully incorporates the effect of evaporation across the simulated sample and predicts chemistry resulting from the culmination of geometric and evaporation effects.

2.4.2.1 Assumptions

The development of the DEM begins with the generation of assumptions, for both the DSM (mentioned in Section 2.3.1) and DEM, used to describe and simplify the involved physics. Equations are formulated, encompassing these physics, to solve for differential evaporation and to predict chemistry. Assumptions for the DEM include:

1. The melt pool follows a mass balance.
2. There is complete mixing within the melt pool.
3. The Kinetic Theory of gases can be applied.

The implications of these assumptions are a solution to the mass flow in and out of the system, a spatially uniform composition of the melt pool, and an evaporation rate formulation derived from the Kinetic Theory of Gases, which itself is built on two postulates [111]:

1. Matter is composed of extremely small molecules, where molecules of the same chemical substance are facsimiles
2. Molecules of a gas are in constant motion → intimately related to temperature

2.4.2.2 Mass Balance

A derivation for mass balance in a control volume was conducted, providing a formulation for chemistry change in a melt pool. Figure 2.10 depicts the mass flow, in and out, of a melt pool in a control volume, whereby mass loss due to evaporation occurs through the melt pool surface, liquid-vapor interface.

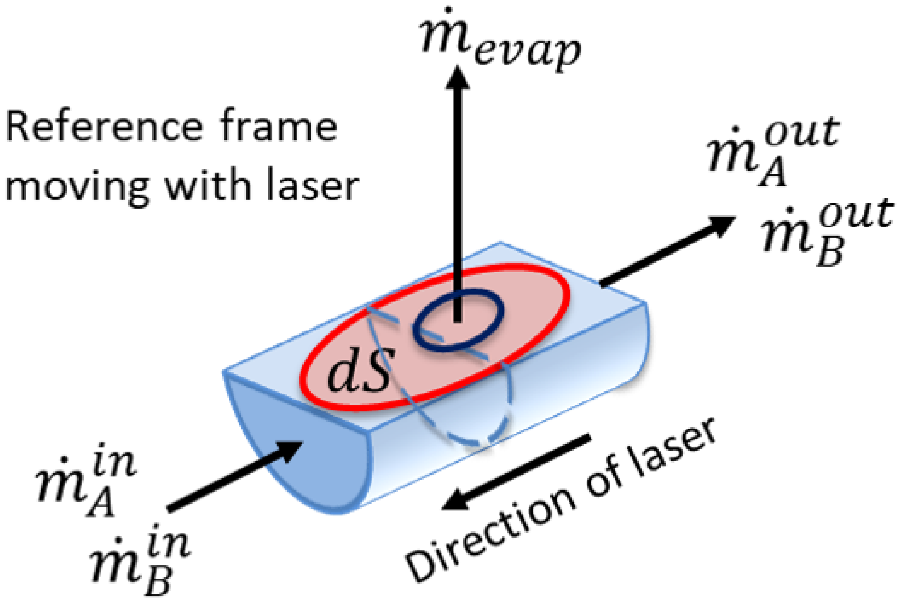

Fig. 2.10. Mass balance of a melt pool in a control volume.This includes mass flow in, mass flow out, and mass loss due to evaporation.

The following relation describes the mass flow through the control volume:

$$\dot{m}^{out} = \dot{m}^{in} - \dot{m}^{evap} \tag{2.8}$$

where $\dot{m}^{in}$ [kg/s] is the mass flow rate into the melt pool, $\dot{m}^{out}$ [kg/s] is the mass flow rate out of the melt pool, and $\dot{m}^{evap}$ [kg/s] is the mass flow rate, due to evaporation, out the top surface of the melt pool. Here, $\dot{m}^{in}$, $\dot{m}^{out}$, and $\dot{m}^{evap}$ are expressed, respectively, as:

$$\dot{m}^{in} = \int_{in} \rho \left(\vec{u} \cdot \hat{n} \right) dA \tag{2.9}$$

$$\dot{m}^{out} = \int_{out} \rho \left(\vec{u} \cdot \hat{n} \right) dA \tag{2.10}$$

$$\dot{m}^{evap} = \sum_{iso=1}^{n} \int_{top} j \left(\chi_A, \chi_B, ..., T_{iso} \right) dS_{iso} \tag{2.11}$$

Where ρ is the density of mass moving in a velocity field $\vec{u} \cdot \hat{n}$ perpendicular to the cross-sectional area of the control volume (defined as the extent of the melt pool) dA, and j is the evaporation flux, dependent on the chemistry of the alloying elements $\left(\chi_A, \chi_B, ... \right)$ and the temperature of interest (T_{iso}), out of the isotherm area (dS_{iso}) corresponding to the temperature of interest. The evaporative flux is a continuous function of both the alloy composition and the temperature. The latter varies spatially across the liquid-vapor interface. To simplify the integral we discretize the liquid-vapor interface into several regions bounded by selected isotherms and assume uniform temperature within each of these subdomains. It should be noted that the boiling isotherm accounts for a majority of the mass loss due to evaporation in the melt pool. Equations 2.9 and 2.10 are reduced to:

$$\dot{m}^{in} = \rho^{in} \omega^{in} u A_{x-s}^{in} \tag{2.12}$$

$$\dot{m}^{out} = \rho^{out} \omega^{out} u A_{x-s}^{out} \tag{2.13}$$

Where $\rho * \omega \ [kg/m^3]$ represents the density of the alloy multiplied by the alloying element's weight fraction, and $A_{x-s} \ [m^2]$ is the front projected area of the melt pool.

If the melt pool is thoroughly mixed, we can then assume that the liquid has a spatially uniform composition, the chemistry of the alloying elements can be considered constant. As a result, equation 2.11 becomes:

$$\dot{m}^{evap} = \sum_{iso=1}^{n} j\left(\chi_A, \chi_B, ..., T_{iso}\right) S_{iso} \tag{2.14}$$

From here, the mass balance (eqn. 2.8) may be re-written as a first-order steady-state solution for each alloying element i by substituting equations 4.9-2.14:

$$\dot{m}_i^{out} = \left(\rho_i^{in} * \omega_i^{in}\right) u A_{x-s}^{in} - \sum_{iso=1}^{n} j_i\left(\chi_A, \chi_B, ..., T_{iso}\right) S_{iso} \tag{2.15}$$

2.4.2.3 Evaporation Rate

The DEM follows a sequence of several calculations, completed for each alloying element (Ni and Ti in NiTi), to predict the chemistry at a location in an AM part:

1. Calculate Equilibrium Vapor Pressure, as a function of isotherm temperature and incoming chemistry.
2. Determine Evaporation Rate, according to eqn. 2.18.
3. Conduct Mass Balance, as described in eqn. 2.15.

In order to calculate the equilibrium vapor pressure, $\bar{p}_i\ [atm]$, the standard pressure of the alloying element, $p_i^\circ\ [atm]$, must first be evaluated. This was accomplished through Antoine's equation (eqn. 2.16), derived from the Clausius-Clapeyron relation, where A, B, and C are Antoine coefficients, listed in Table 2.3, and $T\ [^\circ C]$ is the temperature of interest [49]:

$$p_i^\circ = 10^{\left(A - \frac{B}{C+T}\right)/760} \tag{2.16}$$

The equation for equilibrium vapor pressure, for each alloying element, is then:

$$\bar{p}_i = p_i^\circ a_i \tag{2.17}$$

Where a_i is the activity of the respective alloying element. Activity values were generated through Thermocalc 2020b TCHEA4 database for temperatures ranging from T_{melt}-T_{boil} for a

Table 2.3. Antoine coefficients for Ni and Ti.

Element	A	B	C
Ni	-8.75	17882.38	134.99
Ti	8.90	20948.99	190.76

desired composition. The evaporation rate for each element is then determined through the Kinetic Theory of Gases as:

$$j_i = 44.331\bar{p}_i\left[\frac{M_i}{T}\right]^{\frac{1}{2}} \tag{2.18}$$

where j_i [g/(cm^{2}s)] is the vaporization rate of species i, $\bar{p}_i$ $[atm]$ is the equilibrium vapor pressure of i, M_i $[g]$ is the molecular weight of i, and T $[K]$ is the absolute temperature. This is followed by the mass balance (eqn. 2.15) for each alloying element. From the mass balance, the mass flow out of the melt pool can be related to the weight fraction of Ni and Ti along with the melt pool's updated chemistry. This procedure is repeated for multiple melt pools, based on scan strategy and sample size, to consider cumulative thermal effects from adjacent layers and tracks on the location-specific chemistry prediction of the AM part.

The model took a quick and simple approach to chemistry prediction, utilizing the thermal history of a designated point of interest. This thermal history was segmented based on the number of desired isotherms, with surface area and interaction time calculated for each. The mass balance was resolved and chemistry predicted.

2.4.3 Experimental Procedure

For the validation of the DEM, gas atomized $Ni_{50.8}Ti_{49.2}$ [at.%] powder with a *d*80 of 38 μm was used to fabricate $10 \times 10 \times 10$ mm^3 cubes. As shown in Table 3.2, the laser power and scanning velocity were in the range of 60~240 W and 80~1330 mm/s, respectively. The Oxygen level in the print chamber during printing and the layer thickness were 500 ppm and 40 μm, respectively. The volumetric energy density ($VED = \frac{P}{uhL_t}$, where h is hatch distance and L_t is layer thickness) for these 21 cube prints vary from 52.9 to 234.4 J/mm^3.

A differential scanning calorimetry (DSC) sample of the powder was solution heat-treated at 950 °C for 1 hour under protective argon atmosphere in order to determine the transformation temperatures of the powder in single phase (without any precipitates which may change the transformation temperatures and the matrix composition). In addition, DSC samples with 3 mm diameter and 1 mm thickness were cut from the printed cubes using wire EDM, and then solution heat-treated at 800 °C for 1 hour in argon, again in order to eliminate any second phases, residual stresses or any other microstructural features that may affect the transformation temperatures. This is critical because the Ni content of the prints are indirectly determined using the transformation temperatures, as explained in the following section in detail. A TA Instruments Q2000 DSC is used to measure the transformation temperatures of both powder and the printed cubes. Two thermal cycles were performed during the DSC measurement at a heating/cooling rate of 10 °C/min between -150 °C to 150 °C, and the transformation temperatures listed in Table 3.2 were extracted from the second cycle using the intersecting tangent method [112]. These transformation temperatures include martensite start temperature, M_s, martensite finish temperature, M_f, austenite start temperature, A_s, and austenite finish temperature, A_f. The following section will focus on M_s, however, a similar procedure could be used for the remaining transformation temperatures.

2.4.4 Nickel Content and Martensitic Transformation Temperature (M_s)

In NiTi SMA literature, it is well-known that determining the exact Ni content of Ni-rich NiTi SMAs at the desired level of accuracy is very challenging, if not impossible, using known chemistry measurement techniques [70, 113, 114]. This is due to the extreme sensitivity of martensitic transformation temperature to the Ni content in materials with Ni contents greater than 50 at.% as shown in Figure 2.11. Such chemical sensitivity requires the determination of Ni content on the order of 0.01 at.% level in bulk samples. As seen in Figure 2.11, there are two distinct regions defined by the M_s-Ni relationship, where M_s is the martensite start temperature. At Ni contents less than ~49.8 at.%, M_s remains relatively constant, while a strong negative trend is seen with Ni content greater than ~49.8 at.%. This negative slope becomes larger as the Ni content approaches 51

Table 2.4. Process parameters and the transformation temperatures after solution heat treatment for the 21 cubes manufactured from $Ni_{50.8}Ti_{49.2}$ powder.

P (W)	u (mm/s)	h (μm)	LED (J/mm)	VED (J/mm^3)	M_s (°C)	M_f (°C)	A_s (°C)	A_f (°C)
160	1080	70	148.1	52.9	-19.81	-33.29	-3.46	9.37
65	297	100	218.9	54.7	11.23	-18.81	9.81	41.40
240	1330	80	180.5	56.4	-22.9	-29.21	-1.11	11.17
200	1080	80	185.2	57.9	-23.61	-36.61	-6.39	7.44
160	830	80	192.8	60.2	-18.62	-29.62	-2.61	9.37
200	830	100	241.0	60.2	-27.70	-35.90	-6.33	3.94
160	580	110	275.9	62.7	-18.75	-27.66	-1.16	11.09
120	330	130	363.6	69.9	3.81	-10.56	16.27	32.00
80	330	80	242.4	75.8	12.78	-4.05	22.83	42.34
96	297	100	323.2	80.8	15.10	-5.24	24.25	44.40
65	200	100	325.0	81.3	27.35	10.62	37.61	57.34
96	350	80	274.3	85.7	21.93	-3.65	26.51	50.25
60	160	100	375.0	93.8	38.59	19.17	47.52	70.19
96	250	100	384.0	96.0	20.95	1.87	34.24	51.24
96	297	80	323.2	101.0	21.37	-8.47	20.25	51.14
96	200	100	480.0	120.0	32.58	14.93	43.76	62.63
60	120	100	500.0	125.0	54.38	33.13	63.39	86.45
72	120	120	600.0	125.0	47.57	28.31	57.42	79.42
60	80	120	750.0	156.3	66.79	44.49	78.19	99.79
65	80	120	812.5	169.3	69.95	48.12	81.97	102.83
60	80	80	750.0	234.4	70.76	52.97	89.74	106.25

at.%, and corresponds to a change of over -100 [K/Ni at.%]. This demonstrates a strong sensitivity of M$_s$ to Ni content in the NiTi system, and reinforces the importance for accurately predicting composition to tailor location-specific properties. Therefore, in the present study we used the measured M$_s$ temperatures to calculate the Ni content of the printed samples as described below and compare these with the Ni contents predicted using the DEM.

Nickel content is determined from the M$_s$ temperature attained through DSC by utilizing an empirical relation for Ni $[at.\%]$ and M_s $[K]$ [70]:

$$M_s(\chi_{Ni}^T) = (A + B * \chi_{Ni}^T) + C * D^{(\chi_{Ni}^T - 50)} \tag{2.19}$$

where M_s $[K]$ is the martensite start transformation temperature, A is 4511.2373, B is -83.42425, C is -0.04753, D is 204.86781, and χ_{Ni}^T is the true Ni content [at.%].

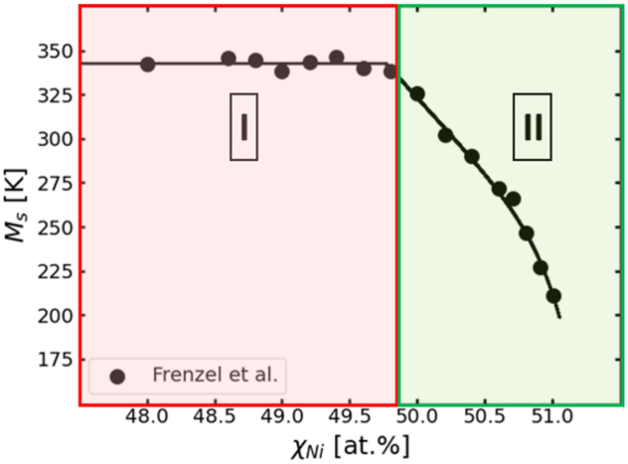

Fig. 2.11. Nickel content and corresponding M_s for multiple NiTi samples. Region I: Non-Invertible, Region II: Invertible

2.5 Model Validation Results and Discussion

Following the previously stated methodology, the combined DSM-MLM-DEM was used to model the printing process of the 21 solution heat treated (SHT) 50.8 Ni [at.%] samples (mentioned in Section 2.4.3) and predict Ni content after the thermal process. Pertaining to the DSM, relevant input parameters are listed in Table 2.5. Additionally, the surface area of each melt pool was binned into 5 equally spaced isotherms, spanning NiTi's melting to boiling temperature (1312 - 3187 °C), for the application of the DEM.

Table 2.5. Model parameters and thermophysical properties.

P (W)	υ (mm/s)	h (μm)	L_t (μm)	η	κ (W/m K)	C_p (J/kg K)	C	σ_x (μm)	ρ (kg/m^3)	T_0 (°C)	$f_{T_{melt}}$	$f_{T>T_{melt}}$
60-240	80-1330	70-130	40	0.61	28.9	1033.6	1.11	20	6471	23	3	30

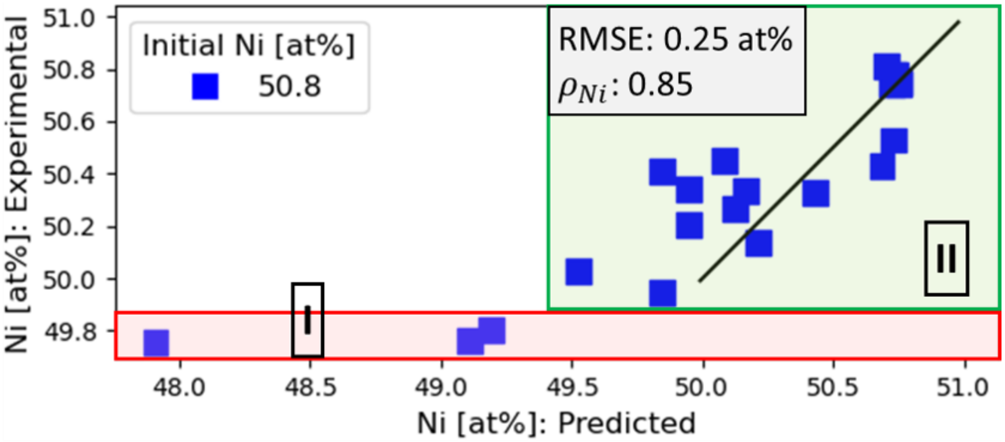

Fig. 2.12. Model predictions of Ni [at.%] compared with experimental values for LPBF 50.8 Ni [at.%] samples.

Figure 2.12 compares the predicted Ni [at.%] for each of the 21 SHT samples with the Ni [at.%] derived from experiments. The data is divided into two regions based on the M_s and Ni relationship described in Section 2.4.4 and Figure 2.11. In Region I, the experimentally derived Ni values reach a limit of approximately 49.8 [at.%]. This is expected due to the non-invertible relationship of calculating Ni content from M_s, when M_s is approximately 335 K or higher. However, the combined DSM-MLM-DEM is not limited by this conversion, and directly calculates Ni compositions that may dip below this 49.8 [at.%] threshold. This is demonstrated by several points in Region I with the predicted Ni [at.%] below 49.8. Unlike Region I, the invertible relationship of calculating Ni content from M_s can be used in Region II. Both empirical and predicted Ni values are superimposed on a 45-degree line, demonstrating over- and under-predicting values that result from a combination of errors corresponding to the lack of knowledge about the parameters, possible missing physics or assumptions in DSM-MLM-DEM, and experimental measurements. Due to the non-invertible nature of Region I, only points located in Region II were considered in calculating the RMSE of 0.25 Ni [at.%] and the Pearson correlation, ρ_{Ni}, of 0.85, suggesting a strong positive linear correlation between model predictions and experiment values. This means that the hierarchical DSM-MLM-DEM approach is capable of predicting Ni content in a range *well within the uncertainty of ± 0.5 [at.%]* for some of the chemistry measurement techniques such as wavelength dispersive spectroscopy (WDS) and inductively coupled plasma atomic emission spectroscopy (ICP-AES), and composition predictions followed expected trends, even in Region I. It should be noted here that although ICP-AES can be accurate to parts per million ranges for low-level constituents, the accuracy can be as low as ± 2% of the absolute value for the major constituents [115]. It is also important to note that the predictions were achieved with only a calibrated analytical thermal model being fed to the MLM and DEM, which can be much faster than numerical thermal models (e.g. finite element models).

Predicted Ni [at.%] can then be related to transformation temperature, $M_s\ [K]$, by utilizing Equation 4.15. Figure 4.10 illustrates the comparison between predicted and experimental DSC-measured M_s.

The RMSE for the 21 samples is 18.65 [K], which is again *well within* the range of uncertainty that a WDS or ICP-AES to M_s measurement might provide ($\pm 50K$). Additionally, the Pearson correlation, ρ_{M_s}, is 0.85, again suggesting a strong linear positive correlation between model predictions and experiment values. Due to the nature of the M_s-Ni relationship, errors in predicted Ni content are magnified with M_s, as is shown with several points predicting M_s values 30-45 K larger than corresponding empirical measurements. -However, some of this error could be

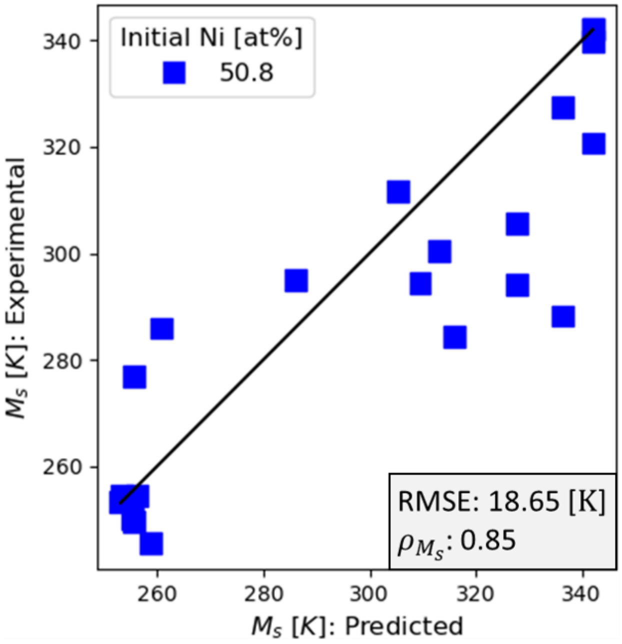

Fig. 2.13. Model predictions of M_s compared with empirical values for LPBF 50.8 Ni [at.%] samples.

imparted on the fact that the analytical M_s-Ni relationship is an approximation, and could be refined with supplementary experiments. Additionally, as mentioned earlier, the compounding effect of assumptions in the DSM-MLM-DEM could have impacted predicted values, some more-so than others. This requires further inspection of the relationship between processing parameters and structure, melt pool volume and surface area, as well as properties.

2.6 Conclusion

In metal AM, accurate resolution of the forward problem (predicting location-specific chemistry for a specific set of manufacturing processing parameters) is a necessary step preceding solution of the inverse problem (determining manufacturing processing conditions to achieve location-specific chemistry). With NiTi as a model material system, this first step is achieved by utilizing several hierarchically coupled physics-based models, calibration with experiments, and validation. The model chain begins with the DSM analytical model, enabling the simulation of thermal history based on processing parameters and material properties. A depth correction factor to account for the keyholing phenomenon, determined using an experimentally obtained criterion, is considered, and the DSM is calibrated against the width and depth measurements of $\mathrm{Ni}_{51.2}\mathrm{Ti}_{48.8}$ single-track experiments in the Bayesian context, providing a probabilistic calibrated value for heat capacity, conductivity, efficiency, and the depth correction coefficient. Following this, the DEM's initialization is 2-fold, where chemistry predictions are made for a melt pool based on the effect of evaporation and melt-pool overlap, and geometric considerations are evaluated and updated through the multi-layer model (MLM). By considering multiple-layers during the AM process, the effect of chemistry propagation due to melt pool overlap across a part is appropriately represented; followed by the combined consideration of the DSM-MLM-DEM that enables the prediction of Ni content in LPBF AM $\mathrm{Ni}_{50.8}\mathrm{Ti}_{49.2}$ parts with a smaller range of uncertainty (RSME: 0.25 Ni [at.%]) than typical chemistry measurement techniques such as WDS and ICP-AES provide. Additionally, the martensitic transformation temperature, M_s, corresponding to these predictions were evaluated (RSME: 18.65 K), providing a complete transition from process to structure to properties. The DSM-MLM-DEM chain has thus shown its utility for predicting location-specific chemistry and solving the forward problem for LPBF AM $\mathrm{Ni}_{50.8}\mathrm{Ti}_{49.2}$, as well as providing a path to model NiTi's PSPP relationship.

Although the results here are promising, several considerations can be made for the improvement of this model and future work. The MLM is currently limited in its scope regarding the steady-state assumptions, where predictions could be improved by allowing for more complex patterns and full resolution of chemistry propagation. Additionally, the DSM's ability to switch processing parameters mid-scan would enable the modeling and chemistry prediction of more complex printing strategies and should be tested. From the computational perspective, the most important aspect in solving the inverse design problem is the introduction of a cheap and effective forward model. Full uncertainty propagation analysis through the coupled models is also needed to establish uncertainty bounds on predicted quantities. The current DSM-MLM-DEM will be tested in this regard to provide, potentially through training a cheaper surrogate model, processing parameters that will achieve a desired chemistry, and subsequently validated with experiments. In this context, the detection and quantification of prominent uncertainty sources in modeling are also essential tasks. Finally, as was mentioned in the Introduction, we will be using this forward model within an inverse design framework to achieve *designable and controllable* location-specific actuation in 3D-printed NiTi-based SMA components.

3. INVERSE DESIGN OF ADDITIVELY MANUFATURED NITI SHAPE MEMORY ALLOY THROUGH AN INTEGRATED COMPUTATIONAL FRAMEWORK

3.1 Overview

As technological advancements further the integration of data and machine learning with manufacturing tools and processes, additive manufacturing (AM) sits at the forefront of development in materials design. Additionally, the desire of industry to improve the utility, performance, and reliability of AM parts has driven the need for tools or parts with specific property requirements. The subsequent problem is determining how to fabricate an AM component which meets the desired performance requirements. In this study, an integrated computational materials engineering framework composed of data-driven and and physics-based models is leveraged towards the design of laser powder bed fusion (LPBF) AM NiTi shape memory alloy with tailored location-specific chemistry and properties. A sensitivity analysis is conducted for input parameters across the core modeling components consisting of a thermal model to simulate time-temperature history during fabrication, a multi-layer model to account for melt pool overlap and chemistry propagation across a component, and a differential evaporation model to account for changes in chemistry due to material evaporation. A surrogate model is then developed to aid in computational efforts, for which a sensitivity analysis on the design variables of laser power, laser speed, and hatch spacing is conducted. This is followed by an investigation of constraints, bounds, and the design space through the development of process maps. Further, gradient-based sequential least squares quadratic programming and differential evolution genetic algorithm optimization techniques, targeting specific Martensite start transformation temperatures in LPBF AM $Ni_{51.2}Ti_{48.8}$ in addition to minimizing overall fabrication time, are employed on the surrogate model to efficiently solve the inverse design problem. After parameter tuning and scaling, a global optimum solution of the design variables of power, velocity, and hatch spacing for a target transformation temperature were found.

3.2 Introduction

Additive manufacturing (AM) has disrupted industry through the integration of computer-aided engineering, data, and machine learning to address critical materials development and design problems [116, 117]. This has been met with rapid progression and the curation of material-specific process parameters to successfully fabricate new and improved AM components for the energy, medical, automotive and aerospace industries [118–120]. Among these materials include Ti-6Al-4V, stainless steels, and NiTi shape memory alloys (SMAs). In particular, the design freedom, geometric complexities, and fit-for-purpose fabrication offered by AM has provided an opportune setting for the design of NiTi SMAs with tailored properties.

Although NiTi is desired for its shape memory effect, superelasticity, low stiffness, and biocompatibility, its high reactivity and ductility make it a poor candidate for traditional manufacturing techniques which require processing and machining [121, 122]. These detrimental qualities can be avoided through additive manufacturing, whereas functional properties are concurrently benefited and further enhanced through the improved control and freedoms afforded by the fabrication process. Further, by leveraging the AM design space to modulate process parameters, the design and control of location-specific properties of NiTi SMA can be achieved [123, 124]. It was shown that by adjusting hatch spacing between 35 μm and 120 μm for separate regions of a print, the input volumetric energy energy (VED) and resulting Martensite transformation temperature, M$_s$, varied by 421 J/mm^3 and over 60 K, respectively. This variation in spatial properties based on energy input can then be explained through the distinct difference in thermal history and direct effect of temperature on evaporation during fabrication.

Due to the potential for material exposure to repeated and extreme thermal events during the AM process, the evaporation of alloying elements from the melt pool can result in final compositions and properties differing from the original powder composition and properties. In NiTi SMAs, the significantly larger volatility of Ni compared to Ti results in preferential Ni evaporation and loss during fabrication [125]. Variations in transformation temperature of 80 K to 100 K are shown to be the consequence of extreme sensitivity to Ni content, resulting from changes of just 1 at%. An important finding, the ability to leverage the inherent evaporation caused by additive manufacturing would enable greater control over the designability and tailored location-specific properties of NiTi SMAs.

Hindering the accelerated development of components through additive manufacturing is an inherently complex process-structure-property-performance (PSPP) relationship, making the investigation and analysis of process parameters for design a challenging and extensive task [126]. However, the combination of physics-based and data-driven models through an integrated computational materials framework (ICME) provides a means to decipher and exploit AM PSPP networks. Ranaiefar et al. [14] developed and applied a fast-acting framework, ideal for screening PSPP trends and guiding experiments, towards the accelerated design of laser powder bed fusion (LPBF) NiTi SMAs. Through this calibrated and validated framework, both Ni content and M_s were predicted based on process parameters and shown to accurately align with experimental values and trends. With a solution to the forward modeling problem, this framework can now be applied towards inquisitions for inverse design. In this sense, a solution to the question of 'given a desired property, what are the required process parameters' is sought.

In this study, a validated ICME framework is leveraged for the inverse design of LPBF AM $Ni_{51.2}Ti_{48.8}$ SMAs. A sensitivity analysis of the complete framework is conducted to evaluate the effect of input parameters on the variance of predicted M_s. Further, a surrogate model is developed from the ICME framework to reduce computational cost and enable the efficient exploration of design space through several design variables, laser power, laser speed, and hatch spacing. Process maps are also developed as tool to aid in cost-effective design, providing insight on PSPP trends. Additionally, a multi-objective function is formulated to minimize the error between a target and predicted Martensite starting transformation temperature, and to minimize the fabrication time for additively manufacturing the component. Both a gradient based sequential least squares quadratic programming and differential evolution genetic algorithm are applied in this endeavor. This is followed by parameter tuning and scaling, after which a global optimum solution of design variables for the inverse design of a AM NiTi component with desired M_s properties is presented.

3.3 Problem Formulation

The main issue to be addressed is the efficient determination of required process parameters to achieve a target objective. More specifically, this study seeks to determine the optimal processing parameters for the LPBF AM of $Ni_{51.2}Ti_{48.8}$ to achieve a desired material property. With an expansive design space and the potential for multiple solutions, consideration should also be made to further constrain the viable process parameters. One potential avenue for this is considering a second object function to reduce the overall fabrication time of a component by leveraging laser speed and hatch space values at the upper end of tolerable design constraints, effectively translating to improved production rate in industry.

3.3.1 Objective

The main objective is then to achieve the desired transformation temperature, M_s, of the material system by changing the additive manufacturing processing parameters while satisfying the machine and printability requirements for a given initial powder composition. The secondary objective is to minimize production time. These objectives can be defined as:

$$\begin{bmatrix} J_1 \\ J_2 \end{bmatrix} = \begin{bmatrix} |y - M_{s,Predicted}| \\ Production\ Time \end{bmatrix}$$

where $M_{s,Predicted}$ is the predicted transformation temperature, y is the target M_s, and the design variables are:

$$\begin{bmatrix} x_1 \\ x_2 \\ x_3 \end{bmatrix} = \begin{bmatrix} Power\ [W] \\ Velocity\ [mm/s] \\ Hatch\ [\mu m] \end{bmatrix}$$

The objective functions would then be:

$$MinJ_1(x_1, x_2, x_3, y)$$

$$MinJ_2(x_2, x_3)$$

3.3.2 N^2 Diagram

The model framework, discussed in greater detail in Section 3.4, can be decomposed into four modules to be used in this optimization problem. These include the discrete source (thermal) model (DSM), the multi-layer model (MLM), the differential evaporation model (DEM), and the optimization module. As shown in Figure 3.1, each module can be represented by a block diagram alongside their inputs and outputs.

The relation between the block diagrams can be visualized through the N^2 matrix as shown in Table 3.1. This matrix represents the functional interfaces between different elements of the system.

Table 3.1. Order N^2 matrix.

N^2 Matrix					
In	P, υ, h			Target M$_s$, P$_{max}$, υ_{max}	
	DSM	MP$_{w,l,d}$			
		MLM			
			DEM	M$_s, \chi$	
	P, υ, h			**Optimizer**	M$_s, \chi$
					Out

The melt pool, MP, width (w), depth (d), and length (l) are the main outputs of the DSM, which utilizes a majority of framework input parameters, including laser power , P, laser speed, υ, and hatch spacing, h. This output informs the MLM, which in turn informs the DEM with melt pool geometry and melt pool overlap. From here, a prediction of Ni composition, χ and M_s is attained. This prediction is then evaluated by the optimizer, in conjunction with the fastest potential build

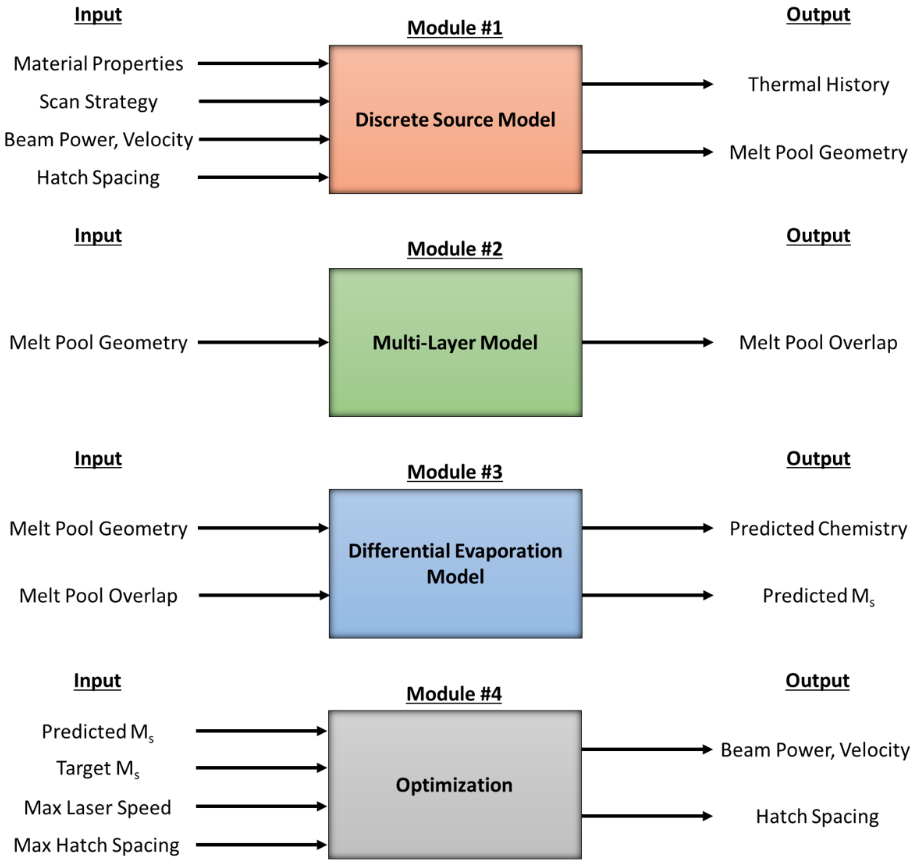

Fig. 3.1. Block diagram for the different framework modules.

time and the build time corresponding to the predicted M_s, providing updated design variables to test in an effort to minimize the objective functions.

3.4 Model Framework

A model has been created accounting for the thermal process of the 3D printing process to determine melt pool geometry and overlap, melt pool evaporation loss, chemistry propagation, and corresponding Nickel composition and transformation temperature of a NiTi part [14]. Illustrated in Figure 3.2, this ICME framework is further developed and integrated with optimization techniques for the purpose of inverse design. User input, consisting of process parameters and material properties, informs the hierarchical model, enabling chemistry predictions across an AM part. The chemistry of the part can then be linked to properties and performance. The resolution of this hierarchical chain, also known as the forward problem, is an essential task in design under the ICME scheme. However, by applying an optimization technique to the objective function of minimizing J_1, the workflow serves to answer the inverse problem of providing design variables that will satisfy the post-printing material property criteria.

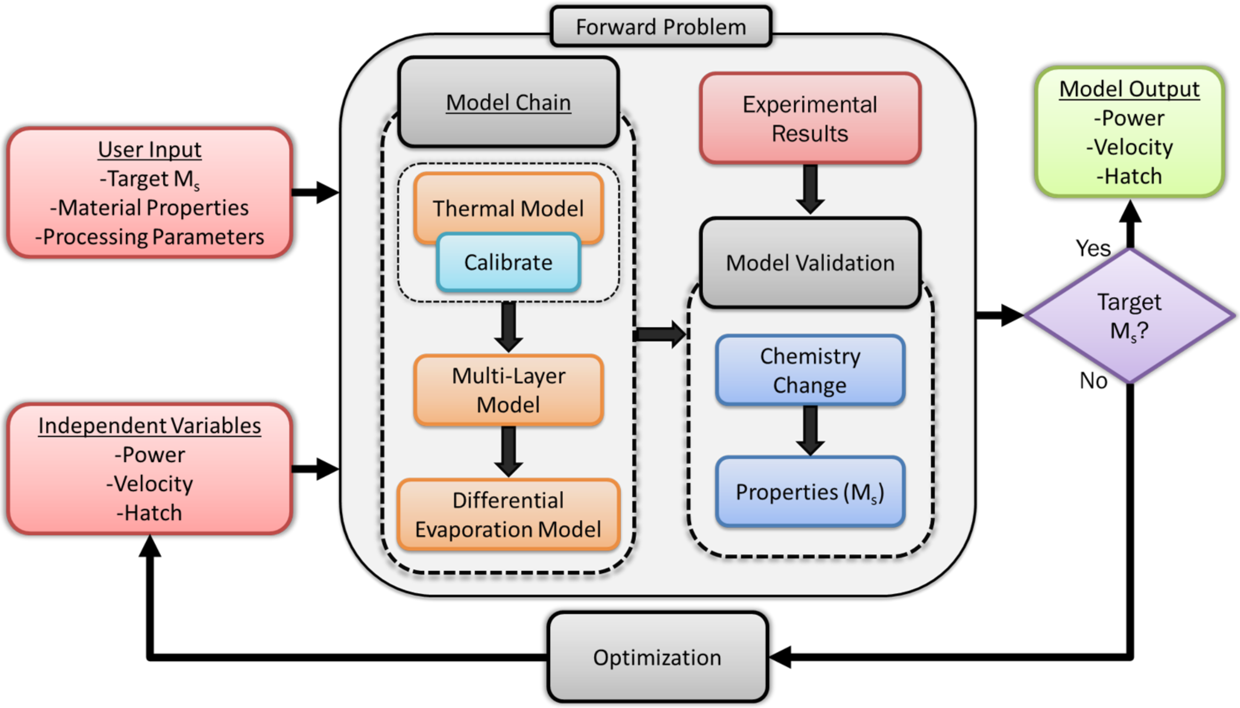

Fig. 3.2. Model predictions of Ni [at.%] compared with experimental values for LPBF 50.8 Ni [at.%] samples.

As part of the framework development, the model was calibrated and validated with $Ni_{50.8}Ti_{49.2}$ experiments, predicting Ni content and M_s in agreement with experimental measurements and trends. M_s was determined through a semi-analytical equation determined through Ni content and corresponding M_s measurements [70]:

$$M_s(x_{Ni}) = (4511.23 - 83.42x_{Ni} - 0.0475 * 204.87^{x_{Ni}-50}) \tag{3.1}$$

Table 3.2 provides relevant process parameters, corresponding linear and volumetric energy density, and measured solution heat treated M_s values for experiments used in the framework validation. These values, and limits of the 3D printer, will be used as a guide in the current work for design parameter constraints and bounds discussed in Section 3.4.3.

3.4.1 Sensitivity Analysis of Model Inputs

Prior to applying the multi-objective optimization approach on the model framework, a sensitivity analysis has been conducted to provide insight on the significance of input parameters on the output variance of predicted Ni content and M_s. Figure 3.3 illustrates the effect of preheat temperature, varied from 20 °C to 600 °C, for three separate sets of design variables of the $Ni_{50.8}Ti_{49.2}$ builds. From Table 3.2, laser power, laser velocity, and hatch space values corresponding to the lowest VED at 52.9 J/mm^3, largest VED at 234.4 J/mm^3, and a VED close to the midpoint of these two values (medium VED) at 120.0 J/mm^3, are are chosen to capture and demonstrate the effect of preheat temperature across the experimental design space.

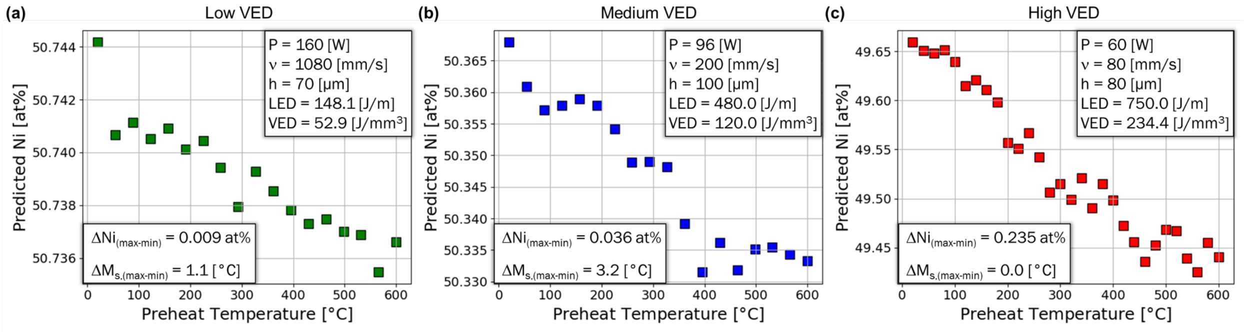

Fig. 3.3. Preheat sensitivity and resulting change in Ni content and M_s for LPBF $Ni_{50.8}Ti_{29.2}$ as predicted by the calibrated ICME framework for several parameter sets spanning the experimental range of VED: (a) Low VED (b) Medium VED (c) High VED.

As expected, across all VED cases it is shown that with increasing preheat temperature there is a decrease in the value of predicted Ni content. For the low VED case it is shown that the difference in predicted Ni content when considering a preheat temperature of 600 ° C as compared to 20 °C (approximately room temperature) is 0.009 at%, corresponding to a 1.1 °C difference in M_s.

Table 3.2. Process parameters and corresponding solution heat treated martensite start transformation temperature for 21 cuboid specimen manufactured from $Ni_{50.8}Ti_{49.2}$ powder.

P [W]	v [mm/s]	h [μm]	LED [J/mm]	VED [J/mm^3]	SHT M_s [°C]
160	1080	70	148.1	52.9	-19.81
65	297	100	218.9	54.7	11.23
240	1330	80	180.5	56.4	-22.9
200	1080	80	185.2	57.9	-23.61
160	830	80	192.8	60.2	-18.62
200	830	100	241.0	60.2	-27.70
160	580	110	275.9	62.7	-18.75
120	330	130	363.6	69.9	3.81
80	330	80	242.4	75.8	12.78
96	297	100	323.2	80.8	15.10
65	200	100	325.0	81.3	27.35
96	350	80	274.3	85.7	21.93
60	160	100	375.0	93.8	38.59
96	250	100	384.0	96.0	20.95
96	297	80	323.2	101.0	21.37
96	200	100	480.0	120.0	32.58
60	120	100	500.0	125.0	54.38
72	120	120	600.0	125.0	47.57
60	80	120	750.0	156.3	66.79
65	80	120	812.5	169.3	69.95
60	80	80	750.0	234.4	70.76

Similarly, the medium VED case displays a minimal difference in predicted Ni content and M_s, 0.036 at% and 3.2 °C respectively, between the 600 °C preheat and room temperature condition. For the high VED scenario, a slightly larger difference in predicted Ni content across the preheat temperature range, 0.235 at%, is recorded. However, this corresponds to a difference in 0 °C for predicted M_s values, a result of extensive Ni evaporation leading to Ni content below 49.8 at%, the threshold for Ni-M_s insensitivity. It should be noted that the high VED is an extreme case utilizing a VED 65 J/mm^3 larger than the next largest VED in the experimental data set. If this study were repeated with $Ni_{51.2}Ti_{48.8}$ powder, high VED predicted Ni content would potentially not fall within the Ni-M_s insensitive region. However, increased insensitivity as Ni content approaches 49.8 at% would result in a minimal difference between predicted M_s across the preheat temperature range. Results for the low and medium VED cases could be expected to remain consistent across the composition and temperature ranges. Although preheat has a negligible effect in the current work, if powder compositions exceed 51.2 Ni at% and high VED design parameters are prominent, the significance of accounting for large preheat values during the fabrication process should be reevaluated.

An extensive global sensitivity analysis of model inputs was also conducted through the SAlib package [127]. Specifically, the approach utilized a Sobol analysis of 10 model inputs following a Saltelli sampling scheme with a total sample size of 22,528. Table 3.3 provides details on the model parameters and value ranges considered for each parameter. Figure 3.4 provides the results of the Sobol sensitivity analysis and sensitivities on model output variance corresponding to each input parameter. From these results, a total order insensitivity on model output can be established for model inputs such as layer thickness, L_t, the laser spot size, σ_x, density, ρ, and the start temperature, T_0, which is analog to a preheat temperature of approximately room temperature. Demonstrating more significant total order sensitivity are efficiency, η, thermal conductivity, κ, heat capacity, c_p, melt temperature, T_m, boil temperature, T_b, and Ni activity, α_{Ni}. Of these parameters, the melt and boil temperature ranges could actually be reduced, as uncertainty in these values is not that large. However, in the current evaluation the large sensitivity shown by these values, for the already relatively small ranges that were used, demonstrates their significance on model output, as melt temperature and boil temperature are inherently tied to melt pool geometry, evaporation loss, and chemistry change within a melt pool and across the entire component. The remaining parameters support initial measures taken to calibrate the model for efficieny, thermal conductivity, and heat capacity. Although Ni activity was not a calibrated parameter in the NiTi applied ICME framework, where results have already proven to be in agreement in light of this, Ni activity can be calibrated alongside other parameters as the framework is expanded and applied to additional material systems.

Table 3.3. Model parameters and thermophysical properties, and associated ranges, used for the sensitivity analysis study. Here, σ represents the laser spot size in terms of the 4σ diameter (the 4σ diameter range is (70 - 90) μm).

Symbol	Range	Unit	Description
L_t	26-46	μm	Layer Thickness
σ_x	17.5-22.5	μm	Sigma X
η	0.19-1.0	-	Efficiency
κ	7-50.8	$\frac{W}{m*K}$	Thermal Conductivity
c_p	302.8-1764.4	$\frac{J}{kg*K}$	Heat Capacity
ρ	6421-6521	$\frac{kg}{m^3}$	Density
T_m	1292-1332	$°C$	Melt Temperature
T_b	3087-3287	$°C$	Boil Temperature
T_0	15-25	$°C$	Start Temperature
α_{Ni}	0.15-0.4	-	Activity Ni

3.4.2 Surrogate Model

Although the framework is built off a fast acting thermal model, the nature of simulating thousands of track across multiple layers aggregates the total computational time required to simulate a component. This is especially true of design parameters consisting of small hatch space values, high laser power, and low laser velocity, where some cases can take on the upper end of 5 hours to simulate. Therefore directly applying an optimization technique could be computationally expensive and potentially become infeasible. For this reason, a surrogate model was developed through sklearn's support vector regression (SVR) package to remedy this [128]. A full factorial

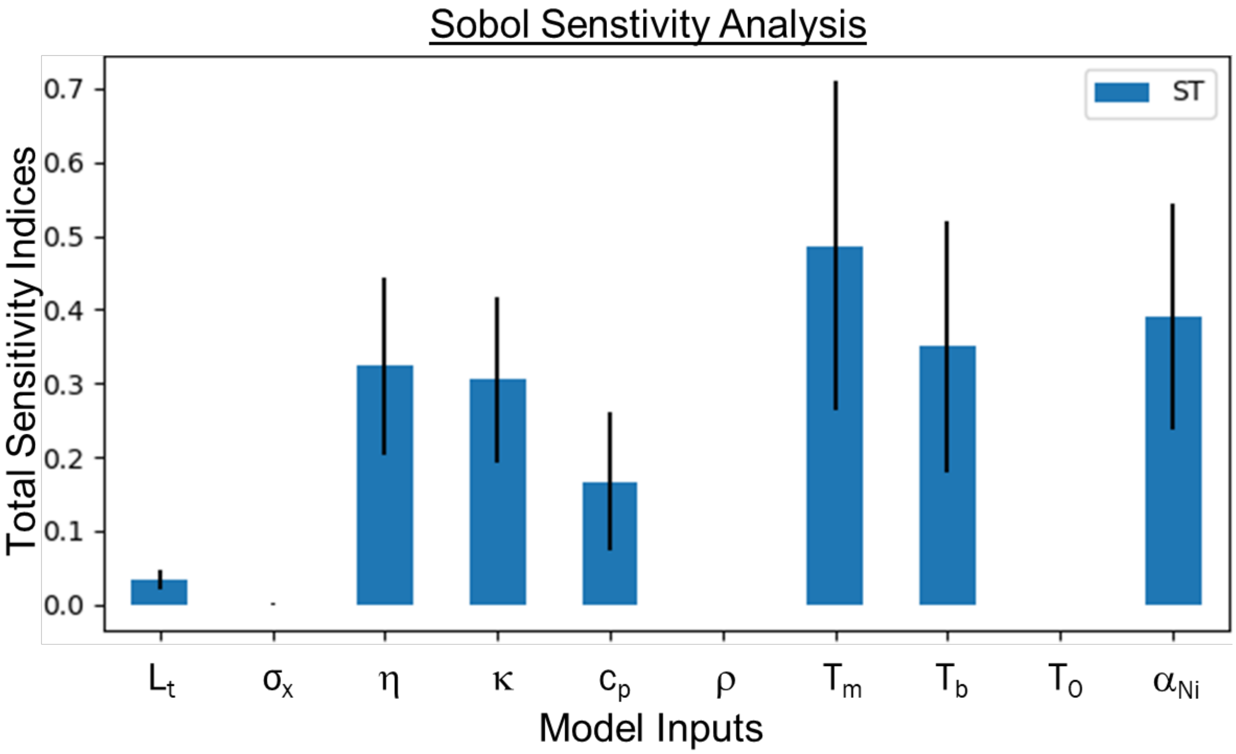

Fig. 3.4. Total order sensitivity for model parameters through the ICME framework for LPBF $Ni_{51.2}Ti_{28.8}$.

design approach, using $Ni_{51.2}Ti_{48.8}$, was taken to build the surrogate, with results summarized in Table 3.4. Although the upper bound of 3D printer's laser power can reach 260 W, the SVR will only be applied up to 150 W due to time constraints for running the full framework across the entire range of laser powers needed to train and test the surrogate. From the 210 simulated parameter combinations, the data was randomly split into training and testing groups of size 157 and 53, respectively. For validation with testing group, the SVR reported an R^2 of 0.91.

Table 3.4. $\mathrm{Ni}_{51.2}\mathrm{Ti}_{48.8}$ surrogate model parameters and test-train results.

Parameter	Value
Model	SVR
Chemistry	$\mathrm{Ni}_{51.2}\mathrm{Ti}_{48.8}$
Power	50-100 [W], by 25
Velocity	250-2200 [mm/s], by 25
Hatch	60-120 [μm], by 30
Test-Train	157
Validate	53
R^2 Test-Train CV	0.94
R^2 Validate	0.91

3.4.2.1 Sensitivity Analysis of Design Variables

Utilizing the surrogate model, the design variables of laser power, laser velocity and hatch spacing can be analyzed through an additional sensitivity analysis. A sensitivity analysis for model parameters such as heat capacity, thermal conductivity, efficiency, laser spot size, layer thickness, and preheat temperature is conducted in Section 3.4.1 and cannot be repeated with the surrogate model. This is due to the fixed state of these parameters when the surrogate model was constructed, their constant values now baked into the inherent calculations.

Realizing the benefit of the surrogate model and significantly reduced computational time, the SAlib package was utilized for a Sobol sensitivity analysis of the three design variables across their respective bounds. Table 3.5 and Table 3.6 contain the sensitivity analysis results when considering 8,000 and 80,000 parameter sets, respectively. The sensitivity index representing first order indices, second-order indices, and total-order indices are reported. Here the first-order indices measure the contribution to the output variance by a single model input alone, the second-order indices measure the contribution caused by the interaction of two model inputs, and the total-order indices measure the contribution caused by a model input from both its first-order effects and all higher-order interactions.

Table 3.5. Sensitivity analysis with 8,000 parameter sets.

Interaction	**Power**	**Velocity**	**Hatch**
First-Order	0.110	0.679	0.020
Total-Order	0.272	0.892	0.066
	Power-Velocity	**Power-Hatch**	**Velocity-Hatch**
Second-Order	0.153	-0.001	0.085

From Table 3.5, power and velocity exhibit first-order sensitivities, but hatch spacing has a minimal effect. Due to significantly higher total-order indices in power and velocity, there is likely higher-order interactions occurring. From the second-order interactions, there are strong interactions between power and velocity. Due to computing error, a negative value is observed for the power and hatch interaction. However, this error can be reduced with an increased sample size. In Table 3.6 similar interactions are observed, but the power-hatch interaction is now a positive value.

These results tend to match intuition from beforehand, however it is surprising that hatch spacing does not have larger sensitivity indices. It is possible that the range for hatch spacing used to construct the model is too small, relative to laser power and laser velocity, to contribute

Table 3.6. Sensitivity analysis with 80,000 parameter sets.

Interaction	**Power**	**Velocity**	**Hatch**
First-Order	0.106	0.689	0.012
Total-Order	0.264	0.875	0.062
	Power-Velocity	**Power-Hatch**	**Velocity-Hatch**
Second-Order	0.139	0.002	0.037

significant interactions. Similarly, a smaller parameter range could explain why the sensitivity indices for power are not as large as velocity. In the future, the design variable ranges used to build the surrogate model should be expanded and the sensitivity analysis repeated.

3.4.3 Constraints and Bounds

In the inverse design problem, the main design variables are laser power, laser velocity, and hatch spacing. Both laser power and scanning velocity should be within the operating range of the 3D printer. Therefore, the laser power can range from 50 W to 150 W while the scanning speed ranges from 250 to 2200 mm/s. On the other hand, the hatch spacing is chosen based on a calibrated thermal model for $Ni_{51.2}Ti_{48.8}$ which determines the melt pool dimensions used to calculate the range of hatch spacing in the good printability region. From this calibrated model, the hatch spacing should be kept between 60 and 120 μm. Table 3.7 presents these bounds. At the current stage of the problem formulation, there are no constraints considered. A constraint which could be considered in the future could be constructed using a printability map. This map details the defect, such as balling, keyhole, and lack of fusion, and good print regions in design space, and could be used to further restrict the bounds of the design space to a region where design solutions would provide defect-free prints.

Table 3.7. Design variables and corresponding bounds.

Parameter	Lower Bound	Upper Bound
Power [W]	50	150
Velocity [mm/s]	250	2200
Hatch [μm]	60	120

3.4.4 Exploration of the Design Space

As an initial analysis of the design space, Nickel content and M$_s$ were calculated for various points of interest through the surrogate model. This exploration is documented in Table 3.8. From the parameter sets explored, it can be seen that a wide range of M$_s$ values can be achieved within the bounds of the design space. This provides a strong foundation for the surrogate model to provide an inverse design solution for a variety of specifications. Additionally, this can be achieved efficiently due to the fast acting nature of the surrogate model, which makes it possible to determine the M$_s$ for thousands of points in the design space in a matter of seconds.

Table 3.8. Interesting parameter sets for the design variables (power, velocity, and hatch spacing) and corresponding predictions for Ni content and M_s.

	Input			Output	
Set #	**Power [W]**	**Velocity [mm/s]**	**Hatch [μm]**	**Ni [at%]**	**M$_s$ [K]**
1	60	250	60	51.08	235.71
2	60	250	120	51.11	230.10
3	100	250	60	50.63	286.31
4	100	250	90	50.87	262.44
5	100	500	90	51.14	225.31
6	140	250	60	50.24	319.53
7	140	250	120	50.76	274.19
8	140	500	90	51.02	244.62
9	140	500	120	51.06	238.23
10	140	750	90	51.13	227.07
11	140	750	120	51.14	225.17

3.4.4.1 Process Maps

As an extended exploration of the design space and as a tool for accelerated materials design and development, process maps were developed as look-up tables and to guide experiments by providing insight on PSPP trends of LPBF AM Ni$_{51.2}$Ti$_{48.8}$. Figure 3.5 illustrates these process maps and PSPP for a range of laser power and laser velocity combinations across the hatch space values of 60 μm, 90 μm, and 120 μm, where ΔNi represents the difference in predicted Ni content, Ni$_{Predicted}$, from the initial Ni content, Ni$_{Initial}$, for a given set of design variables:

$$\Delta Ni = Ni_{Initial} - Ni_{Predicted} \tag{3.2}$$

Consistent with expectations, it is found that across all hatch space values there is an increase in

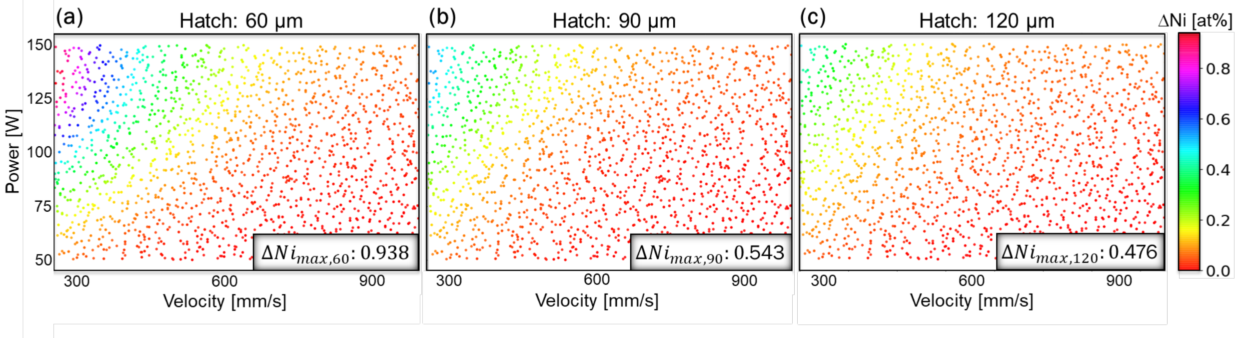

Fig. 3.5. Process maps for NiTi depicting change in Ni content from the starting composition as a result of the LPBF AM process across a range of laser power and laser velocity combinations for several hatch space values: (a) 60 μm; (b) 90 μm; (c) 120 μm.

ΔNi with increasing laser power and decreasing laser velocity. Additionally, as power and velocity combinations approach lower linear energy densities, ΔNi approaches zero. This aligns with the lower temperatures and negligible evaporation that would be expected at lower energy inputs. As hatch space decreases it is also shown that there is an increase in ΔNi for corresponding power and velocity combinations. This results in much more significant evaporation for the hatch 60 μm parameter sets compared to the 120 μm parameter sets. This is demonstrated through the maximum difference in predicted and initial Ni content, ΔNi$_{max}$, for the 60 μm hatch spacing, 0.938 at%, being nearly double the ΔNi$_{max}$ experienced at 120 μm hatch spacing, 0.476 at%, for the same laser power and velocity combination. Further, these predicted Ni content values can be correlated to M$_s$ through the semi-analytical Ni-M$_s$ relation described by Equation 3.1. By leveraging these process maps and PSPP insights, the ΔNi content associated with each design parameter combination and the ΔNi content required for a target M$_s$ could be used to determine the appropriate combination of design parameters required to achieve the desired design specifications.

3.5 Multi-Objective Problem

The main objective of this inverse design optimization problem is to find the power, velocity, and hatch spacing design parameter combination that most closely achieves the desired M_s. This is achieved by minimizing the residual between the target M$_s$ and the surrogate-predicted M$_s$.

However, if the optimizer gets stuck in a local minimum, then it is possible that a solution for the desired M$_s$ may not be attained. For this reason, a multi-start approach should also be considered for the optimization process. The equation for this main objective is provided in Equation 3.3.

$$\epsilon_1 = min(|M_{s,Target} - M_{s,Predicted}|) \tag{3.3}$$

The second objective of this optimization problem is to find the velocity and hatch combination that minimizes fabrication time. This is formulated as the minimization of the residual between the product of the selected velocity and hatch combination and the maximum velocity and hatch values allowed within the bounds of the design space. The equation for this objective is provided in Equation 3.4.

$$\epsilon_2 = min(|v_{max} * h_{max} - v * h|) \tag{3.4}$$

Combining these objective functions into a single minimization problem, a design solution that minimizes the error across both objectives may be found. It should be noted that the design solution for the combined multi-objective function might not yield the same optimal design solution as when considering each objective function individually. The equation for this combined multi-objective problem is provided in Equation 3.5.

$$\epsilon = min(|(M_{s,Target} - M_{s,Pred})| + (v_{max} * h_{max} - v * h)) \tag{3.5}$$

Within the multi-objective problem, the bounds considered are the same as were considered in the single-objective optimization problem, restricting the values of power, velocity, and hatch spacing as dictated by the capabilities of the 3D printer and the capability of the surrogate model. There were no additional constraints to be included in the problem formulation.

When looking to minimize ϵ_1, this may not necessarily come at the detriment of ϵ_2. There may be many solutions to the optimization problem, but this may also depend on the target M$_s$. Another way to approach the issue is that increasing velocity and hatch spacing reduce the amount of evaporation that may occur, as demonstrated by the process maps in Figure 3.5. This has to be offset by a corresponding increase in power, if the target M$_s$ is large. Due to the nature of this relationship, there is a possibility that if the maximum velocity and hatch spacing are utilized, the 3D printer may not be able to output sufficient laser power to cause enough evaporation to reach a desired M_s. In this case, the objectives would be mutually opposing. The larger velocity and hatch desired, the larger power required to reach a target M$_s$. When solving for the design variables, one approach is that the optimizer should seek to maximize power and then reduce or increase velocity and hatch until a feasible solution is achieved. This is because using the maximum power mitigates the reduction in evaporation loss caused by an increase in velocity and hatch spacing. It should be noted that satisfying the minimization for M$_s$ is a higher priority than the increased build time. If the part can be built quickly, but not at the correct specs, then it is not a successful build. As part of the determination for whether or not a build is successful, defect-free, an evaluation of a printability map would provide insight on design parameter combinations which are likely to result in keyhole, balling, and lack of fusion defects. The constraints and bounds set by the printability map for good quality prints are currently not considered, leaving the potential for optimized solutions to result in defective prints, and should be incorporated into the optimization scheme in the future.

3.6 Algorithm Selection

The optimization of the current problem formulation was conducted through an easily accessible repository of optimization methods through the ’scipy.optimize’ package [128]. Both gradient and heuristic approaches have been explored.

3.6.1 Gradient Based Approach

Both the Nelder-Mead and BFGS methods were utilized through python’s ’scipy.optimize.minimize’ function, however these approaches do not accept bounds as an input. When testing several example parameter sets for a target M$_s$, this resulted in optimized parameter sets containing negative velocity and hatch values. This is not an acceptable solution, so the sequential least squares quadratic programming (SLSQP) method was utilized due to having bounds as an input argument. In the case of the single objective function minimizing the error in a target and predicted M_s, the SLSQP method was applied for a target M_s of 250 K and 290 K. The results are listed in Table 3.9.

It is shown that SLSQP converged for all cases, with multiple appropriate solutions for each target objective, however it was also found that the SLSQP could get stuck in local minimum. Addressing the issue of local minimum and the potential for multiple solutions in the design space that could satisfy the optimization problem, a multi-start approach should be utilized to better ensure that the optimal solution is found. Although there are multiple solutions, it is still possible that one solution is preferred over another. Not considered in this single objective function is production time, where a larger velocity and hatch spacing equate to improved fabrication rate. For this reason, from the first target's two solutions, set 2 might be preferred over set 4 due to the higher scanning velocity. From the second target's three parameter sets, all solutions (set 6, 7, and 9) are fairly close in value for power, velocity, and hatch. However set 9 might edge out as the choice design set with a slightly larger velocity and hatch spacing combination compared to the other solutions.

3.6.2 Heuristic Optimization

For the heuristic optimization approach, a genetic algorithm, in particular the differential evolution method from the 'scipy.optimize' package, was utilized. This function is able to find the global minimum of a multivariate function, accepts bounds, can search large areas of space, and

Table 3.9. SLSQP Method for single objective optimization with target M_s, the initial guess, and the optimized solution.

		Initial Guess					Optimized Solution				
Set #	**Target M_s [K]**	**Power [W]**	**Velocity [mm/s]**	**Hatch [μm]**	**Ni [at%]**	**M_s [K]**	**Power [W]**	**Velocity [mm/s]**	**Hatch [μm]**	**Ni [at%]**	**M_s [K]**
1	250	135	1900	60	51.20	212.7	121.72	1892.17	60.00	51.20	212.82
2	250	150	1900	60	51.19	213.5	150.00	593.84	60.03	50.98	250.00
3	250	150	1900	120	51.20	211.8	150.00	1102.98	120.00	51.11	230.04
4	250	150	250	120	50.72	278.2	98.20	277.86	98.27	50.98	250.00
5	290	150	400	120	50.95	253.3	150.00	250.00	120.00	50.72	278.20
6	290	150	400	60	50.69	280.4	150.00	353.6	60.04	50.59	290.00
7	290	130	800	75	51.15	223.3	140.97	349.01	64.13	50.59	290.00
8	290	140	800	110	51.15	222.1	140.00	1109.03	120.00	50.11	230.05
9	290	140	700	110	51.14	223.7	144.55	357.65	60.77	50.59	290.00

the reduced computational cost of the surrogate model will allow a quick assessment of the local min/max across large areas of the design space. This function is also packaged in a similar manner to the previously utilized gradient based SLSQP approach, allowing for easy implementation.

Additionally, the differential evolution method does not accept an initial guess for the design space. For a target M_s of 250 K, a population multiplier of 1, and seeding for traceable results across 10 tests. Figure 3.6 illustrates the convergence of each test, while the corresponding feasible optimal solutions are listed in Table 3.10.

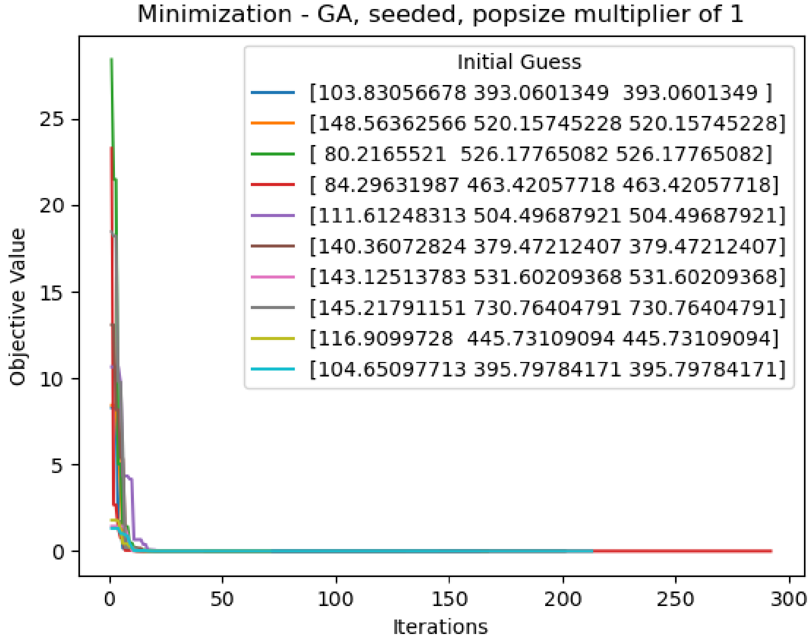

Fig. 3.6. Convergence for single objective differential evolution algorithm with popsize multiplier of 1 for a range of seeds.

It is shown that the differential evolution algorithm reached the absolute minimum objective value in every case, providing multiple unique design solutions, while the SLSQP got stuck in a local minimum for 2 of the 4 cases and yielded 2 unique solutions. It is apparent that there many solutions to the target M_s of 250 K. The genetic algorithm also had a slightly increased computational cost

Table 3.10. Differential evolution and sequential least squares quadratic programming feasible optimal solutions.

		Optimized Solution				
Set #	**Target M_s [K]**	**Power [W]**	**Velocity [mm/s]**	**Hatch [μm]**	**Ni [at%]**	**M_s [K]**
Differential Evolution						
1	250	101.29	328.03	89.08	50.98	250
2	250	106.10	395.26	77.87	50.98	250
3	250	107.14	278.28	113.30	50.98	250
4	250	109.05	376.23	85.66	50.98	250
5	250	114.64	470.35	67.91	50.98	250
6	250	127.97	538.58	62.82	50.98	250
7	250	135.88	443.92	91.14	50.98	250
8	250	138.42	459.00	89.12	50.98	250
9	250	140.76	519.79	76.74	50.98	250
10	250	145.56	439.45	94.52	50.98	250
Sequential Least Squares Quadratic Programming						
1	250	98.20	277.86	98.27	50.98	250.00
2	250	121.72	1892.17	60.00	51.20	212.82
3	250	150.00	593.84	60.03	50.98	250.00
4	250	150.00	1102.98	120.00	51.11	230.04

relative to the SLSQP.

3.6.2.1 Parameter Tuning

In general, the chances of finding the global minimum will improve through a higher popsize value, higher mutation and dithering, but lower recombination values. Figure 3.7 illustrates the results from popsize multiplier of 10. The same seeded values were used here as well as the previous convergence calculations. The results are similar to a popsize multiplier of 1, but took significantly more computational time. This is not worth the cost, and it seems the model performs efficiently and with good success in its current state. The number of iterations before the objective function was satisfied also increased for several of the runs, however this could be remedied by utilizing a max iteration parameter.

Utilizing the absolute tolerance parameter can also help with this issue. By cutting down on these additional iterations, where minimal change in the objective value is seen, computational cost

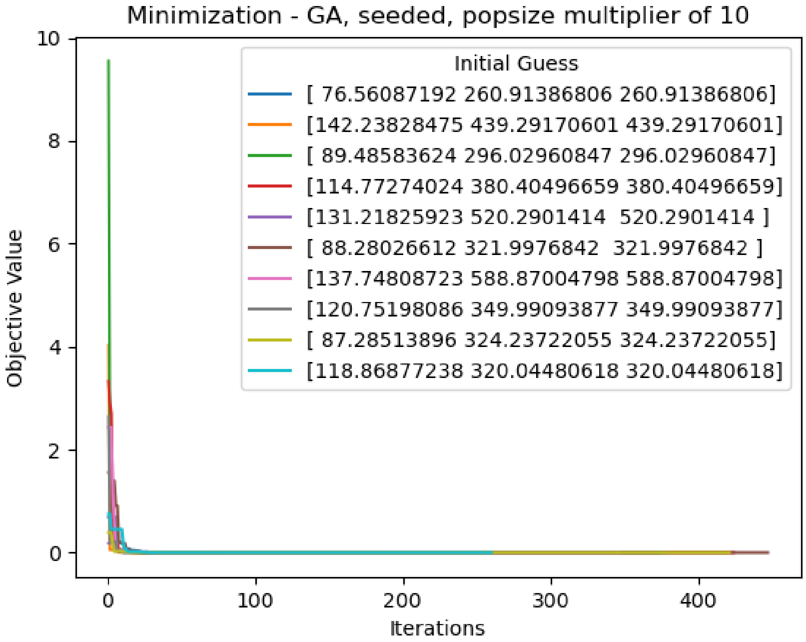

Fig. 3.7. Convergence for single objective differential evolution algorithm with popsize multiplier of 10 for a range of seeds.

can be reduced. Increasing the mutation parameter can also help prevent the optimizer from getting stuck in a local minimum. Additionally, the ‘polish’ parameter can be used to improve minimization slightly by utilizing the ’L-BFGS-B’ or ’trust-constr’ method on the best population member. This could have a similar impact to re-running the feasible optimal solution from the genetic algorithm through a gradient based approach in an effort to improve the minimization. When considering a second objective function, adjusting the popsize multiplier, increasing the mutation, and polishing the results aid in finding the feasible optimal design solution.

It is likely that a global optimum has been found, and multiple of them, however it is important to recognize that the genetic algorithm does not guarantee the global optimum. Results should be run through a gradient based approach for further minimization. It should also be noted that there are many solutions to the objective function, and it might be impossible to find them all, especially when considering continuous design variables. If constraints are added to the problem formulation, this might reduce the number of global optimal solutions that satisfy the objective function.

3.7 Scaling

Scaling takes into account that the design variables and objective values may be different magnitudes. This may cause the optimizer to more heavily favor one design variable or objective, and may hinder the performance of the optimizer. The effect of scaling on the single objective optimization of minimizing the error between the target and predicted M$_s$, Equation 3.3, is explored. This will also be analyzed in the combined multi-objective optimization, which considers the objective of minimize the production time, Equation 3.4. This means the combined multi-objective optimization function is required, Equation 3.5. The design solution of parameter set 4 from Table 3.9 is used for this scaling exercise.

By utilizing the 'numdifftools' package in python, the Hessian matrix of the single objective optimization for a target M$_s$ is determined with the 'Hessian' function call (Method 1):

$$H = \begin{bmatrix} -1.601e-03 & 1.424e-04 & 3.797e-03 \\ 1.424e-04 & -5.053e-06 & 2.634e-05 \\ 3.797e-03 & 2.634e-05 & -9.068e-03 \end{bmatrix} \tag{3.6}$$

Also utilizing the 'numdifftools' package, the diagonal entries of the Hessian are determined with the 'Hessdiag' function call (Method 2):

$$H = \begin{bmatrix} -7.754e-04 & -2.610e-06 & -4.399e-03 \end{bmatrix} \tag{3.7}$$

It is unclear why the 'Hessdiag' output does not much the diagonal from the 'Hessian' output. However both scale factors will be considered, as well as others, in order to improve the optimal design solution.

From Method 1 we have:

$$H_{11} = -1.601e - 03 \rightarrow 10^{-3}(-1.601)$$

$$H_{22} = -5.053e - 06 \rightarrow 10^{-6}(-5.053)$$

$$H_{33} = -9.068e - 03 \rightarrow 10^{-3}(-9.068)$$

From Method 2 we have:

$$H_{11} = -7.754e - 04 \rightarrow 10^{-4}(-7.754)$$

$$H_{22} = -2.609e - 06 \rightarrow 10^{-6}(-2.609)$$

$$H_{33} = -4.399e - 03 \rightarrow 10^{-3}(-4.399)$$

The scaling of the design variables took the form presented in Equation 3.8 with the bounds in Equation 3.9.

$$x = [\frac{y_1}{Scalar_{H_{11}}} \frac{y_2}{Scalar_{H_{22}}} \frac{y_3}{Scalar_{H_{33}}}] \tag{3.8}$$

$$\begin{aligned} Scalar_{H11} * 50 \le Power \le Scalar_{H11} * 150 \\ Scalar_{H22} * 250 \le Velocity \le Scalar_{H22} * 2200 \\ Scalar_{H33} * 60 \le Hatch \le Scalar_{H33} * 120 \end{aligned} \tag{3.9}$$

The scaled design variables, originally the optimal feasible solution, had to be reverted before input into the surrogate in order to have accurate M$_s$ predictions. New design variables within the scaled bounds are chosen for the next iteration and the process repeated until the objective function is satisfied. Each set of scalar values yielded negligible improvements, on the scale of 10^{-5} or smaller, for the optimal solution. The design variables experienced minimal change in each case.

The updated Hessian for one of these solutions is shown in Equation 3.10.

$$H = \begin{bmatrix} -0.0085 & -0.0047 & 0.0406 \\ -0.0047 & -0.0003 & 0.0040 \\ 0.0406 & 0.0040 & -0.0162 \end{bmatrix} \tag{3.10}$$

When considering the combined multi-objective function, a target M_s of 250 K was maintained. Since there are several acceptable design solutions already known in Table 3.9, a comparison between design solutions for the single-objective and multi-objective formulations can be readily made. In the case of the multi-objective function, the objective values for each case must be scaled accordingly. For Equation 3.3 the error, ϵ_1, approaches 0 as the objective is optimized. For Equation 3.4, ϵ_2 also approaches 0, however relative to ϵ_1 the objective value can be of a much larger magnitude. For this reason, the second objective function has been scaled in Equation 3.11:

$$\epsilon_{2s} = min(\frac{v_{max} * h_{max} - v * h}{10000}) \tag{3.11}$$

Equation 3.12 combines this scaled objective function with Equation 3.3:

$$\epsilon_{3s} = min(|(M_{s,Target} - M_{s,Pred})| + \frac{v_{max} * h_{max} - v * h}{10000}) \tag{3.12}$$

This newly scaled multi-objective function was then tested, with a target M_s of 250 K, and results compiled in Table 3.11.

For the SLSQP sets, each of the optimal feasible design solutions reached the target M$_s$ of 250 K. However, there was some variation in the reported power, velocity, and hatch spacing values for each set. Amongst the solutions, set 3 yielded the largest product of velocity and hatch spacing, thus the shortest production time. The design variables of set 3 were similar to set 2, however set 3 was the only case were the resulting M$_s$ had a small variation, 0.06 K, from the target M_s, which may have contributed to the small improvement in production time.

For the differential evolution sets, parameter tuning across 7 sets was conducted and objective values were measured. It was shown that by increasing the popsize multiplier from 1 to 200 the

Table 3.11. Multi-objective optimization with target M_s, the initial guess, and the optimized solution.

Model Input					Optimized Solution				
Sequential Least Squares Quadratic Programming									
Set #	**Power [W]**	**Velocity [mm/s]**	**Hatch [μm]**	**Target M$_s$ [K]**	**Power [W]**	**Velocity [mm/s]**	**Hatch [μm]**	**M$_s$ [K]**	**V*H [mm^2/s]**
1	100	350	70	250	111.68	449.77	70.01	250.00	31488.40
2	150	250	120	250	150.00	409.86	114.66	250.00	46994.55
3	150	350	120	250	150.00	419.61	118.90	250.06	49891.63
4	50	800	60	250	150.00	576.79	63.93	250.00	36874.18
Differential Evolution									
Set #	**Popsize**	**Mutation**	**Polish**	**Target M$_s$ [W]**	**Power [W]**	**Velocity [mm/s]**	**Hatch [μm]**	**M$_s$ [K]**	**V*H [mm^2/s]**
1	1	0.2	True	250	113.09	462.58	68.19	250.00	31543.33
2	10	0.2	True	250	98.19	386.91	69.20	250.00	26774.17
3	100	0.2	True	250	149.70	436.00	95.96	250.00	41838.56
4	200	0.2	True	250	150.00	423.61	120.00	250.00	50833.20
5	200	0.1	True	250	150.00	423.61	120.00	250.00	50833.20
6	200	0.5	True	250	150.00	423.57	120.00	250.00	50828.40
7	200	0.2	False	250	150.00	423.61	120.00	250.00	50833.20

optimal feasible design solution improved. A mututation of 0.1 and 0.2 had similar results, however a value of 0.5 yielded a slight, negligible, reduction in production time. A test of the polish parameter was also conducted, and resulted in no difference when set to 'False' on the best performing model parameters. This resulted in a popsize of 200, mutation of 0.2, and a polish value of 'True,' for applying a gradient based approach on the best population member, as the tuned parameters for the differential evolution approach. Additionally, the best solutions from the differential evolution approach were used as an initial guess in the SLSQP, but no difference in the design variables was reported. These results can also be compared with the single-objective design solutions from Table 3.9, where it is shown that feasible solutions for the target M$_s$ of 250K are achieved in both cases, however the multi-objective optimal solutions also provide faster fabrication rates than the solutions that were not concurrently optimized for production time.

Further investigating the second objective function, from Equation 3.4, ϵ_2 is defined as a function of laser velocity and hatch spacing, and from the sensitivity analysis conducted in Section 3.4.2.1, it is shown that hatch spacing has the smallest effect on predicted M$_s$. With this knowledge about the design variables, it can be expected that, in the current formulation of the second objective function, the optimal feasible solution will report a hatch spacing at the upper bound of the design space, as reported in the best solutions of Table 3.11. Increasing hatch spacing has a small effect on M$_s$ relative to velocity, but has a large effect on ϵ_2. For this reason, it might be beneficial to revisit the formulation for gauging production time, so that laser velocity plays a larger role.

3.8 Final Design

Having conducted the sensitivity analysis, scaling, applying the SLSQP with a multi-start approach, and applying the differential evolution with tuned parameters, the chosen solution for the multi-objective problem with a target M_s of 250 K is as follows:

$$\begin{bmatrix} x_1 \\ x_2 \\ x_3 \end{bmatrix} = \begin{bmatrix} 150.0\,W \\ 423.61\,mm/s \\ 120.0\,\mu m \end{bmatrix}$$

Additional solutions to this design problem have already been referenced in 3.11.

3.9 Post Optimality Analysis

Section 3.4.2.1 and 3.7 have already discussed much of the detail on the surrogate sensitivity analysis and scaling as applied to the single and multi-objective optimization problem. Additionally, solutions have been determined for over 80,000 points in the parameter space. Figure 3.8 illustrates the magnitude of 8,000 of these points in the design space.

From visual inspection, concave surfaces can be approximated by the bounds formed by colors representing the magnitude of M$_s$ values. By analyzing the M$_s$ values alongside the product of velocity and hatch spacing, one could easily filter the design space to potentially optimal solutions. These solutions could be used in a multi-start approach as initial guesses in the SLSQP to further optimize the design variables. Due to the speed of the surrogate model, this methodology should yield quick results with strong confidence that one of the design variables is the global minimum.

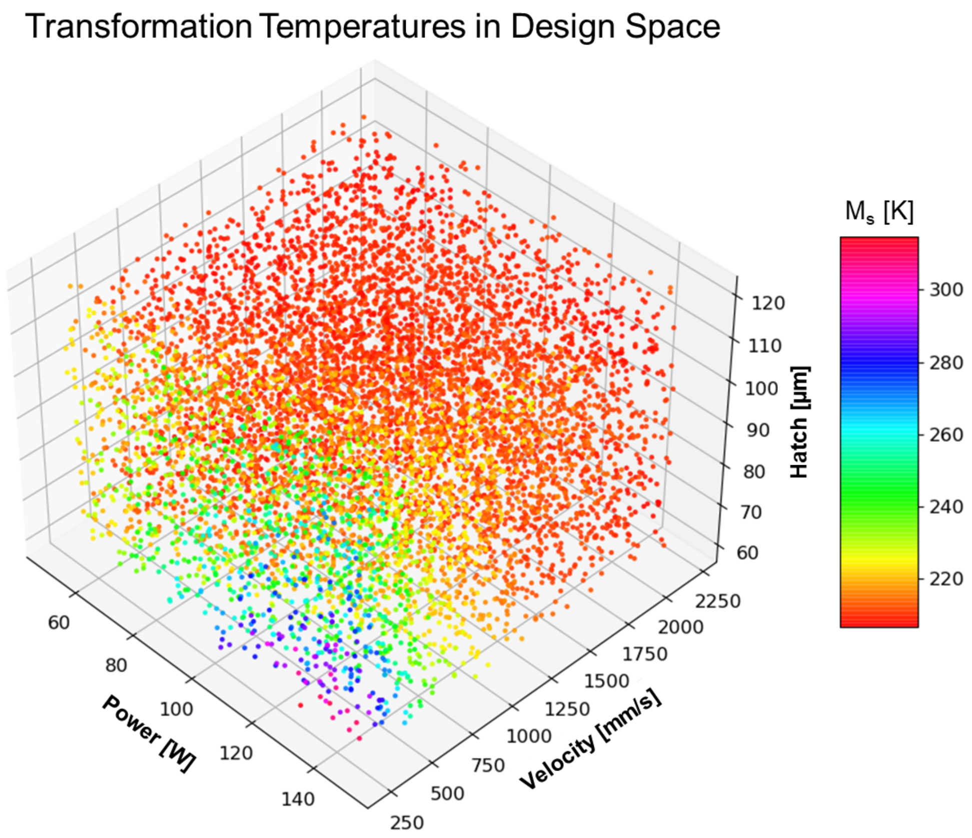

Fig. 3.8. M_s values for 8,000 points in the design space.

Additionally, a Pareto front was generated, Figure 3.9, for the multi-objective optimization problem. It is shown that the SLSQP algorithm is able to produce multiple solutions to the problem, including several that are stuck in a local minimum. Although, at close inspection, only two solutions truly compose the Pareto front, the objective values, based on error criteria, are significantly small and imply that there are multiple acceptable solutions to the multi-objective optimization problem. Additional criteria, such as printability, can be used to further optimize the process parameters for desired material properties in AM LPBF $Ni_{51.2}Ti_{48.8}$ SMAs.

3.10 Conclusions

The inverse design problem for AM LPBF $Ni_{51.2}Ti_{48.8}$ SMAs was approached through the application of single and multi-objective optimization technique, analyzed, and an optimal feasible solution was found. Multiple solutions were found for all cases, through both the gradient based

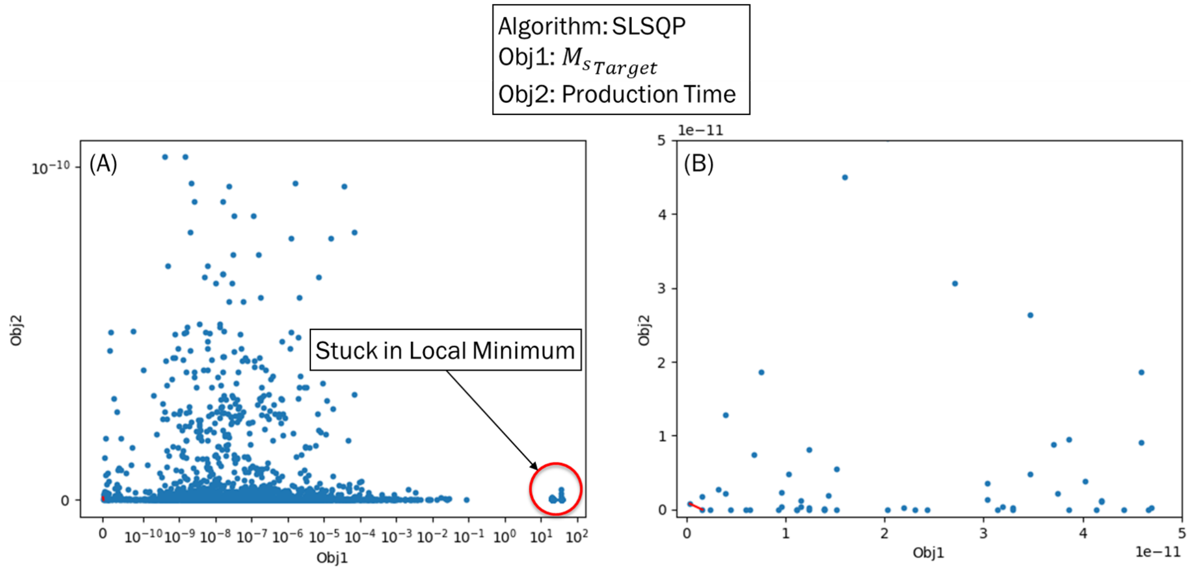

Fig. 3.9. Pareto front for multi-objective optimization of M_s and production time. (A) The SLSQP algorithm provides multiple optimal solutions and several local minimum solutions. (B) Zoomed for enhanced visibility of the Pareto front.

SLSQP and heuristic differential evolution approach. Additionally, tuning the parameters of the differential evolution function improved the results of the optimal solution. Scaling the objective values in the multi-objective problem was also an important consideration that improved the reported solution. With the consistency of results and development of a surrogate model, allowing complete analysis of the design space, there is a high level of confidence that the reported optimal design variables are indeed the global minimum. The conducted sensitivity analyses and constructed process maps also provided insight and supported expectations for overall PSPP trends across the design space.

Future considerations should take into account constraints that might be applied to the problem formulation, such as printability maps dictating design space regions correlating to good quality defect-free prints, and regions where keyhole, balling, and lack of fusion defects could be expected. Additionally, an improved formulation of the second objective function could more accurately capture the sensitivity and importance of velocity and hatch spacing in calculating M_s.

4. UNCERTAINTY QUANTIFICATION AND PROPAGATION ACROSS A MULTI-MODEL COMPUTATIONAL FRAMEWORK FOR THE TAILORED DESIGN OF ADDITIVELY MANUFACTURED SHAPE MEMORY ALLOYS

4.1 Overview

Integrated computational materials engineering (ICME) combines the utility and efficiency of simulations with experimentation to drive forward materials design and discovery. These physics-based and data-driven frameworks have enabled material advancement by querying the complex process-structure-property-performance relationships to inform and guide experiments for the cost-effective design of alloy systems. In this study, a proven computational framework is presented and applied towards the tailored design of additively manufactured (AM) high-temperature NiTiHf shape-memory alloy (SMA) parts. Specifically, the effort deploys a design tool to attain specific transformation temperatures by composition control through differential evaporation, which in turn depends on processing conditions. This framework consists of a fast-acting discrete source model to simulate thermal history, a multi-layer model to account for chemistry propagation across melt pools, and a differential evaporation model to evaluate Nickel loss throughout the fabrication process. Besides the development of this multi-model chain, proper quantification of model uncertainties is critical to an ICME approach for materials design. Addressing these concerns, the parameter calibration and uncertainty quantification (UQ) of hierarchical model components is conducted through a Markov chain Monte Carlo (MCMC) Bayesian approach over either the model itself or a representative Gaussian process-based surrogate model. These uncertainties are propagated across the models to the final response, i.e., martensitic start temperature. Subsequently, the hierarchical model framework is validated by comparing the experimental results with the most plausible values and uncertainty bounds obtained for the multi-model predictions at different processing conditions. From this calibrated and validated framework, process maps to streamline and illustrate the tailored design of AM high-temperature NiTiHf SMAs are developed, which demonstrates a promising path towards efficient design under uncertainty in additive manufacturing processes.

4.2 Introduction

Beyond the original and well-proven capabilities of Additive Manufacturing (AM) processes, such as geometric freedom and mass customization, a fast emerging avenue of development involves AM of functional materials such as NiTi-based alloys, with variations of the ternary component including Pt, Pd, Au, Zr, and Hf [129, 130]. These shape memory alloys (SMAs) exhibit a functional response based on temperature, where the ternary alloying element affects material properties such as hardness, superelasticity, and transformation temperature. NiTi, prominently known for its biocompatibility, and functional and mechanical properties, exhibits a martensitic start transformation temperature, M_s, spanning 100 °C for a composition range of (50 - 51) Ni at% [70]. However, NiTi SMA is limited in its use for high-temperature (HT) applications due to a low ceiling for M_s, approximately 70 °C. For this purpose, tertiary SMA NiTiHf enables the cost-effective application of functional materials in high-temperature environments, exhibiting transformation temperatures dependent on both Ni and Hf content and an M_s ceiling exceeding 500 °C [131, 132]. Umale et al. [133] demonstrate this NiTiHf chemistry-property relationship by varying Ni and Hf content between (49.8 – 51.3) at% and (0 – 30) at% respectively, resulting in an M_s range of nearly 700 °C, from -163 to 519 °C.

Of crucial importance for the tailored design of AM-fabricated NiTiHf HT-SMA across this window of transformation temperatures is the knowledge of underlying physics and mechanisms to control process-structure-property-performance (PSPP) relationships. During the laser powder bed fusion AM (LPBF), a material undergoes multiple bouts of rapid solidification and cooling. The magnitude and duration of these events at a specific location depend on a combination of process parameters, including laser power, laser velocity, hatch spacing, etc. These parameters directly relate to melt pool geometry and the loss of alloying elements due to differential evaporation, resulting in location-specific chemistry throughout an AM part [14, 134]. For NiTi alloys, a significant difference in volatility between alloying elements is conducive to significant changes in composition and properties through Ni loss and a sensitive Ni-M_s correlation [70]. Additively manufactured NiTiHf SMA shares this difference in volatility between alloying elements, allowing for quantifiable chemistry change due to differential evaporation [133, 134]. Informed modulation of AM process parameters then enables controlled modification of melt pool structure and chemistry change due to evaporation, corresponding to tailored changes in properties and fit-for-purpose components. However, this is not easily achieved and requires effective leveraging of simulations and experiments along the PSPP chain of integrated computational materials engineering (ICME) shown in Figure 4.1.

Generally, the development of models and simulations is a vital task in the ICME framework to direct experiments in materials and product design along the PSPP chain. However, design is not viable without the calibration and uncertainty quantification (UQ) of these computational tools. These needs arise from our lack of knowledge about the physical systems, applied assumptions and simplifications, and incomplete parameterization [101]. In other words, UQ is necessary in order to provide a notion of confidence in computational-guided design. This necessity is especially prominent in AM process design due to the many complex physical phenomena and hard-to-measure variables involved, which correspond to multiple assumptions, missing physics, and lack of parameter knowledge in the relevant models and simulations. In the recent decade, Markov Chain Monte Carlo (MCMC) approaches in the context of the Bayesian inference have been commonly used to perform model calibration and UQ in different materials science and engineering problems [14, 102–108, 135–140]. The popularity of these UQ approaches is driven by their simple implementation, powerful and rigorous analysis, consideration of prior knowledge, and capability of updating analysis results upon acquiring new data [101]. However, the high computational cost of these methods restricts their application in the UQ of expensive models and simulations. In these cases, a surrogate-based MCMC technique, such as Kennedy and O'Hagan's GP-based approach [141] can be applied to quantify uncertainties [142, 143].

In the current work, a fast-acting ICME framework [14], consisting of a thermal model, multi-layer model, and differential evaporation model, is developed to achieve designable and controllable location-specific actuation in additively manufactured NiTiHf SMA components. For the purpose

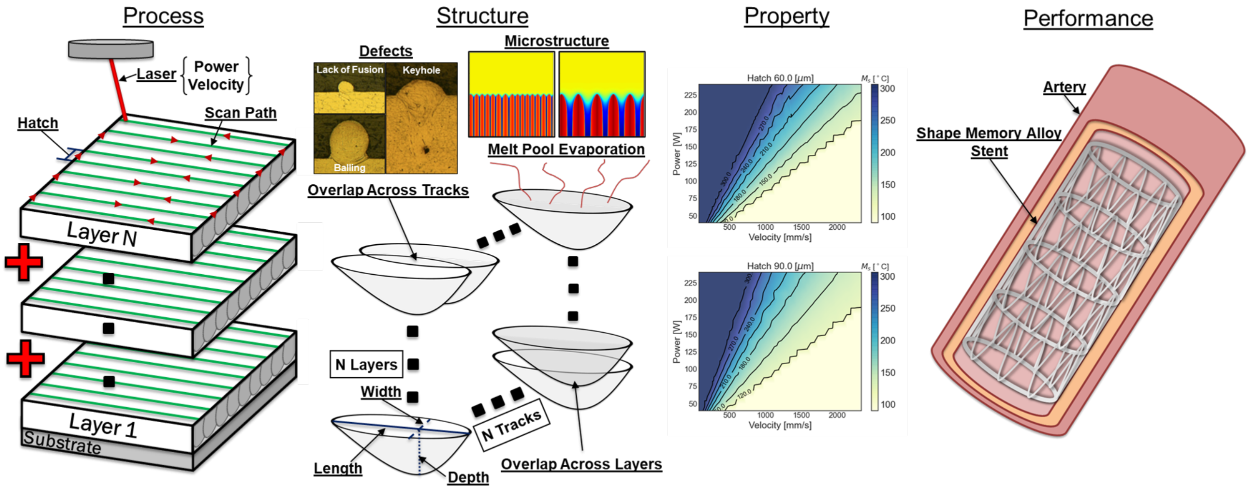

Fig. 4.1. Sample schematic of an integrated computational materials engineering modeling approach for LPBF AM. This is established through a process-structure-property-performance relationship.

of accelerated materials design and discovery, the capabilities and speed alotted by this fast-acting framework serve as a swift tool ideal for screening PSPP trends. This is in contrast to high-fidelity models, e.g., finite element models, that require a high computational cost not suitable for expedited material development in the large and complex design space provided by AM. Additionally, the difficulties and costs associated with the calibration of high-fidelity models further hinder their application in the ICME materials design. However, to fill the accuracy gap resulting from the reduction of considered physics in low-fidelity models, probabilistic calibration approaches are applied over the fast-acting low-fidelity models in this framework to identify the uncertainty bounds of the final model outcomes, i.e., location-specific properties of additively manufactured parts, sufficient to provide a notion of robustness in materials design.

In this regard, the calibration process and uncertainty quantification are performed using a Markov chain Monte Carlo (MCMC) Bayesian approach directly over the thermal model component and indirectly over the differential evaporation model through a representative Gaussian process-based surrogate model. Following this, quantified uncertainties are propagated across the modeling framework to the final model response, martensitic start temperature. Subsequently, the hierarchical model framework is validated through comparing the experimental results with the most plausible values and uncertainty bounds obtained for the multi-model predictions at different processing conditions. Exploiting this calibrated and validated computational framework, process maps are developed for the sake of tailored design of additively manufactured high-temperature NiTiHf SMAs, providing a promising path towards efficient design under uncertainty in AM processes.

4.3 Material Response during the Thermal Process

4.3.1 Thermal Model

A discrete source model (DSM) proposed by Schwalbach et al. [94] is applied in this work to predict the thermal history and melt pool characteristics in a fast-acting manner during the thermal process of an AM part. While high-fidelity numerical simulations, such as finite difference, volume, or element, are required to precisely capture the physics in the AM thermal processes, their high computational cost makes them impractical for process design in the context of the ICME paradigm, particularly the processes involving forward-feeding and in-line feedback control. Therefore, the development of low-fidelity fast-acting analytical models with comparable precision is essential to a successful approach in tackling AM design problems.

4.3.1.1 Assumptions

The DSM enables fast-acting temperature predictions of AM parts by simulating thermal history while accounting for a series of key assumptions. These assumptions offer a balance between computational cost and accuracy. In this regard, the main considerations fall into the categories of thermophysical properties and heat transfer.

For the purpose of predicting AM melt pool characteristics, Schwalbach et. al [94] has quantified small differences resulting from material property temperature dependence. From this, temperature-independent thermophysical properties are thus assumed by the DSM in this work. Additionally, experiments are utilized in a probabilistic calibration of the model to provide effective thermophysical property values alongside the property's associated distributions. Uncertainties stemming from the temperature-independence assumptions are accounted for through the calibration procedure.

Heat transfer within the material system is directly governed by thermal conduction. Additionally, material absorption and thermal transport mechanisms including convection and radiation, as well as evaporation, are accounted for through a calibrated efficiency parameter. Considering the dependence of melt pool shape on convection, a shape factor variable to adjust the volumetric energy source and consequent melt pool geometry for a given set of process conditions can be tuned and calibrated [94]. However, a calibrated shape factor is not transferable to multiple process parameters within the same material system and will result in extensive computational cost when screening for trends. For this reason, the shape factor is assumed to have a value equal to 1, but a generalized physics-based depth correction factor is considered [99] and calibrated with experiments for cases when the AM process is characterized by keyholing mode through a criterion derived from NiTiHf printability maps [134]. This presents significant disparities in melt pool width to depth ratios for the keyholing conditions due to substantial evaporation of material and corresponding recoil pressure [96].

In the context of heat transfer and temperature distribution of the melt pool, latent heat due to liquid-solid and solid-state phase change, as well as sensible heat, are also considered, subsumed by a calibrated effective heat capacity parameter. The calibration approach and results for the thermophysical properties, efficiency, and depth correction are discussed in Section 4.3.3 and Section 4.3.4, respectively.

4.3.1.2 Thermal Profile

The DSM predicts temperature, T, at any given spatial location along the x, y, and z coordinates, $\vec{r}_j$, over the AM process. These predictions at any given process time, t, provide isotherm contours that are used to determine the melt pool dimensions based on the material melting temperature. In this model, the temperature prediction is performed by solving the heat conduction equation in the presence of a series of volumetric discrete heat sources, $\{\hat{s}_i\}_{i=1}^{N}$, at designated locations, $\{\vec{r}_i\}_{i=1}^{N}$, which sequentially activate at different process times, $\{\vec{\tau}_i\}_{i=1}^{N}$, depending on the laser beam velocity, v. This equation is expressed as:

$$\frac{\partial T}{\partial t} = D\nabla^2 T + \sum_{i=1}^{N} \frac{\hat{s}_i(\vec{r}_j, t)}{\rho C_p} \tag{4.1}$$

where D, ρ, and c_p are the thermal diffusivity, mass density, and mass specific heat capacity of the given material, respectively. As mentioned in Section 4.3.1.1, these parameters are considered temperature-independent and represented by their effective quantities. It should also be noted that the thermal diffusivity can be related to the thermal conductivity, κ, as $D = \frac{\kappa}{\rho C_p}$. Assuming normally-distributed volumetric heat sources centered at $\vec{r}_i$ with standard deviation, σ representing the beam size, the following solution based on Green's function technique can be derived from Equation 4.1 for an infinite uniform medium assigned at initial temperature T_0:

$$T(\vec{r}_j, t) = T_0 + \sum_{i=1}^{N} \left\{ \frac{\eta_i P_i \Delta t}{\rho C_p \sqrt{2}\pi^{1.5}} \Theta(t-\tau_i)\left(\sigma^2 + 2D(t-\tau_i)\right)^{-1.5} \exp\left(- \frac{R_{ij}^2}{2\left(\sigma^2 + 2D(t-\tau_i)\right)} \right) \right\} \tag{4.2}$$

where η_i is an adjusting factor called efficiency, indicating the energy received by the material from the heat source $\hat{s}_i$. In other words, this factor accounts for the energy loss due to convection, radiation, and evaporation phenomena in the final solution. While P_i is the power of heat source i, $\eta_i P_i$ is known as its effective power. η_i and P_i are considered fixed in this work and denoted by η and P. Δt is the source discretization timescale. $R_{ij} = |\vec{r}_j - \vec{r}_i|$ corresponds to the distance between the given spatial position and the position of the heat source $\hat{s}_i$. Θ is the Heaviside step function accounting for the contribution of heat sources activated at process time t. For further information about DSM, the readers are referred to [94].

4.3.1.3 Melt Pool Geometry

LPBF AM process parameters and material properties directly affect melt pool geometry and structure. For a given material, modulating laser power, laser speed, and hatch spacing translates to different energy inputs into the system and variations in melt pool geometry. Even within a single layer there is variation in location-specific energy, resulting in unique melting and solidification events throughout the AM process. Proper evaluation of these events at specific points in time then enables the approximation of corresponding melt pool geometries. By leveraging the DSM to simulate a desired print, melt pool geometries for any point in time and at any spatial location can be generated.

Resolving melt pool dimensions follows a short sequence beginning with the generation of an AM layer based on desired process parameters. Next, a specific point of interest on the simulated layer is chosen and the thermal history is generated. For the identification of a specific thermal event within the thermal history, an approximate range of times corresponding to the melting and solidification event should also be specified. The material's melt temperature is then used as a criterion to determine the start and end, respectively the melting and solidification time, of the thermal event. The melt pool width and depth are then determined by querying points for the solidification temperature in a radial vector search pattern originating from the location of interest, bounded by the timing of the thermal event. This results in a cross-section of queried points, where the thermal history of each point should be resolved to determine a respective duration of the thermal event, defined by the melting and solidification time. Under the steady-state assumption, the length for each point in the cross-section can then be calculated as a summation of its length before, L_B, and length after, L_F, the cross-section, as shown in Figure 4.2. These lengths are based on the distance travelled by the laser relative to the solidification time of the cross-section boundary points, where length is zero, and both the solidification time and melting time of individual points within the cross-section. The total length $L_{(y,z)}$ corresponding to a specific point in the cross-section can be solved as:

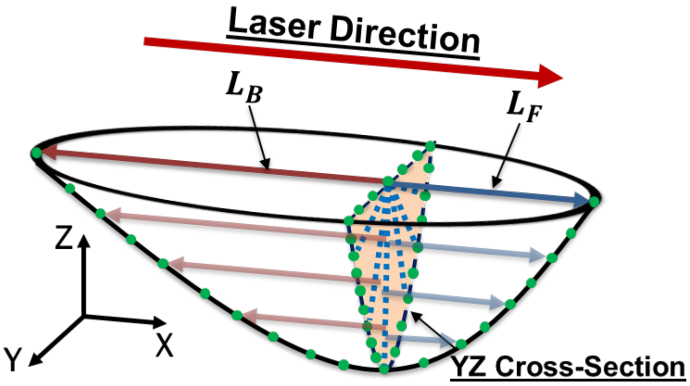

Fig. 4.2. Sample melt pool with queried points in the YZ cross-section. The melt pool length corresponding to any point in the cross-section is comprised of components for both the length before, L_B, and the length in front, L_F, of the cross-section.

$$L_{(y,z)} = [L_B + L_F]\upsilon = \Big[\big(t_{solid,(y,z)} - t_{solid,min}\big) + \big(t_{solid,min} - t_{melt,(y,z)}\big)\Big]\upsilon \tag{4.3}$$

where $t_{solid,(y,z)}$ and $t_{melt,(y,z)}$ are the solidification and melting time of a point in the cross-section, respectively, $t_{solid,min}$ is the earliest solidification time from all points in the cross-section, and υ is the laser velocity. By generating lengths for each point in the cross-section, an approximation of the 3D melt pool is resolved and a melt pool volume is determined. This is a critical component to calculating chemistry propagation through an AM part, discussed in Section 4.4.

4.3.1.4 Prediction Correction for the Keyhole Depth

Keyholing is a common defect in the AM processes which occurs in high input energy processes resulting from specific combinations of high laser power and low laser velocity. In these conditions, materials' incapability of dissipating sufficient heat from the melt pool underneath the laser beam leads to a local increase in temperature above the materials boiling point, inducing massive elemental evaporation from the melt pool. Therefore, an evaporation-induced force, also known as the recoil pressure, is produced in an opposite direction perpendicular to the melt pool surface [14, 135]. When the recoil pressure is larger than its opposing counterpart resulting from surface tension, it forms a vapor cavity by pushing out its inner molten material. This cavity promotes heat absorption and enables the laser beam to penetrate deeper than non-keyhole conditions [98].

Analytical thermal models, such as the model described in Section 4.3.1, typically ignore the physics involved in keyholing mode, resulting in melt pool depth underestimation at these conditions. For this reason, the same depth correction as our previous studies [14, 135] is applied here for cases undergoing the keyholing phenomenon. This correction is taken into account using the simplified analytical model for the keyhole depth, d_k, suggested by Gladush and Smurov [99], which is derived by solving the heat conduction equation for a cylindrical-assumed keyhole of radius σ under the laser beam with a semi-infinite boundary condition. The final general solution is expressed in terms of the processing conditions, i.e., laser power, velocity, and beam size, as well as some materials properties, as follows:

$$d_k = \frac{\eta P}{2\pi\kappa T_b}\ln\left(\frac{\sigma + \frac{D}{v}}{\sigma}\right) \tag{4.4}$$

where T_b is the material boiling temperature alongside other previously defined properties.

Assuming the depth prediction in Equation 4.4 can perfectly represent the experimental data for keyhole depths, the discrepancy between the DSM prediction and experimental data is considered a constant fraction of this depth under the keyholing conditions. This constant fraction is called the correction factor, C, in our studies in order to account for keyholing missing physics in the DSM and calibrated probabilistically besides other uncertain model parameters against available experimental data for melt pool dimensions. The correction factor should change between 0 and 1 based on the high-precision assumption for Equation 4.4. However, our previous studies [14, 135] showed that it can be higher than 1 since the keyhole depth can still be underestimated by Equation 4.4.

For the sake of parameter calibration, an experimentally-derived criterion is used to identify the processing conditions in the given data corresponding to the keyholing occurrence, at which the DSM depth predictions are required to be corrected. This criterion is expressed as an inequality between melt pool width, w_{exp}, and depth, d_{exp}, as $(w_{exp}/1.5) \leq d_{exp}$ for Ni-based SMAs, which corresponds to a classified P-v region in the printability maps for these alloys [144]. Therefore, the depth correction can also be performed based on a criterion for the combinatory values of P and v input into the thermal model.

4.3.2 Experimental Procedure

$Ni_{50.3}Ti_{29.7}Hf_{20}$ (at.%) ingots were acquired from Ingpuls GmbH and then gas atomized by Nanoval GmbH & Co. KG. The atomized powder possessed a D80 (80th percentile of particle size distribution) of 41 μm and was utilized for single track and solid specimen fabrication throughout this study. Thin disks of the NiTiHf were cut by wire electrical discharge machining (wire-EDM) for printing NiTiHf single tracks. Fifty four single tracks with length of 10 mm and spacing of 1 mm were fabricated using DMP ProX 200 LPBF system by 3D Systems with different combinations of laser power and scanning speed under argon atmosphere. These print conditions, their linear energy density (LED), and their corresponding average values of melt pool width and depth are listed in Table 4.1. Additionally, these prints are split into training and test sets to calibrate and validate the thermal model parameters.

After the single track experiments, top-view optical microscopy (OM) images were taken at the middle of each single track using a Keyence VH-X digital microscope, and the widths were measured and averaged at five different locations from the OM images. For each single track, three cross-sectional samples were cut using wire-EDM at equal-spaced distance. The cross-sectional samples were mechanically polished up to 1200 grit, followed by a final polishing with colloidal silica solution. In order to reveal the melt pool shapes, the polished samples were etched with the etchant (3 parts HNO_3, 1 part HF, 10 parts distilled water). OM was carried out on each etched cross-section to measure the melt pool depths, and the average of three cross-sectional samples was calculated for each single track. Figure 4.3 contains cross-section images of these single-track prints for several processing conditions, characterizing differences in melt pool geometry for lack of fusion, good quality, balling, and keyholing print modes.

4.3.3 Probabilistic Calibration Approach

Computer models are always imperfect due to the incomplete parameterization and physical knowledge incorporated in these models [101]. Therefore, model calibration is required and should utilize a probabilistic approach in order to assess validity [145]. Bayesian inference is a simple and straightforward approach that applies the Bayes' theorem to identify the probability of the parameter quantities represented by a parameter posterior density function (PDF), given the observed data, $\mathbf{D}$, and parameter prior information, $\mathbf{I}$. Parameter posterior probability, $p(\theta|\mathbf{D},\mathbf{I})$, is proportional to the product of parameter prior probability, $p(\theta|\mathbf{I})$, and likelihood, $p(\mathbf{D}|\theta,\mathbf{I})$ in this context [146]. However, this inference typically involves solving multi-dimensional intractable integrals to determine the posterior statistical characteristics. These integrations are difficult or often impossible to compute through the analytical and conventional numerical methods [101, 147]. Markov Chain Monte Carlo sampling techniques are mostly used in order to tackle these integration problems in a robust and straightforward manner [148–150].

Table 4.1. Average measured melt pool width and depth for single-track prints at different LPBF process conditions over $Ni_{50.3}Ti_{29.7}Hf_{20}$ (at.%) powder. Experimental data selected for the calibration and validation of the thermal model are separated.

P (W)	u (mm/s)	LED (J/m)	$\bar{w}$ (μm)	$\bar{d}$ (μm)
Training Data for Thermal Model Calibration				
40	80	500.0	126.9	21.4
80	80	1000.0	244.9	64.9
120	80	1500.0	385.6	235.3
160	80	2000.0	462.7	400.9
240	80	3000.0	551.2	721.8
40	330	121.2	83.1	9.4
80	330	242.4	116.4	42.3
120	330	363.6	173.6	129.7
160	330	484.8	206.6	222.5
200	330	606.1	227.7	247.3
80	580	137.9	97.2	32.4
120	580	206.9	125.0	63.4
200	580	344.8	165.9	100.8
240	580	413.8	173.6	112.3
80	830	96.4	78.7	11.6
120	830	144.6	113.2	42.3
160	830	192.8	137.8	71.3
200	830	241.0	142.9	72.8
240	830	289.2	157.0	144.1
80	1080	74.1	73.9	11.6
160	1080	148.1	113.5	57.0
240	1080	222.2	138.4	94.8
80	1330	60.2	74.6	6.8
120	1330	90.2	80.6	17.8
160	1330	120.3	83.8	40.8
240	1330	180.5	109.4	78.3
160	1580	101.3	74.8	32.7
200	1580	126.6	79.0	49.3
120	1830	65.6	72.3	10.8
160	1830	87.4	66.8	27.4
240	1830	131.1	69.1	53.5
120	2080	57.7	68.5	7.6
160	2080	76.9	59.8	23.2
200	2080	96.2	59.5	34.2
240	2080	115.4	67.8	39.1
120	2330	51.5	69.8	8.7
160	2330	68.7	58.5	20.2
240	2330	103.0	68.7	43.8
60	205	292.7	101.0	16.8
100	205	487.8	181.9	51.8
140	205	682.9	248.4	183.5
100	455	219.8	109.0	35.4
140	455	307.7	162.4	71.5
Test Data for Thermal Model Validation				
200	80	2500.0	522.5	557.0
240	330	727.3	240.4	320.3
160	580	275.9	158.3	74.0
120	1080	111.1	84.4	28.1
200	1080	185.2	123.1	71.5
200	1330	150.4	94.0	55.5
120	1580	75.9	76.8	10.4
240	1580	151.9	75.5	63.4
200	1830	109.3	73.9	38.4
200	2330	85.8	63.9	26.9
60	455	131.7	77.8	9.5

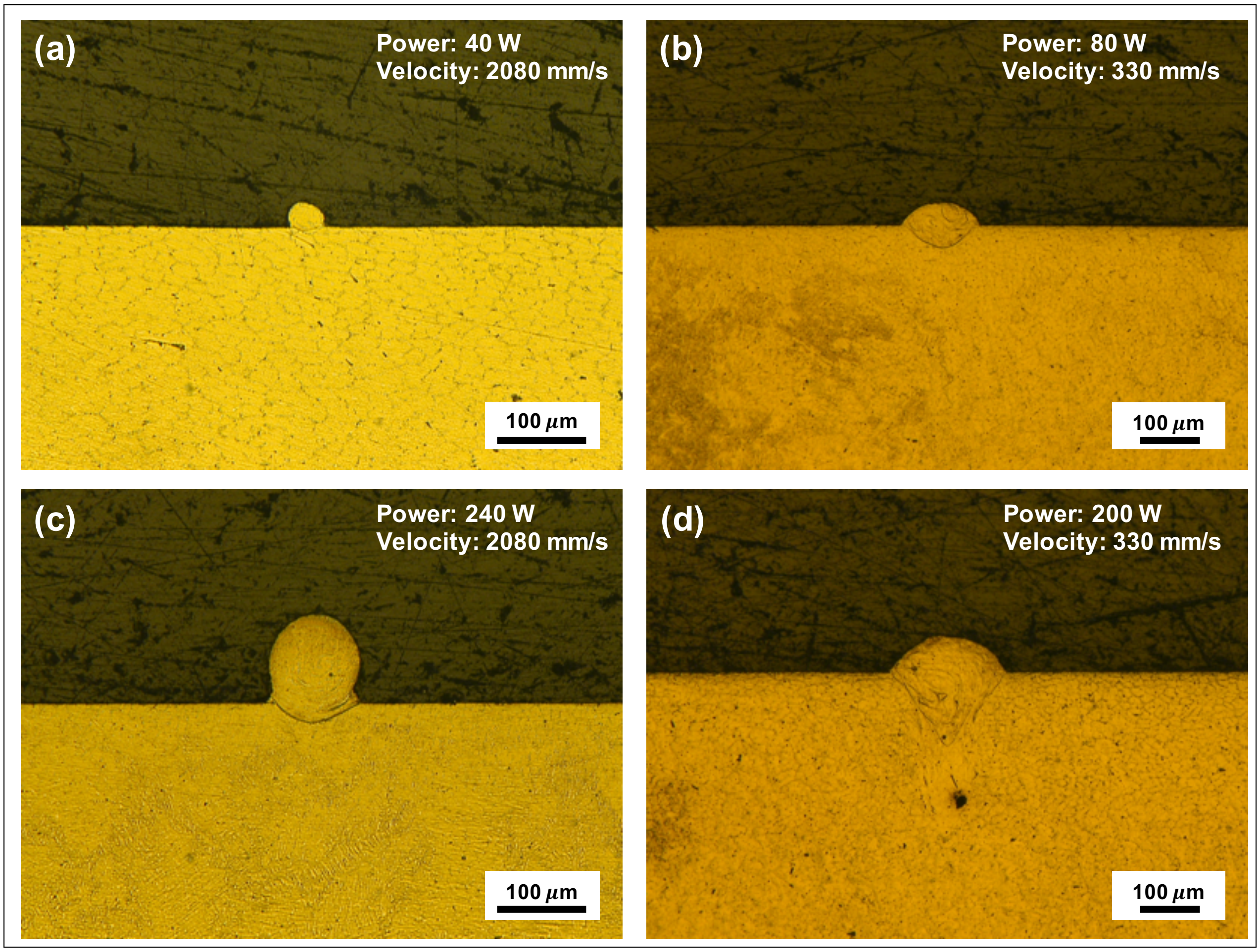

Fig. 4.3. Cross-section images for LPBF $Ni_{50.3}Ti_{29.7}Hf_{20}$ single-track prints obtained through optical microscopy. Based on print conditions, different print modes are experienced: (a) lack of fusion (b) good quality (c) balling (d) keyholing.

In this work, an MCMC toolbox in Matlab [151] based on the adaptive Metropolis-Hastings algorithm is employed to infer the posterior distribution of the model parameters. For this purpose, parameter vectors are sampled from this multivariate posterior distribution, iteratively, after defining the parameters' initial guess, bounds, and prior distribution. In each iteration of this process denoted by index i, a candidate, θ^{cand}, is sampled from a proposal posterior distribution, $\mathbf{q}$. In the beginning, the proposal distribution is considered as a multivariate Gaussian proposal distribution centered at the parameters' initial guess with an arbitrary variance-covariance matrix. Then, it is adapted to a multivariate Gaussian distribution centered at the previous parameter vector, $\theta^{(i-1)}$, in the MCMC chain with a variance-covariance matrix calculated as a function of the variance-covariance matrix of all the previous parameter vectors in the chain, based on Haario et al.'s works [100, 152]. The acceptance/rejection of the sampled candidate is performed based on the Metropolis- Hastings (MH) ratio that is:

$$MH = \frac{p(\theta^{cand}|\mathbf{I})p(\mathbf{D}|\theta^{cand},\mathbf{I})}{p(\theta^{i-1}|\mathbf{I})p(\mathbf{D}|\theta^{i-1},\mathbf{I})}\frac{q(\theta^{i-1}|\theta^{cand})}{q(\theta^{cand}|\theta^{i-1})}, \quad i = \{1, ..., n\} \tag{4.5}$$

where the first ratio is the Metropolis ratio expressed as the product of the prior probability of θ^{cand} and the likelihood of obtaining the observed data given this sample over its counterpart given $\theta^{(i-1)}$. In other words, the posterior probabilities of θ^{cand} and $\theta^{(i-1)}$ are compared through this ratio. It should be noted that the parameter prior distribution is defined based on prior knowledge about the parameters. However, a non-informative distribution, e.g., uniform, is considered when no previous information is available. Moreover, likelihood is a multivariate Gaussian distribution in the applied MCMC toolbox, which compares a vector of the observed data at different input conditions with its corresponding vector of model outputs at any given theta. This multivariate Gaussian distribution is centered at the observed data vector with a diagonal variance-covariance matrix of data variances.

The second ratio in Equation 4.5 is the Hastings ratio that compares the probability of moving forward from $\theta^{(i-1)}$ to θ^{cand} with its counterpart for the reverse move. The parameter vector candidate is accepted if the MH ratio is higher than a random value between 0 and 1. This is equivalent to an acceptance probability of min$\{MH, 1\}$ for the candidate. θ^i equals θ^{cand} in the case θ^{cand} is accepted; otherwise, θ^i is the same as $\theta^{(i-1)}$. The iterative sampling of parameter vectors continues until the proposal distribution becomes almost stationary, which is generally equivalent to parameter convergence in the MCMC process. Then, the parameter samples generated after the convergence can represent the parameter posterior PDF and its statistical properties for the sake of parameter calibration and uncertainty quantification. The model outputs at these parameter samples are used to find uncertainties propagated from the parameters to the model outputs. Moreover, 2.5% of the model output samples can be discarded from their upper and lower bounds to predict 95% credible intervals (CIs).

4.3.4 Calibration Results

The DSM, similar to all models with any range of fidelity or precision, is incapable of emulating reality perfectly due to its assumptions, simplifications, and incomplete physics. Therefore, the quantification of existing errors is required in order to have a notion of confidence for the model predictions, enabling the application of such a model in design methodologies. For this purpose, the Bayesian MCMC inference method described in Section 4.3.3 is applied to perform the probabilistic calibration of the model parameters against the closest information source to reality, i.e., experimental data. Then, the parameter uncertainties are propagated to the model outputs in order to have predictions within uncertainty bounds at any given processing condition.

Out of 54 available experimental data points for melt pool width and depth presented in Table 4.1 at different processing conditions of printing $Ni_{50.3}Ti_{29.7}Hf_{20.0}$ SMA single-tracks, 43 data points (80%) are considered as training data for the probabilistic calibration and the rest (20%) are used as test data for the validation of the calibrated model. It should be noted that the Bayesian inference provides the best plausible results based on the current experimental information and is not impeded by the number of data points. However, this statistical inference can be updated when more data is available.

Using all the training experimental data points from both conduction and keyholing modes at the same time, the uncertain model parameters, i.e., η, k_{eff}, C_{p-eff}, and C, are probabilistically calibrated through the MCMC sampling approach in a multi-objective optimization scheme. This process starts by considering appropriate ranges for parameters based on the physical constraints and expert intuition alongside a uniform prior distribution due to the lack of knowledge about the parameters' distribution form. Subsequently, 20,000 parameter vector samples are generated using the MH criterion discussed in Section 4.3.3. After discarding the burn-in period from the sample chain, the parameter vector samples represent a multivariate joint posterior probability density function (PDF) for the parameters that is illustrated through the marginal (individual) and bivariate (pair) joint parameter PDFs in Figures 4.4 and 4.5, respectively. The statistical properties of the marginal PDFs that include the mean and standard deviation of samples for the individual parameters are reported in Table 4.2 as their calibrated values and uncertainties. Also, the pair joint PDFs that show the probability densities in the parameter pair spaces in different colors, increasing from blue to red, imply the extent of linear correlation between each parameter pair in a qualitative manner through the linearity of color features.

The Pearson correlation coefficient, $r_{XY} = cov(X,Y)/\sigma_X\sigma_Y$, provides a quantitative measure enabling the comparison of the linear correlations, where σ_X, σ_Y, and $cov(X,Y)$ are the standard deviation of parameter X, the standard deviation of parameter Y, and the covariance of these two parameters, respectively. This quantitative parameter alters from -1 to 1. The upper and lower bounds correspond to a full linear correlation between the given parameter pair, contrarily 0 implies no linear correlation. Also, the negative and positive signs indicate the correlation direction, meaning whether the value of one of the pairs decreases or increases as the value of the other pair increases. As shown in the bottom right corner of plots in Figure 4.5, there is almost a full linear correlation between η and C_{p-eff} and fairly high correlations between η and k_{eff} as well as k_{eff} and C_{p-eff}. These correlations can also be observed in the marginal PDFs in Figure 4.4. Part (c) of this figure shows that the C_{p-eff} distribution peak falls beyond the lower bound of this parameter since the probability density increases as the C_{p-eff} value approaches the lower bound. However, having a parameter value under its lower bound is physically unreasonable, which can result from assumptions and missing physics in the DSM or errors in the experimental results. As a result of a very high linear correlation between η and C_{p-eff} (r = 0.99), Figure 4.4-(a) also shows a very similar marginal PDF for η. However, as shown in Figure 4.4-(b), the marginal PDF in the case of k_{eff} is less similar to the one for C_{p-eff} and mostly shows a double peak distribution as the linear correlation drops to 0.81. Figure 4.5 also exhibits low linear correlations between C and the other three parameters, indicating C has an independent contribution to predictions and cannot be replaced by the mentioned model parameters. This independent behavior results in a clear peak in the marginal PDF of parameter C in Figure 4.4-(d).

The most plausible values and uncertainties of the DSM parameters listed in Table 4.2 are propagated to the model outputs, i.e., melt pool width and depth, through the model forward analysis of the parameter mean vector and the MCMC parameter vector samples after discarding the burn-in period. In this UP scheme, 2.5% of the output samples for melt pool width or depth are discarded from the upper and lower bounds of the sorted output samples in order to obtain 95% CIs at each experimental print condition. These probabilistic predictions versus their corresponding experimental data are plotted in Figure 4.6 for both training (part (a) and (b)) and test (part (c) and (d)) experimental conditions. Colors in this figure represent the LED values at different print conditions. As observed in Figure 4.6-(a) and (b), the predictions of the calibrated DSM model are in excellent agreement with their corresponding training data with R^2 and RMSE values of 0.94 and 32 μm for melt pool width and 0.93 and 43 μm for melt pool depth. Comparable R^2 and RMSE values of 0.95 and 35 μm for melt pool width and 0.97 and 31 μm for melt pool depth for test-experimental conditions in Figure 4.6-(c) and (d) also validate the calibration results with no over-fitting. Therefore, the calibrated DSM model is applied in our multi-model framework in Section 4.4 and Section 4.5 to predict melt pool overlap, evaporation flux, final chemistry, and transformation temperatures for different print conditions of cuboid specimen.

Table 4.2. The most plausible (mean) values and standard deviation of the DSM parameters after the MCMC calibration against the experimental data for $Ni_{50.3}Ti_{29.7}Hf_{20.0}$ SMA single-track melt pool dimensions.

η	κ **(W/m K)**	$\mathbf{C_p}$ **(J/kg K)**	**C**
0.64 ± 0.08	13.22 ± 1.87	652.53 ± 76.38	0.81 ± 0.03

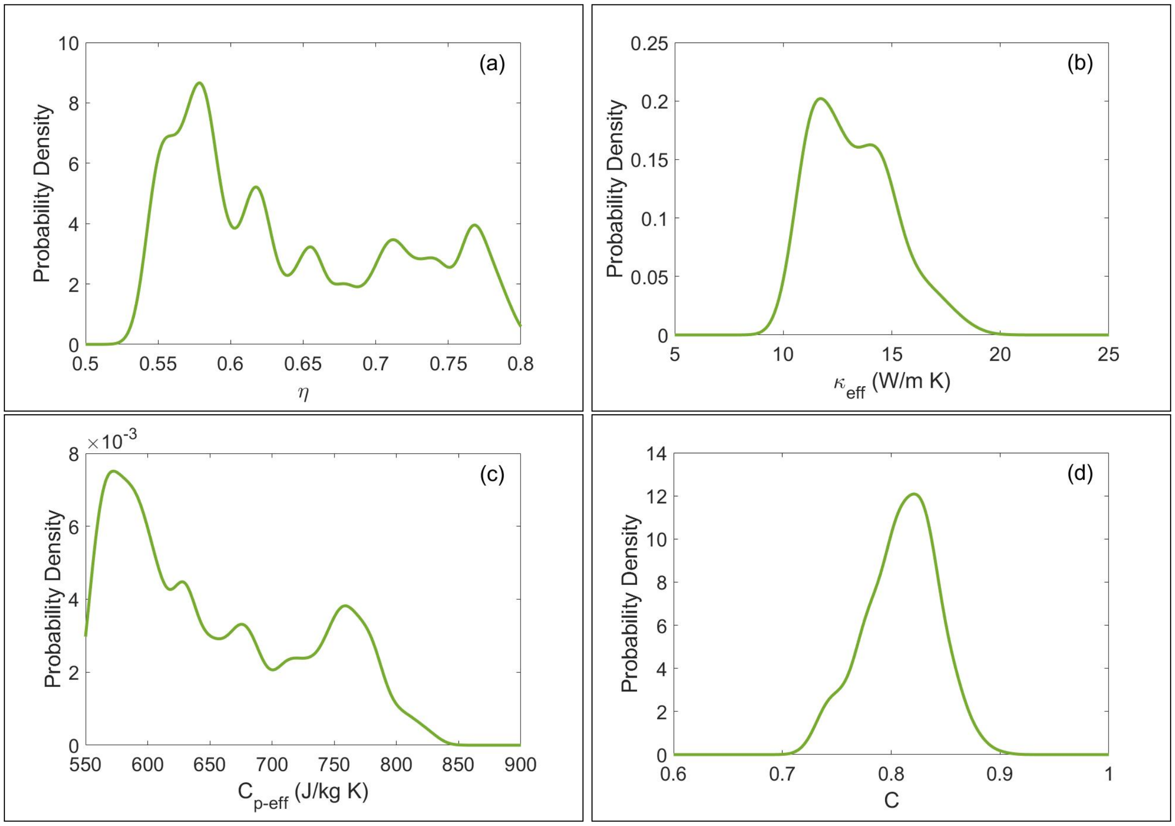

Fig. 4.4. Marginal posterior PDFs of the DSM parameters obtained after the MCMC calibration against the experimental data for $Ni_{50.3}Ti_{29.7}Hf_{20.0}$ SMA single-track melt pool dimensions.

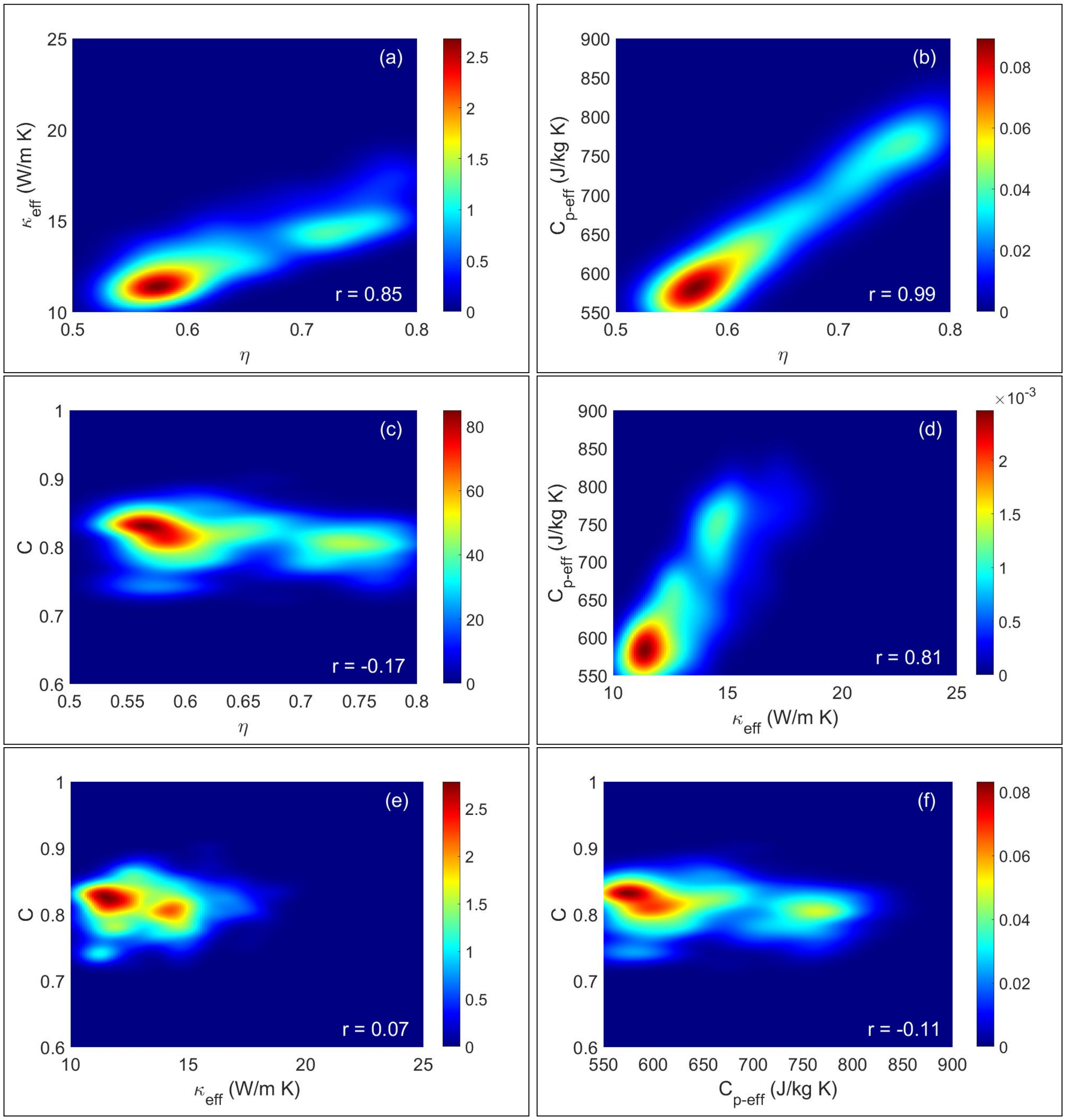

Fig. 4.5. Bivariate joint posterior PDFs of the DSM parameters obtained after the MCMC calibration against the experimental data for $Ni_{50.3}Ti_{29.7}Hf_{20.0}$ SMA single-track melt pool dimensions.

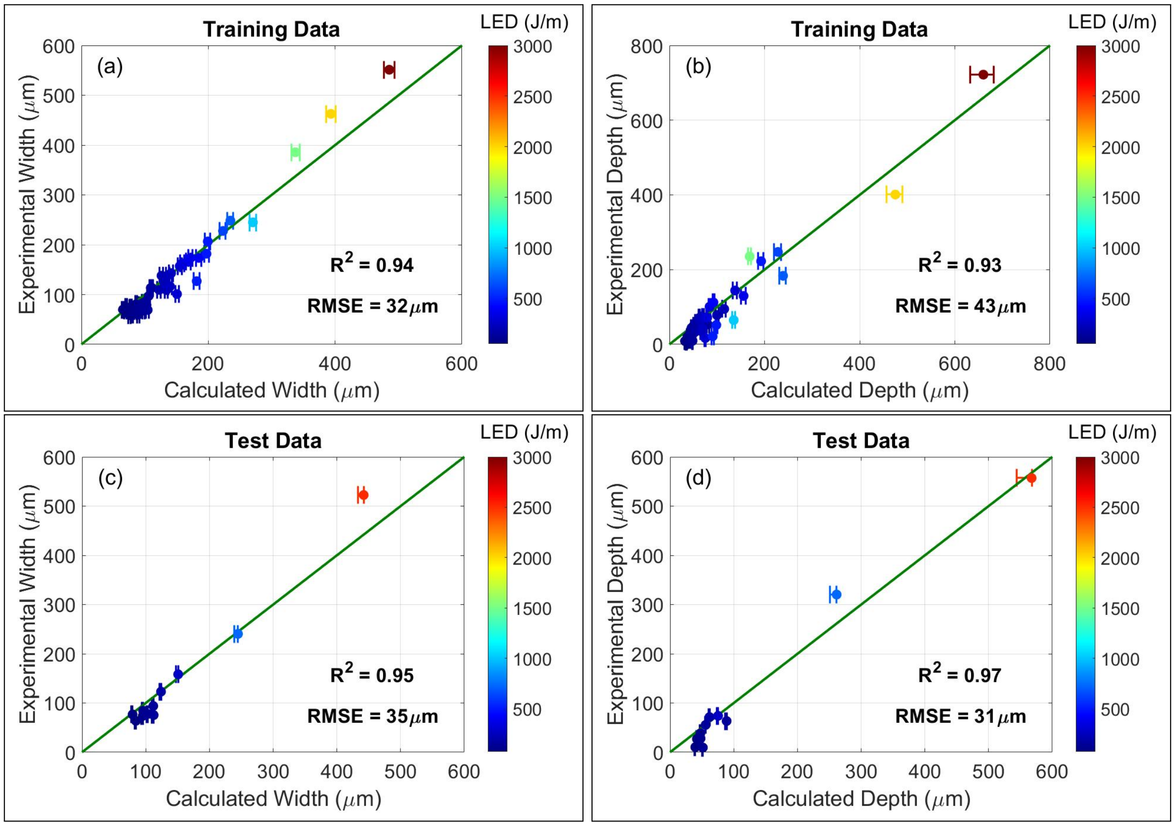

Fig. 4.6. Calibrated DSM predictions with 95% CIs vs. experimental training and test data for the melt pool width and depth at different given $Ni_{50.3}Ti_{29.7}Hf_{20.0}$ SMA single-track print conditions.

4.4 Chemistry Propagation Across Melt Pools

4.4.1 Multi-Layer Model

A multi-layer model (MLM) proposed by Ranaiefar et al. [14] is applied in this work to assess melt pool overlaps resulting from the AM process and to account for chemistry propagation across a part. The MLM is important for appropriately defining the PSPP chain of an AM part because it assists in accounting for the multiple thermal events and the associated evaporation of alloying elements which occur during the AM fabrication process. By simulating multiple layers within an AM part and the corresponding melt pool overlap and differential evaporation, the model framework takes an additional step towards becoming a fast-acting 3D model, analog to a digital twin, ideal for screening PSPP trends. Additionally, the MLM receives melt pool geometry input directly from the calibrated DSM and does not require direct calibration as there are no uncertain parameters in this model.

4.4.1.1 Assumptions

Simulating each of the hundreds to thousands of layers fabricated during the AM process is computationally expensive and impractical in the context of utilizing the model framework to screen for PSPP trends and accelerated development in design. For this reason, the MLM implements a series of assumptions to reduce computational cost for the simulation of multiple layers. In this regard, the main considerations fall into the categories of preheat effects and melt pool overlap.

During the AM process, there are both intralayer and interlayer preheating effects which impact melt pool dimensions. Intralayer preheating describes the diffusion and build-up of heat across a single layer. The influence of intralayer preheating on melt pool dimensions is highly dependent on the scan strategy and the part shape, where small hatch spacing and quick turn-arounds result in larger preheat temperatures in adjacent tracks relative to increased hatch spacing and delayed turn-around times. When a region with raised preheat temperature is processed, the thermal field at a point in time, defined by the melting temperature, would be larger than at a point with no or less thermal build-up. This intralayer preheating effect is inherently accounted for through the DSM and translates to larger melt pool volumes and variations in melt pool overlap.

In the current work, a conventional snaking scan strategy is utilized by the DSM, where an initial thermal build-up is experienced through the first several tracks until an approximately steady-state preheat is experienced by the remaining tracks. These thermal build-up events correspond to an increase in melt pool dimensions for each track until the steady-state intralayer preheating is reached, resulting in approximately equivalent melt pool widths and depths for the remaining tracks. The start of this steady-state region varies between process parameters, but can be leveraged to reduce computational cost by setting a melt pool dimension-based criterion. For this reason, it is assumed that if a point on the current track and a parallel point on the prior track entertain a desired tolerance of $10e^{-15}$ μm in width and depth, then the steady-state region has been reached and all remaining tracks have the same dimensions.

Interlayer preheating refers to the effect of residual heat on the processing of an AM layer resulting from the processing of the prior layer. Again, the influence of interlayer preheating on melt pool dimensions is highly dependent on the AM process parameters and scan strategy. Due to the intrinsic time-temperature process of AM, as a single layer is printed it experiences thermal diffusion and, given enough time, eventually cools to room temperature. This layer may now act as a substrate and allow the next layer to be printed in conditions similar to the first layer. This results in melt pool dimensions that are constant through each progressive layer. In the case where insufficient time is given between printed layers, the residual heat build-up could result in slightly larger melt pools and variation in melt pool geometry for progressive layers. Therefore, assuming enough time is given to diminish interlayer preheating effects allows the use of a single predicted layer to model all layers of the AM build and reduce the overall computational cost. This directly correlates to the improved efficiency of the model framework for quickly simulating AM components to screen location-specific properties and guide experiments. For this reason, it is assumed that interlayer preheating is negligible.

Similar to preheating effects, the degree of melt pool overlap with adjacent solidified melt pools also varies based on process parameters and scan strategy. In some cases, the degree of melt pool overlap with solidified tracks from the same or previous layer is marginal, resulting in minor interaction and minimal chemistry propagation. However, the increased computational cost for calculating these small melt pool overlaps remains. For this reason, it is assumed that overlaps comprised of less than 1% of the melt pool cross-sectional area are considered negligible. The implementation and consideration of melt pool overlaps within the model framework are discussed in greater detail in Section 4.4.1.2.

4.4.1.2 Melt Pool Overlap

Melt pool overlap refers to the multiple melting and solidification events occurring on both adjacent tracks and adjacent layers during the AM process, resulting in repeated processing and interaction of melt pool regions. Then by accurately modeling and capturing these melt pool overlaps, the processed chemistry within each melt pool can be propagated across successive melt pools, resulting in the identification of location specific chemistry across the AM part.

The degree of melt pool overlap within an AM build varies based on material properties and process parameters, where process parameters are user-defined. By manipulating process parameters such as hatch spacing, the melt pool overlap and printability of an AM part can be directly controlled, as well as its properties [134]. Scenarios of AM processing with small hatch spacing may produce melt pools which experience overlap with multiple adjacent tracks, while a large enough hatch spacing could result in lack of fusion defects and no overlap. Another aspect to consider with smaller hatch spacing is the corresponding increased volumetric energy density and an increased significance for the evaporation of alloying elements from the melt pool, further influencing location-specific chemistry and properties. The MLM works in concert with a differential evaporation model discussed in Section 4.5 to account for the loss of alloying elements due to evaporation.

Melt pool overlap is also affected to a varying degree by intralayer preheating, which itself is dependent on scan strategy and part geometry. In the current work, the DSM utilizes a conventional snaking pattern along a square geometry with tracks running parallel to the X-axis, as illustrated in Figure 4.7. The thermal history within the layer could then be defined by transient regions where thermal events are in greater flux, located near the start and end of each track, and a larger steady-state region where thermal history is constant, located about the center of each track [153]. The melt pool dimensions for a point along a single-track in the steady-state region could then be repeated for remaining points within the steady-state region of the track. Due to the assumption of negligible interlayer preheating and negligible chemistry effect (across small changes in chemistry) on melt pool dimensions, this single melt pool can also represent the melt pool dimensions in the proceeding layer. By extension, a slice of resolved melt pool dimensions in the XY-plane, for a single layer, effectively captures and simulates the complete 3D steady-state region of the AM part.

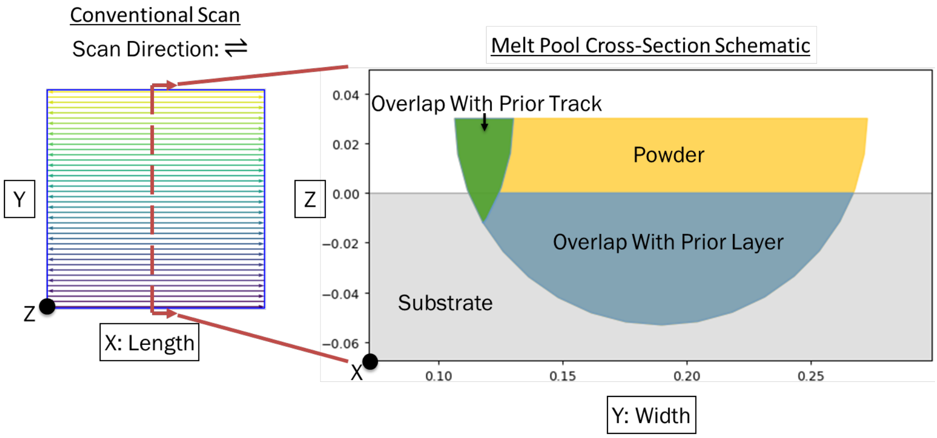

Fig. 4.7. Conventional snaking scan strategy and melt pool cross-section schematic depicting a sample case for melt pool overlap, where the Z-axis represents the build-direction.

After the AM layers have been simulated, the process of evaluating melt pool overlaps and chemistry propagation begins with the first melt pool. The melt pool cross-section along the XY-plane is compared with prior melt pool cross-sections along the same plane, as well as the substrate. If no overlap is found, then a lack of fusion defect is likely present and subsequent analysis unnecessary. In the case of multiple overlaps, a precedent is set based on print-time hierarchy. In the case of the first melt pool, the only overlap should be with the substrate. The entirety of the overlap can then be used to determine overlap volume and an average composition calculated based on both powder and substrate volume and composition. This average composition will then be utilized by the differential evaporation model to determine the final solidified melt pool composition after evaporation.

Next, the second melt pool should overlap with the prior melt pool as well as the substrate. Referring to the print-time hierarchy, the overlap with the most recent solidified melt pool should be considered first. From Figure 4.7, the referenced overlap could refer to the green region within the melt pool cross-section schematic. This region partially extends into the former substrate region, as it was processed within the first melt pool and corresponds to the first melt pool's calculated chemistry. The substrate cross-section overlap is then represented by the blue region and substrate chemistry. Similar to the first melt pool, these overlaps and compositions are then used to determine the second melt pool's average composition. Through this process, the propagation of chemistry through the first two melt pools has been considered. Similarly, this process can be repeated for remaining melt pools within layer and for proceeding layers, effectively capturing location-specific chemistry and chemistry propagation throughout the AM part.

It can be noted that because of constant process parameters and negligible interlayer preheating, a symmetric pattern in melt pool overlap can be drawn from the simulated layers. The number of overlaps will vary based on process parameters, but generally melt pools will only overlap with prior tracks within the same layer and several tracks within the prior layer. Due to consistent depths in the simulated melt pool geometries, melt pools do not extend 2 layers prior and melt pool overlap search criteria can account for this to further reduce computational cost. This is beneficial when an AM part can consist of hundreds of tracks and layers, requiring thousands of melt pools to be accounted for. In the case that variable process parameters modulate within a single build, the search criteria should be re-evaluated to capture appropriate melt pool overlaps and chemistry propagation.

4.5 Evaporation Induced Chemical Analysis

4.5.1 Differential Evaporation Model

A differential evaporation model (DEM) proposed by [14] is adapted for this work to evaluate melt pool evaporation throughout the AM fabrication process, providing location-specific final chemistry and transformation temperature properties for the ternary NiTiHf system. The DEM is important in the ICME framework to accurately correlate PSPP relationships by accounting for changes in melt pool chemistry resulting from the extensive thermal processing and the corresponding evaporation loss of alloying elements experienced by AM components. In this regard, the melt pool post-evaporation predicted chemistry can be correlated to location-specific properties, such as martensitic start transformation temperature in SMAs. Through the combined DSM-MLM-DEM chain, melt pools and corresponding properties representative of a full-scale AM build can be simulated and used to inform future experiments in the context of AM product design.

4.5.1.1 Assumptions

The fabrication of an AM part involves the complex interaction of physics between a material and energy source, where accurately capturing the entirety of these interactions is infeasible with current computational methods. In this work, the DEM seeks to leverage the fast-acting DSM and account for missing physics which serve as a loss mechanism within the AM process, important for NiTi-based alloys due to Ni volatility and its evaporation during fabrication. Applying several assumptions, this workflow maintains a reduced computational cost ideal for screening PSPP trends within AM while accounting for material evaporation which prominently affects the composition and properties of AM NiTiHf alloys. These assumptions can then be categorized as the ones related to the prediction of evaporation flux and those corresponding to the calculation of final chemistry.

When evaluating the thermal processing which occurs during AM fabrication, it is assumed that the flow of molecules during evaporation events abides by The Kinetic Theory of Gases [111]. A formulation for the evaporation flux of a species i, j_i [g/cm^{2}s], is then derived as:

$$j_i = 44.331\bar{p}_i\left[\frac{M_i}{T}\right]^{\frac{1}{2}} \tag{4.6}$$

where $\bar{p}_i$ [atm] and M_i [g] represent the equilibrium vapor pressure and molecular weight of species i, respectively, and T [K] represents the absolute temperature. The calculation of evaporation flux within the DEM is further explained in Section 4.5.1.2.

When evaluating the effect of evaporation, it is also assumed that evaporation below the boiling temperature is negligible. This stems from the exponential increase in the vapor pressure and activity, α, of alloying elements with increasing temperature, resulting in the most significant evaporation at the boiling temperature [49]. For this purpose, it is assumed the melt pool surface can be described through the summation of multiple discretized isotherms where the surface area corresponding to each isotherm domain is defined by a uniform temperature. Additionally, for the case of NiTiHf, it is assumed that the amount of Hf, as well as the Ti/Hf mass ratio remains constant while Ni experiences the majority of evaporation within the system. This is due to the substantial volatility and content of Ni within the NiTiHf system relative to the other two alloying elements [49]. Furthermore, through these assumptions, a reduction in the number of calculations and the total computational cost is achieved for the sake of the efficient establishment of PSPP relationships toward AM product design.

After quantifying evaporation loss from the melt pool, the associated change in chemistry of the melt pool must also be accounted for. For this purpose, it is assumed that the melt pool can be defined as a mass balance problem of a control volume. This is accompanied by a formulation for the mass flow in, $\dot{m}^{in}$, the mass flow out, $\dot{m}^{out}$, and the mass loss due to evaporation from the system, $\dot{m}^{evap}$:

$$\dot{m}^{out} = \dot{m}^{in} - \dot{m}^{evap} \tag{4.7}$$

The mass balance and chemistry change is discussed further in Section 4.5.1.2. However, to make these calculations tractable, a secondary assumption is made. Here it is assumed that the flow of material within the melt pool allows for the complete mixing of the contained elements. Through this assumption, an average composition can be determined for a given melt pool and utilized within the model framework for the calculation of location-specific final chemistry as well as chemistry propagation throughout the component.

4.5.1.2 Chemistry Change

In order to calculate the chemistry change within a melt pool, the mass balance described by Equation 4.7 must be resolved. This begins with the deconstruction of the mass flow into and out of the meltpool for an alloying species i, $\dot{m}_i^{in}$ and $\dot{m}_i^{out}$, respectively, as:

$$\dot{m}_i^{in} = \rho^{in}\omega_i^{in} v A_{x-s}^{in} \tag{4.8}$$

$$\dot{m}_i^{out} = \rho^{out}\omega_i^{out} v A_{x-s}^{out} \tag{4.9}$$

where ρ $[kg/m^3]$ represents the density of the alloy, ω_i represents the weight fraction of the alloying species i, and v $[m/s]$ represents the flow velocity of the mass moving through the cross-sectional area of the melt pool, A_{x-s} $[m^2]$. The mass flow out of the melt pool due to evaporation for each alloying species i, m_i^{in}, must then be similarly deconstructed:

$$\dot{m}_i^{evap} = \sum_{iso=1}^{n} j_i\left(\chi_A, \chi_B, ..., T_{iso}\right) S_{iso} \tag{4.10}$$

where the evaporation rate for a species i, j_i, is dependent on both the chemistry of the alloying elements and an isotherm temperature, $(\chi_A, \chi_B, ...)$ and T_{iso}, respectively. This evaporation rate is multiplied with the corresponding surface area of the isotherm, S_{iso}. The meltpool surface can be discretized into multiple temperature isotherm bins, n, and summed to determine the total mass loss of the alloying species due to evaporation. However, due to the simplifying assumption of negligible evaporation below the boiling temperature, this equation is reduced to:

$$\dot{m}_i^{evap} = j_i\left(\chi_A, \chi_B, ..., T_{boil}\right) A_{boil} \tag{4.11}$$

The reader is referred to Ranaiefar et al. [14] for additional details on the mass balance in a control volume derivation. However, from Equations 4.7-4.11, a first-order solution to the problem, describing the mass flow due to each alloying species i through the melt pool, can be rewritten as:

$$\dot{m}_i^{out} = \rho^{in}\omega_i^{in} u A_{x-s}^{in} - j_i\left(\chi_A, \chi_B, ..., T_{boil}\right) A_{boil} \tag{4.12}$$

As part of this solution, further decomposition of variable components for evaporation flux, Equation 4.6, is required. The equilibrium vapor pressure for an alloying species i can be calculated through the product of standard vapor pressure and activity for the species i, p_i° $[atm]$ and α_i, respectively, as [66]:

$$\bar{p}_i = p_i^\circ a_i \tag{4.13}$$

It should be noted that activity values were generated through the Thermocalc 2020b TCHEA4 database and are not easily measured. For this reason, Ni activity, corresponding to the most volatile and prominent constituent of the NiTiHf system is subject to calibration in Section 4.5.4. Furthermore, the standard vapor pressure of a species i is determined through an empirical expression, derived from the Clausius-Clapeyron relation, dependent on temperature, T, and a set of species dependent Antoine coefficients, A_i, B_i, and C_i:

$$p_i^\circ = 10^{\left(A_i - \frac{B_i}{C_i + T}\right)} 760^{-1} \tag{4.14}$$

With Antoine coefficients corresponding to each alloying element of the NiTiHf system [49], defined in Table 4.3, a solution to mass loss and chemistry change in a melt pool due to evaporation can be determined. Based on the prior assumption of constant Hf content within the system, it should be noted that the evaporation flux of Hf is set to zero.

Table 4.3. Antoine coefficients for Ni, Ti, and Hf.

Element	A	B	C
Ni	8.75	17882.38	134.99
Ti	8.90	20948.99	190.76
Hf	9.06	30232.91	285.82

4.5.1.3 Nickel-Martensitic Transformation Temperature (M_s) Relationship

The binary NiTi SMA has been widely studied in literature, where current challenges include a lack of technologically advanced tools, with sufficient precision, for the chemical analysis and exact measurement of Ni content in these alloys [70, 113, 114]. Due to the addition of ternary Hf, measurement of Ni-content within the NiTiHf system is made further difficult [133, 154, 155]. Additionally, mapping the M_s-Ni relationship becomes more difficult in this case, as M_s is highly sensitive to both Ni and Hf content. However, as mentioned in Section 4.5.1.2, these SMAs can be treated the same as binary NiTi SMAs since it is assumed that only their Ni content changes during the fabrication process, due to the significantly greater volatility of this element, and that Hf content remains constant, due to its evaporation being negligible. Figure 4.8 illustrates the M_s-Ni relationship for the NiTiHf system with a constant Hf content, χ_{Hf}, of 20 at%.

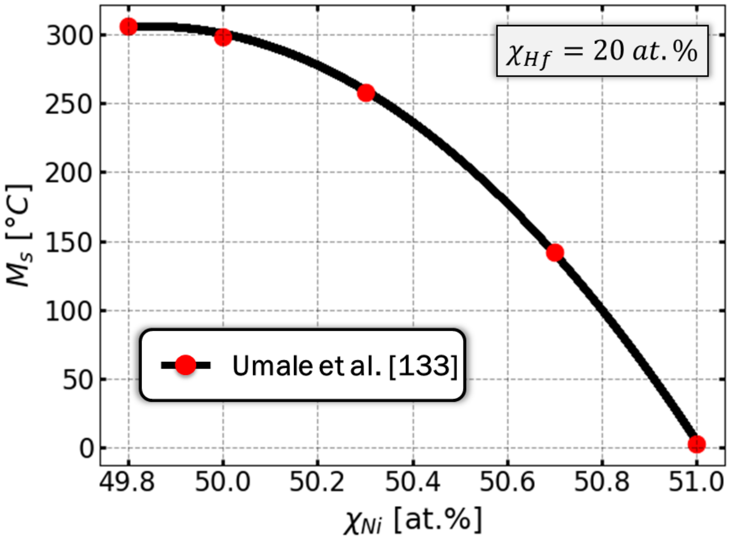

Fig. 4.8. Relationship between Ni content, χ_{Ni} [at%], and martensitic starting transformation temperature, M_s [°C].

It is shown that at Ni-rich content, a decrease in just 0.2 Ni at% can result in a ΔM_s of 100 °C. This strong negative trend of increasing M_s with decreasing Ni content eventually weakens as M_s

reaches an approximate peak of 306 °C at 49.8 Ni at%. Overall, this trend lends to reinforcing the extreme sensitivity of M_s with Ni content along with the importance and potential for utilizing this relationship to tailor location-specific properties of NiTiHf SMA components manufactured by LPBF. From DSC measured $\mathrm{Ni}_X\mathrm{Ti}_Y\mathrm{Hf}_{20}$ data [133], an empirical relation describing the M_s-Ni relationship can be developed:

$$M_s(\chi_{Ni}) = -225.834\chi_{Ni}^2 + 22513.431\chi_{Ni} - 560785.997 \tag{4.15}$$

This formulation is then used in the current study to link predicted location-specific Ni content to the martensite start transformation temperature property.

It should also be noted that although the as-recieved NiTiHf ingots used in this work had a reported Ni content of 50.3 at%, discussed in Section 4.3.2, the solutionized powder M_s value was measured as 101.9 °C through differential scanning calorimeter characterization. Based on Figure 4.8 and Equation 4.15, this M_s value is best characterized by a Ni content of 50.8 at%. Therefore, for the current work, model predictions for the NiTiHf system will utilize $\mathrm{Ni}_{50.8}\mathrm{Ti}_{29.2}\mathrm{Hf}_{20}$ as the initial powder composition.

4.5.2 Experimental Procedure

The 26 cuboid NiTiHf samples with size of 10 mm × 10 mm × 5 mm (building direction) were fabricated on NiTi substrates using DMP ProX 200 LPBF system under argon atmosphere. The oxygen level was kept below 100 ppm during the fabrication process to mitigate potential oxidation and associated performance degradation. Cell scanning strategy with cell size of 3 mm, overlap of 0.3 mm, and rotation of 67° between sequential layers was applied to reduce residual stress build-up. Within each cell, the normal back-and-forth laser paths were applied orthogonal to cell edges.

After printing, the cuboid NiTiHf samples were wire-EDM cut from the substrates for further characterization. A TA Instruments Q2000 differential scanning calorimeter (DSC) was used to measure the transformation temperatures of the fabricated samples. For each cuboid sample, the DSC specimen with 1 mm thickness and 3 mm diameter was cut from the middle of the cuboid sample and solution heat treated at 900 °C for 1 hour followed by water quenching before DSC characterization. Two thermal cycles from 25 to 400 °C were performed at the heating/cooling rate of 10 °C/min. The transformation temperatures were then obtained from the plots of the second cycles using the tangent method according to ASTM F2004-17. Table 4.4 contains the solution heat-treated (SHT) M_s data corresponding to laser power, laser speed, hatch spacing, linear energy density (LED), and volumetric energy density (VED) of 26 experiments with a constant layer thickness, L_t, of 41 μm.

Table 4.4. Process parameters and transformation temperatures after solution heat treatment for the 26 LPBF fabricated $\mathrm{Ni_{50.3}Ti_{29.7}Hf_{20}}$ cuboid specimens.

P [W]	v [mm/s]	h [μm]	LED [J/m]	VED [J/mm^3]	SHT $\mathrm{M_s}$ [°C]
80	330	40	242.4	147.8	305.8
100	455	40	219.8	134.0	297.8
100	600	75	166.7	54.2	201.8
100	600	40	166.7	101.6	215.2
100	600	30	166.7	135.5	300.9
100	600	26	166.7	156.3	325.5
100	600	20	166.7	203.3	309.9
100	800	87	125.0	35.0	191.2
100	800	60	125.0	50.8	198.0
100	800	40	125.0	76.2	256.2
100	800	30	125.0	101.6	262.7
100	800	25	125.0	122.0	316.1
100	800	20	125.0	152.4	305.3
100	800	15	125.0	203.3	308.9
100	800	12	125.0	254.1	313.6
120	830	35	144.6	100.8	212.4
120	830	25	144.6	141.1	274.6
120	830	18	144.6	196.0	304.9
120	1080	77	111.1	35.2	187.7
120	1080	50	111.1	54.2	194.4
120	1080	36	111.1	75.3	236.8
120	1080	27	111.1	100.4	286.0
120	1080	20	111.1	135.5	313.7
120	1080	13	111.1	208.5	314.9
120	1080	10	111.1	271.0	329.6
140	1080	25	129.7	126.5	251.1

4.5.3 Calibration Approach

Although the DSM is able to directly utilize MCMC sampling for Bayesian calibration due its low computational cost, the combined DSM-MLM-DEM chain has an added computational expense where the utilization of a surrogate model could offset the overall cost to run tens of thousands of simulations across the full model framework. In this section, a computationally cheap surrogate for the DSM-MLM-DEM chain is developed and applied towards the MCMC Bayesian calibration of the Ni activity parameter in the DEM, evaluating model predictions against experimental measurements for M_s. In this probabilistic calibration, the statistical model proposed by [141], deemed the Kennedy and O'Hagan (KOH) framework, is applied:

$$z_i = \rho\, \eta\left(\mathbf{x}_i, \boldsymbol{\theta}\right) + \delta(\mathbf{x}_i) + e_i \tag{4.16}$$

where ρ is a scaling parameter, $\mathbf{x}$ is control inputs, $\boldsymbol{\theta}$ is calibration parameters, $\eta(\cdot, \cdot)$ is the surrogate model output, $\delta(\cdot)$ is the model discrepancy term, z_i is the ith experimental observation and e_i is the ith observation error. $\eta(\cdot, \cdot)$, $\delta(\cdot)$, and z_i are assumed to be mutually independent.

Specifically, e_i is an independently distributed Gaussian noise with zero mean and a constant variance σ_ϵ^2, i.e., $e_i \sim \mathrm{N}(0, \sigma_\epsilon^2)$. $\eta(\cdot, \cdot)$ and $\delta(\cdot)$ follow Gaussian process distributions with different mean function and covariance function, i.e., $\eta(\cdot, \cdot) \sim \mathrm{GP}(m_1(\cdot, \cdot), c_1(\cdot, \cdot))$ and $\delta(\cdot) \sim \mathrm{GP}(m_2(\cdot), c_2(\cdot, \cdot))$. We adopt a linear form for the mean function, therefore $m_1(\mathbf{x}, \mathbf{t}) = \mathbf{h}_1(\mathbf{x}, \mathbf{t})^\intercal \beta_1$ and $m_2(\mathbf{x}) = \mathbf{h}_2(\mathbf{x})^\intercal \beta_2$. It is well known that selecting a well-fit covariance function (also called kernel) and choosing proper kernel hyperparameters (denoted as $\boldsymbol{\psi}$) are nontrivial jobs in GP modeling. The goal of calibration is to use simulation data $\mathbf{y}^\intercal$ and experimental observations $\mathbf{z}^\intercal$ to estimate linear estimates $\beta = (\beta_1^\intercal, \beta_2^\intercal)^\intercal$, system hyperparameters $\boldsymbol{\phi} = \{\rho, \boldsymbol{\psi}, \sigma_\epsilon^2\}$, and calibration parameters $\boldsymbol{\theta}$. These parameters should be independent of each other, so the prior distributions is:

$$p(\beta, \boldsymbol{\theta}, \boldsymbol{\phi}) = p(\beta) p(\boldsymbol{\theta}) p(\boldsymbol{\phi}) \tag{4.17}$$

For data $\mathbf{d} = (\mathbf{y}^\intercal, \mathbf{z}^\intercal)^\intercal$, its likelihood function is $p(\mathbf{d} | \boldsymbol{\theta}, \boldsymbol{\phi}, \beta)$. Using the Bayes' rule, we are able to obtain the posterior distribution:

$$p(\beta, \boldsymbol{\theta}, \boldsymbol{\phi} | \mathbf{d}) \propto p(\mathbf{d} | \beta, \boldsymbol{\theta}, \boldsymbol{\phi}) p(\beta) p(\boldsymbol{\theta}) p(\boldsymbol{\phi}) \tag{4.18}$$

In order to efficiently conduct calibration, we use the two-step strategy by [141] to estimate hyperparameters $\boldsymbol{\phi}$. The first step is to tune the surrogate model using simulation data, namely to estimate the hyperparameters $\boldsymbol{\psi}_1$ of $c_1(\cdot,\cdot)$; next, fix $\boldsymbol{\psi}_1$ and use data $\mathbf{d}$ to estimate $\{\rho, \boldsymbol{\psi}_2, \sigma_\epsilon^2\}$. Based on the distribution of MCMC samples, we take the posterior estimates in the form of the maximum posterior probability (MAP) estimates or posterior means. Conditional on the estimated parameters, the calibrated model $\mathbf{z}(\mathbf{x}_0)$ with input $\mathbf{x}_0$ is a Gaussian process, its mean and covariance functions are expressed as follows:

$$\mathbb{E}[\mathbf{z}(\mathbf{x}_0)|\mathbf{d}, \boldsymbol{\theta}, \boldsymbol{\phi}] = \mathbf{h}(\mathbf{x}_0, \boldsymbol{\theta})^\top \hat{\beta}(\boldsymbol{\theta}) + \mathbf{t}(\mathbf{x}_0, \boldsymbol{\theta})^\top \boldsymbol{\Sigma}(\boldsymbol{\theta})^{-1}(\mathbf{d} - \mathbf{H}(\boldsymbol{\theta})\hat{\beta}(\boldsymbol{\theta})) \tag{4.19}$$

$$\begin{aligned}\mathbb{COV}[\mathbf{z}(\mathbf{x}_0)|\mathbf{d}, \boldsymbol{\theta}, \boldsymbol{\phi}] = {} & \rho^2\, c_1((\mathbf{x}_0, \boldsymbol{\theta}), (\mathbf{x}_0, \boldsymbol{\theta})) + c_2(\mathbf{x}_0, \mathbf{x}_0) - \mathbf{t}(\mathbf{x}_0, \boldsymbol{\theta})^\top \boldsymbol{\Sigma}(\boldsymbol{\theta})^{-1} \mathbf{t}(\mathbf{x}_0, \boldsymbol{\theta}) \\ & + (\mathbf{h}(\mathbf{x}_0, \boldsymbol{\theta}) - \mathbf{H}(\boldsymbol{\theta})^\top \boldsymbol{\Sigma}(\boldsymbol{\theta})^{-1} \mathbf{t}(\mathbf{x}_0, \boldsymbol{\theta}))^\top \mathbf{W}(\boldsymbol{\theta})(\mathbf{h}(\mathbf{x}_0, \boldsymbol{\theta}) \\ & - \mathbf{H}(\boldsymbol{\theta})^\top \boldsymbol{\Sigma}(\boldsymbol{\theta})^{-1} \mathbf{t}(\mathbf{x}_0, \boldsymbol{\theta}))\end{aligned} \tag{4.20}$$

where

$$\begin{aligned}\mathbf{h}(\mathbf{x}_0, \boldsymbol{\theta}) &= [\rho\, \mathbf{h}_1(\mathbf{x}_0, \boldsymbol{\theta}) \quad \mathbf{h}_2(\mathbf{x}_0)]^\top \\ \mathbf{t}(\mathbf{x}_0, \boldsymbol{\theta}) &= [\rho\, c_1((\mathbf{x}_0, \boldsymbol{\theta}), D_1) \quad \rho^2\, c_1((\mathbf{x}_0, \boldsymbol{\theta}), D_2(\boldsymbol{\theta})) + c_2(\mathbf{x}_0, D_2)]^\top \\ \mathbf{H}(\boldsymbol{\theta}) &= \begin{bmatrix} \mathbf{H}_1(D_1) & \mathbf{0} \\ \rho\, \mathbf{H}_1(D_2(\boldsymbol{\theta})) & \mathbf{H}_2(D_2) \end{bmatrix} \\ \boldsymbol{\Sigma} &= \begin{bmatrix} c_1(D_1, D_1) & \rho\, c_1(D_1, D_2(\boldsymbol{\theta})) \\ \rho\, c_1(D_2(\boldsymbol{\theta}), D_1) & \sigma_\epsilon^2 \mathbf{I} + \rho^2\, c_1(D_2(\boldsymbol{\theta}), D_2(\boldsymbol{\theta})) + c_2(D_2, D_2) \end{bmatrix} \\ \mathbf{W} &= (\mathbf{H}(\boldsymbol{\theta})^\top \boldsymbol{\Sigma}(\boldsymbol{\theta})^{-1} \mathbf{H}(\boldsymbol{\theta}))^{-1}\end{aligned}$$

D_1 is the inputs of simulation data $\mathbf{y}^\top$, containing control inputs and calibration inputs; D_2 is the control inputs of experimental measurements $\mathbf{z}^\top$; $D_2(\boldsymbol{\theta})$ combines D_2 with the estimates of calibration parameters. $\mathbf{H}_i(D_j)$ is the matrix form of $\mathbf{h}_i^\top$ on D_j, for example, the ith row of $\mathbf{H}_2(D_2)$ takes the form of $\mathbf{h}_2(\mathbf{x}_i)^\top$.

4.5.4 Calibration Results

The proposed differential evaporation model takes power P, velocity, υ, and hatch spacing, h, as control inputs, i.e., $\mathbf{x} = \{P, \upsilon, h\}$ and Ni activity as the calibration parameter, i.e., $\boldsymbol{\theta} = \{a_{Ni}\}$. The prediction of the model is the martensite start transformation temperature, denoted as M_s. For surrogate model development, 556 data points were generated uniformly over the parameter space $X \times \Theta$, bounded by experiment conditions, using Latin Hypercube Sampling.

Before modeling, the mean and covariance functions of the GP models should be specified. We take $\mathbf{h}_1(\mathbf{x}, \mathbf{t}) = \mathbf{h}_2(\mathbf{x}) = (1)$; for surrogate model we adopt the Matérn kernel (ν=3/2), with hyperparameters $\boldsymbol{\psi}_1 = \{\sigma_s^2, \ell_s\}$; for discrepancy model we define its covariance function with hyperparameters $\boldsymbol{\psi}_2 = \{\sigma_{\delta_1}^2, \sigma_{\delta_2}^2, \sigma_{\delta_3}^2, \ell_1, \ell_2, \ell_3\}$:

$$c_2(\mathbf{x}, \mathbf{x}') = \sigma_{\delta_1}^2 \prod_{i=1}^{3} \exp\Big(-\frac{(\mathbf{x}_i - \mathbf{x}_i')^2}{2\ell_i^2}\Big) + \sigma_{\delta_2}^2 \mathbf{x}\mathbf{x}'^{\intercal} + \sigma_{\delta_3}^2 \tag{4.21}$$

As explained in Section 4.5.3, the first step is training the surrogate model. A zero mean GP model with the Matérn kernel (ν=3/2) was trained on 556 simulation data using the $GaussianProcessRegressor$ function through the Python scikit-learn package by [156], outputting hyperparameters $\boldsymbol{\psi}_1 = \{0.656, 0.327\}$.

For remaining hyperparamters $\{\rho, \boldsymbol{\psi}_2, \sigma_\epsilon^2\}$, coefficient β_2 and calibration parameter θ, MCMC is used for generating samples. The prior distributions are set as follows:

$$a_{Ni} \sim \mathrm{Uniform}(0.15, 0.4)$$

$$\beta_2 \sim \mathrm{Normal}(\mu = 0, \sigma^2 = 1/4)$$

$$\sigma_{\delta_1}^2 \sim \text{Inverse-Gamma}(\alpha = 2, \beta = 1)$$

$$\sigma_{\delta_2}^2,\ \sigma_\epsilon^2 \sim \text{Inverse-Gamma}(\alpha = 2, \beta = 0.2)$$

$$\sigma_{\delta_3}^2, \rho \sim \text{Log-Normal}(\mu = 0, \sigma^2 = 1/4)$$

$$\ell_i \sim \text{Log-Normal}(\mu = 0, \sigma^2 = 1/4),\ i = 1, 2, 3$$

From the 26 cuboid experiment parameter sets, 20 were randomly selected as training data and the remaining 6 points were used as test data. MCMC was run in Python using PyMC3 [157]. Two chains of samples, with the sample size of 30,000 and tuning size of 10,000, were generated. We took the posterior mean of a_{Ni} as the posterior estimate, i.e., $\theta^* = 0.275$. For the hyperparmeter $\phi = \{\rho, \{\sigma^2_{\delta_1}, \sigma^2_{\delta_2}, \sigma^2_{\delta_3}, \ell_1, \ell_2, \ell_3\}, \sigma^2_\epsilon\}$, $\boldsymbol{\phi}^*_{MAP} = \{0.599, \{0.298, 0.118, 0.732, 0.866, 0.849, 0.836\}, 0.313\}$ and coefficients MAP estimates are $\hat{\beta} = [0, 0.100]^\intercal$.

According to Equation 4.19, M_s for the test points can now be predicted. Table 4.5 contains performance metrics of model predictions against experimental measurements, for the 6 test data points, in terms of the root mean squared error (RMSE) and mean absolute percentage error (MAPE) for both the surrogate and calibrated model. Upon evaluation, the calibrated model achieved an RMSE and MAPE value of 11.3 °C and 3.4%, respectively, in contrast to the surrogate model's RMSE of 20.5 °C and MAPE of 7.6%. These results make evident the effective improvement in the predictive power of the model resulting from Bayesian calibration.

Furthermore, through uncertainty quantification of the calibrated model parameter, Ni activity, increased comprehension of the model framework's utility for the purpose of robust design can be ascertained. Figure 4.9 illustrates the propagated uncertainty through the multi-model framework for each of the 26 LPBF NiTiHf parameter sets, stemming from MCMC samples generated through the calibration of the DEM. In this case, the last 500 samples for the Ni activity parameter selected from each of the two MCMC sample chains (generated from two different initial parameter values) are combined and used as model input, after which the top and bottom 2.5% output values, i.e., M_s, are removed for each experimental condition to provide a 95% CI. Through this uncertainty quantification, experimental measurements are shown to fall within the 95% CIs of model predic-

Table 4.5. Performance metrics for the surrogate prediction and calibrated prediction on the 6 test data points. RMSE - root mean square error; MAPE - mean absolute percentage error

Model	RMSE [°C]	MAPE [%]
Surrogate	20.5	7.6
Calibrated	11.3	3.4

tions, with the exception of three cases. In Section 4.6, the total model uncertainty and 95% CIs are determined and compared with experiments to provide a complete and more robust measure of the model framework's utility for AM design.

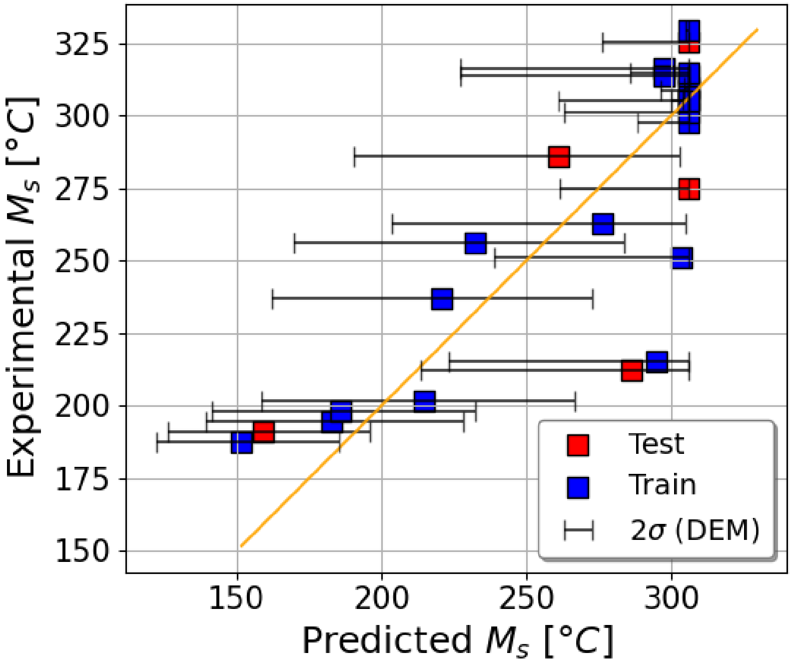

Fig. 4.9. Uncertainty Propagation with 95% credible intervals for model predictions of M_s compared with empirical values for LPBF $Ni_{50.3}Ti_{29.7}Hf_{20}$ samples. Here, uncertainty propagation is from the DEM only.

4.6 Model Validation and Discussion

Through the calibrated ICME framework, M_s properties were predicted and validated with the 26 LPBF NiTiHf cuboids discussed in Section 4.5.2 Table 4.4. The model framework input parameters and thermophysical properties are listed in Table 4.6.

Figure 4.10 provides a comparison of model predictions for M_s and DSC measurements from experiments. The root mean square error (RMSE) and mean absolute percentage error (MAPE) for the 26 samples is 28.9 °C and 8.2%, respectively, representing a good measure of predictive

Table 4.6. Model input parameters and thermophysical properties for the 26 LPBF NiTiHf experiments.

P [W]	v [mm/s]	h [μ m]	L_t [μ m]	η	κ [W/m K]	C_p [J/kg K]	C	σ [μ m]	ρ [kg/m^3]	T_0 [°C]
80 - 140	330 - 1080	10 - 87	41	0.64	13.2	652.5	0.81	20	8893	25

accuracy for the model when compared with experiments. Furthermore, the Pearson correlation, ρ_{M_s}, of 0.83 indicates a strong positive linear correlation between predicted and measured M_s. The strength of these predictions is further reinforced when considering the uncertainty of standard chemistry measurement techniques such as wavelength dispersive spectroscopy (WDS) and inductively coupled plasma atomic emission spectroscopy (ICP-AES), ± 0.5 at%. Additionally, for the measurement of major constituents, ICP-AES uncertainty has been reported to be as large as ± 2% of the absolute value [115]. Converting Ni content measured through these techniques to M_s could then result in an uncertainty of ± 75 °C. This demonstrates the model framework's capability to accurately and efficiently predict M_s property values from processing parameters, performing well within the range of uncertainty for chemistry measurement techniques.

Equally important in understanding the utility of the model framework for the purpose of robust design, uncertainty quantification through the uncertainty propagation of calibrated model parameters has been conducted. Figure 4.11 illustrates the propagated uncertainty through the model framework for each of the 26 LPBF NiTiHf conditions, stemming from MCMC samples generated through the calibration of both the DSM and the DEM. In this case, the last 1000 MCMC samples from the DSM calibration and the same 1000 samples from the prior DEM uncertainty propagation, Section 4.5.4, are combined and used as model input. The top and bottom 2.5% output values are then removed to provide 95% CIs for model predictions based on the uncertainty propagation across the entire model framework.

When comparing uncertainty from the DEM alone to the complete framework uncertainty, an increase in the range of the 95% CI is observed. This is expected due to the consideration of increased uncertainty stemming from the DSM. It should be noted that the peak M_s set by

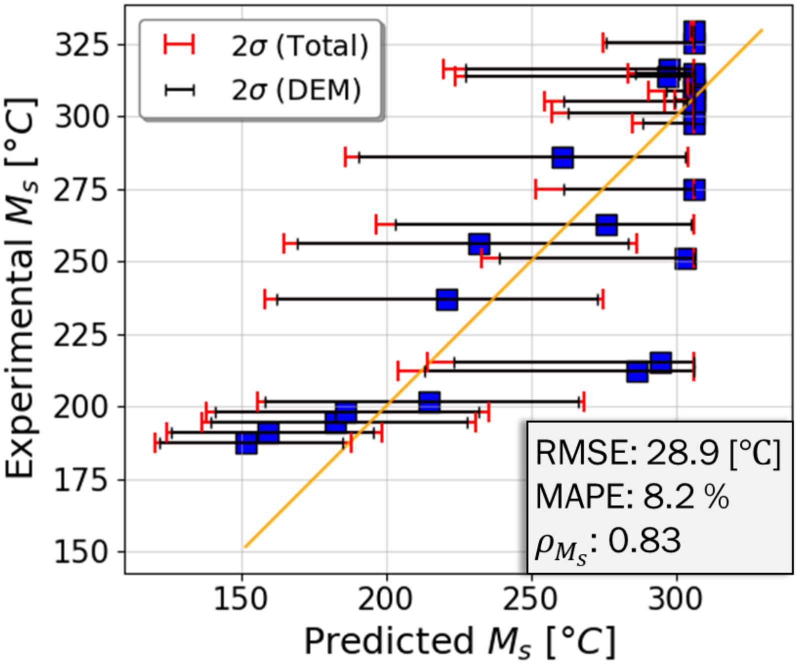

Fig. 4.10. Model predictions of M_s with their 95% CIs compared with empirical values for LPBF $Ni_{50.3}Ti_{29.7}Hf_{20}$ samples, resulting from DEM uncertainty propagation only and uncertainty propagation for all components of the ICME framework.

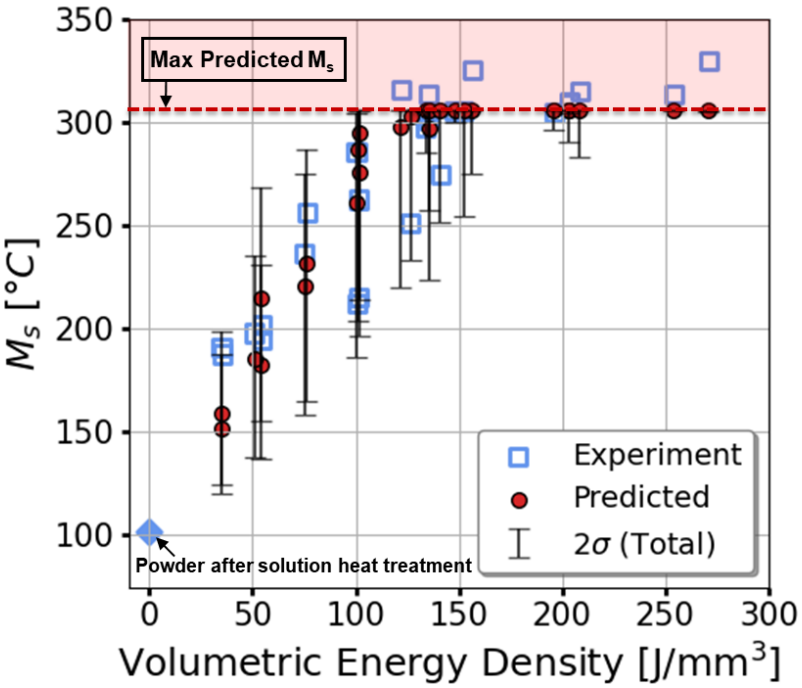

Fig. 4.11. Model predictions of M_s with their 95% CIs in terms of VED for LPBF $Ni_{50.3}Ti_{29.7}Hf_{20}$ samples, resulting from uncertainty propagation for all components of the ICME framework.

Equation 4.15 results in uncertainty bounds which do not capture M_s values exceeding 306 °C, although the model predictions still follow experimental trends. This is observed for higher VED cases, where increased Ni evaporation and M_s values are expected, and can be resolved through additional experiments to refine the empirical Ni-M_s relationship. Furthermore, with experimental measurements falling within the 95% confidence interval of model predictions, the calibrated ICME framework demonstrates its utility and potential to guide and inform experiments in the context of robust design.

In materials design, process maps have also been constructed to further accelerate and expedite development by providing valuable insight into PSPP trends of alloy system. Figure 4.12 illustrates process maps for the additively manufactured $Ni_{50.3}Ti_{29.2}Hf_{20}$ system by LPBF with an incremental hatch spacing of 30 μm, 60 μm, and 90 μm, from which several observations can be made:

- First, for all hatch space values, there is an increase in M_s with increasing power and velocity, corresponding to the keyholing print region. This culminates in a Ni-M_s insensitive region where additional Ni loss does not increase M_s beyond 306 °C. Conversely, as power and velocity decrease, there is a corresponding decrease in M_s. A region with M_s of approximately 101.9 °C, corresponding to the M_s of the initial powder composition, is also observed once power and velocity combinations are low enough. This region is a result of the assumption which states that evaporation is negligible below the boiling temperature, where although these specific combinations of laser power and laser velocity could result in temperatures exceeding the melting point of the alloy system, this does not result in the evaporation of Ni from the melt pool or a change in M_s from the initial composition.
- Second, as the hatch spacing increases, the process region corresponding to the peak M_s is shown to diminish. This trend aligns with expectations that increasing hatch spacing results in the reduced magnitude of thermal events during the AM process, resulting in less evaporation, higher Ni content, and lower M_s than process parameters with lower hatch spacing and the same power and velocity values.

- Third, as the hatch spacing increases, the processing window to achieve a specific range of M_s increases. This translates to an increased tailorability of M_s for the design of components when utilizing larger hatch space values, in contrast to an increased sensitivity of M_s with power and velocity at smaller hatch space values. If a larger hatch spacing can be used in combination with multiple layer scans, a dramatic increase in the robustness of tailored location-specific properties can be achieved. When combined with printability maps depicting the relationship between process parameters and print quality (good, keyholing, balling, lack of fusion), the design space can be further constrained for the accelerated development and cost-effective design of defect-free components with location-specific properties [134, 158].

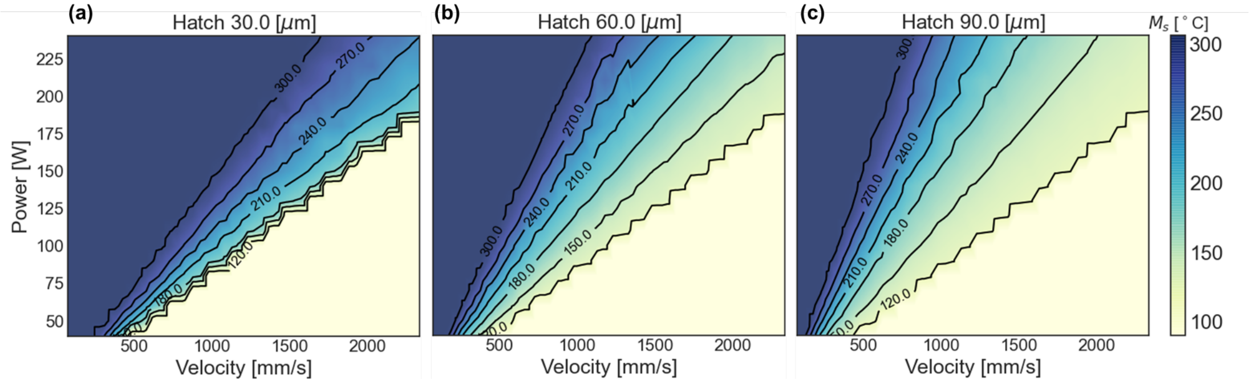

Fig. 4.12. Process maps for $Ni_{50.3}Ti_{29.7}Hf_{20}$ SMAs manufactured by LPBF as predicted by the calibrated ICME framework for several hatch spacing values: (a) 30 μm, (b) 60 μm, (c) 90 μm. Laser velocity and laser power bounds are also selected based on experimental conditions

4.7 Summary and Conclusion

The complex physics of AM processes give rise to numerous challenges in material development and design. Not only is it necessary to accurately resolve the forward modeling problem of linking process parameters to properties for accelerated development, but a measure of confidence in model predictions is required for robust design. The forward model framework can then be leveraged for the inverse design of AM components with tailored location-specific properties. In this study, a fast-acting ICME framework was developed to predict location-specific properties based on process parameters for $\mathrm{Ni_{50.3}Ti_{29.7}Hf_{20}}$ SMAs manufactured by LPBF. Model components were calibrated and the framework validated with experiments, demonstrating good agreement between model predictions and experimentally measured M_s with an RMSE of 28.9 °C, a MAPE of 8.2%, and a Pearson correlation of 0.83. Furthermore, the viability of this modeling framework as a tool to inform and guide experiments for accelerated and robust design is supported by the 95% CIs determined through uncertainty quantification. In this regard, after accounting for the limitation on peak M_s value as determined through the empirical Ni-M_s relationship, 100% of the measured SHT M_s values for the $\mathrm{Ni_{50.3}Ti_{29.7}Hf_{20}}$ cuboid specimens fell within the 2σ or 95% CIs of the framework predictions. Model predictions for measurements which exceeded the peak M_s could be improved upon through an improved empirical Ni-M_s relationship, however predictions are still within 20 °C of measurements and align with expected Ni-M_s trends. Additionally, the total framework uncertainty of predicted values fall within a tighter window than the uncertainty of standard chemistry measurement techniques such as WDS and ICP-AES. With confidence through validation and uncertainty quantification, the ICME framework is then leveraged to develop process maps providing further insight into PSPP relationships across design space and to aid in cost-effective material development. M_s trends as a function of hatch spacing indicate an increased robustness of the design space with increased hath spacing. This can be exploited for the fabrication of tailored AM components with location-specific properties by leveraging printability maps in combination with multiple remelts of a single-layer to reduce the design space and maintain the larger M_s processing window provided by an increased hatch spacing.

5. SUMMARY AND FUTURE WORK

5.1 Summary

Additive manufacturing (AM) has enabled the rapid fabrication of complex and fit-for purpose components impossible through prior manufacturing methods. Not only has AM removed limitations on the materials design space through geometric freedoms and the ability to tailor location-specific properties, but AM has lifted the ceiling on the achievable performance of components across multiple industries. NiTi-based shape memory alloys (SMAs) are primed to benefit from these qualities which AM provides, and the current work has sought to develop a physics-based and data-driven integrated computational materials engineering framework (ICME) to accelerate the development of laser powder bed fusion (LPBF) AM NiTi-based components by accounting for a mechanism inherent to additive manufacturing, differential evaporation, and by formulating a connection between the system's complex process-structure-property-performance (PSPP) relationship.

As an initial step, a multi-model system consisting of a thermal model (DSM), a multi-layer model (MLM), and a differential evaporation model (DEM) was developed to screen PSPP trends and to guide experiments for the accelerated design of LPBF AM NiTi. By utilizing thermal histories predicted by the DSM, melt pool geometries can be calculated. These melt pool width and depth values were then used to calibrate the model with single track experiments for several parameters including efficiency, heat capacity, thermal conductivity, and a depth correction factor. With a calibrated thermal model, melt pool geometries corresponding to cuboid experiments were calculated and fed to the MLM, accounting for melt pool overlap and chemistry propagation across all simulated tracks and layers of the component. Working in concert, the DEM accounts for evaporation losses and corresponding changes in chemistry for each melt pool. This framework is used in conjuntion with a semi-analytical Ni-Martensite starting transformation temperature, M_s, relationship to complete the PSPP network and provide a solution to the forward design problem.

The ICME framework was validated against the cuboid $Ni_{50.8}Ti_{49.2}$ experiments and demonstrated Ni content and M_s predictions in agreement with experimental measurements and trends, and within the uncertainty of traditional chemistry measurement techniques.

With a solution to the forward design problem, the framework is now leveraged to tackle the inverse design of LPBF AM $Ni_{51.2}Ti_{48.8}$ SMAs. A surrogate model was constructed for the design parameters of laser power, laser speed, and hatch spacing, based on experimental design parameters from prior $Ni_{50.8}Ti_{49.2}$ experiments as well as the limitations of the 3D printer. A global sensitivity analysis of the surrogate model across these design parameters was conducted and provided sensitivity indices for model output variance for each of the parameters. Although laser velocity corresponded to the largest sensitivity, hatch spacing displayed a value much lower than expected. A similar observation is made for laser power. This is potentially due to the parameter ranges used in the sensitivity analysis, and can be adjusted for in the future. Additionally, a global sensitivity analysis was conducted across the full model framework for 10 model input parameters. Of these parameters, efficiency, heat capacity, thermal conductivity, and Ni activity demonstrated some of the strongest total-order sensitivity indices and emphasize the importance for calibrating these parameters within the model framework.

Following this, the surrogate model is treated as a black-box and a multi-objective optimize scheme leveraged to solve the inverse design problem. Both a gradient based sequential least squares quadratic programming (SLSQP) and a heuristic genetic evolution based differential evolution approach were tested and proven successful in determining an optimal feasible solution for the main objective function of targeting a desired M_s and the secondary objective function of increasing the fabrication rate. Although successful, additional considerations for reducing the design space by considering the printability corresponding to design parameter combinations should be made.

Furthermore, the utility of the ICME framework was expanded from the binary NiTi system by enabling M_s predictions and the screening of PSPP trends for the ternary $Ni_{50.8}Ti_{29.2}Hf_{20}$ system. This system added complexities to design problem and Ni-M_s relationship due to the addition of Hf, however after calibration of the DSM for efficiency, thermal conductivity, and heat capacity, and calibration of the DEM for Ni activity, validation of the ICME framework demonstrated good agreement between model predictions and experimental measurements for M_s. This was accompanied by a study of uncertainty quantification and uncertainty propagation through the multi-model system to demonstrate the robustness of the ICME framework in the context of design. Setting a benchmark of 2σ, the 95% credible interval for each of the 26 model predictions captured their corresponding experimental measurement for M_s. Additionally, the development of process maps provided insight into PSPP trends for M_s across the laser power, laser velocity, and hatch spacing design space. Through this analysis it is demonstrated that model framework are robust and can be reliably applied towards the tailored design of LPBF AM NiTiHf components.

5.2 Future Work

Although the ICME framework has been successfully tested for the design and development of NiTi and NiTiHf systems, additional steps can be taken to improve and expand its capabilities. One of these tasks include the application of a Bayesian optimization approach towards the resolution of the inverse design problem. In this effort, a probabilistic approach will be taken to more efficiently provide an optimal feasible solution for target specifications. This would also enable the use of the full ICME framework rather than a surrogate model in determining appropriate design solutions. Additionally, an effort to reduce the design space to processing conditions which provide good quality defect-free prints should be made. Figure 5.1 illustrates a sample printability map providing insight on processing conditions and associated regimes of print quality for keyholing, balling, and lack of fusion defects as well as good quality prints [144]. This tool can be leveraged in conjunction with the ICME framework to more effectively and efficiently provide feasible optimal solutions by adding constraints and narrowing the design window for the inverse design problem.

Furthermore, printability maps can be used as an overlay with process-maps to provide additional insight into PSPP relationships while considering the feasibility in the context of design. Figure 5.2 illustrates this printability-process map overlay for LPBF AM $Ni_{50.3}Ti_{49.7}$, $Ni_{50.8}Ti_{49.2}$, and $Ni_{51.2}Ti_{48.8}$ M_s at a constant hatch spacing of 80 μm across a range of power and velocity combinations. Similar PSPP trends are seen as previously discussed, however the boundaries for

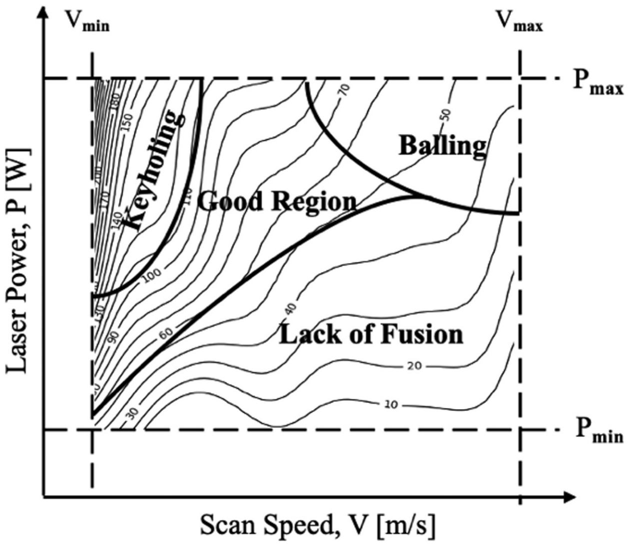

Fig. 5.1. Generic printability map for a range of laser power and velocity combinations. Boundaries corresponding to processing regions for good print quality, keyholing, lack of fusion, and balling defects are provided. Reproduced with permission from [144].

good print quality, keyholing, balling, and lack of fusion provide additional insight into the design window and corresponding M_s which can be tailored for while maintaining good quality prints.

By starting off with $Ni_{51.2}Ti_{48.8}$, it can be observed that a larger range of M_s can be attained within processing window for good quality, whereas this M_s range is reduced as the Ni content within the initial powder is reduced, such as with $Ni_{50.3}Ti_{49.7}$. This is due to an increased Ni-M_s insensitivity as Ni approaches 49.8 at%. Based on these results, there is larger window of opportunity for the tailored design of location-specific properties for LPBF AM NiTi components if a larger concentration of Ni comprises the NiTi system. Multiple remelts of a location or layer could then be used to further modulate location-specific properties while maintaining design variables within the good print quality design window. The continued development of these maps could provide actionable insight and influence decision making for optimal design parameters in the design process, and should be repeated for the NiTiHf system as well as additional combinations of design parameters and new material systems as available.

As the need for specialized components increases, there is likely an accompanying increase in complexity and challenges for its fabrication. Functionally graded materials (FGMs) are one

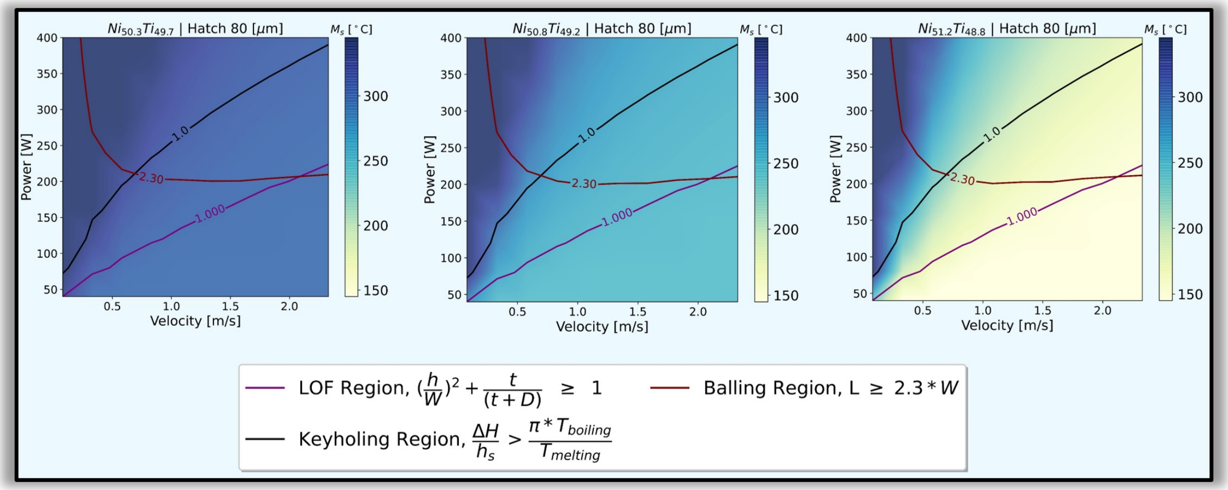

Fig. 5.2. Process maps overlaid with printability maps for LPBF AM $Ni_{50.3}Ti_{49.7}$, $Ni_{50.3}Ti_{49.7}$, and $Ni_{50.3}Ti_{49.7}$ M_s at a constant hatch spacing of 80 μm across a range of power and velocity combinations. Criteria and boundaries for lack of fusion (LOF), balling, and keyholing regions are included. as predicted by the calibrated ICME framework for several hatch space values: (a) 30 μm, (b) 60 μm, (c) 90 μm. Laser velocity and laser power bounds are also based on experiment parameters.

such example, where composition, microstructure, and properties are gradually changed as the part is being printed. In NiTi-based alloys, processing conditions can be modulated throughout the print process to exploit PSPP trends by altering input energy and the consequential Ni content and corresponding M_s. The ICME framework can be utilized in this regard to enable the accelerated design of functionally graded LPBF AM NiTi-based SMAs. Although the framework can readily account for multiples zones of different processing conditions, the complex scan strategies required by experiments for successful fabrication are not readily captured by the MLM. Melt pool overlap and chemistry propagation resulting from a conventional scan strategy is relatively straightforward and consistent compared to the geometric and overlap consideration that are required with diagonal and rotational scan strategies. However, properly accounting for melt pool overlap and chemistry propagation across more complex scan strategies would enable the improved accuracy of simulations with respect to experiments and the expanding utility of the framework across a wider variety of material design scenarios.

Another application of the framework towards the development of FGMs involves utilizing differential evaporation to assist in difficult material path planning efforts and avoid the formation of undesirable phases. In high-dimensional alloy systems, avoidance may be impossible or require absolute precision and control over the printing path [159, 160]. A major factor that compromises the controllability of compositions deposited is differential evaporation. This can be remedied by considering differential evaporation and predicted chemistry changes during AM. Integrating the DEM with a path planning algorithm [160] would provide the means to predict chemistry changes from uncontrolled evaporation and to correct for them as an FGM path is being defined. This will enhance path planning capabilities and the ability to successfully print a higher order of FGMs.

REFERENCES

[1] W. E. Frazier, "Metal additive manufacturing: a review," *Journal of Materials Engineering and Performance*, vol. 23, no. 6, pp. 1917–1928, 2014.

[2] J. O. Milewski, *Additive Manufacturing of Metals : From Fundamental Technology to Rocket Nozzles, Medical Implants, and Custom Jewelry*. Cham, SWITZERLAND: Springer International Publishing, 2017.

[3] T. Mukherjee, J. Zuback, A. De, and T. DebRoy, "Printability of alloys for additive manufacturing," *Scientific reports*, vol. 6, 2016.

[4] A. Vafadar, F. Guzzomi, A. Rassau, and K. Hayward, "Advances in metal additive manufacturing: a review of common processes, industrial applications, and current challenges," *Applied Sciences*, vol. 11, no. 3, p. 1213, 2021.

[5] W. J. Sames, F. A. List, S. Pannala, R. R. Dehoff, and S. S. Babu, "The metallurgy and processing science of metal additive manufacturing," *International Materials Reviews*, vol. 61, no. 5, pp. 315–360, 2016.

[6] T. DebRoy, H. L. Wei, J. S. Zuback, T. Mukherjee, J. W. Elmer, J. O. Milewski, A. M. Beese, A. Wilson-Heid, A. De, and W. Zhang, "Additive manufacturing of metallic components – process, structure and properties," *Progress in Materials Science*, vol. 92, no. Supplement C, pp. 112–224, 2018.

[7] D. Moon and E. Metzbower, "Laser beam welding of aluminum alloy 5456," *Welding Journal*, vol. 62, no. 2, pp. 535–585, 1983.

[8] A. Yadollahi and N. Shamsaei, "Additive manufacturing of fatigue resistant materials: Challenges and opportunities," *International Journal of Fatigue*, vol. 98, pp. 14–31, 2017.

[9] M. Yakout, A. Cadamuro, M. A. Elbestawi, and S. C. Veldhuis, "The selection of process parameters in additive manufacturing for aerospace alloys," *The International Journal of Advanced Manufacturing Technology*, vol. 92, no. 5, pp. 2081–2098, 2017.

[10] A. El-Batahgy and M. Kutsuna, "Laser beam welding of aa5052, aa5083, and aa6061

aluminum alloys," *Advances in Materials Science and Engineering*, vol. 2009, 2009.

[11] M. J. Cieslak and P. W. Fuerschbach, "On the weldability, composition, and hardness of pulsed and continuous nd:yag laser welds in aluminum alloys 6061,5456, and 5086," *Metallurgical Transactions B*, vol. 19, no. 2, pp. 319–329, 1988.

[12] M. M. Collur, A. Paul, and T. Debroy, "Mechanism of alloying element vaporization during laser welding," *Metallurgical Transactions B*, vol. 18, no. 4, pp. 733–740, 1987.

[13] S. Marimuthu, D. Clark, J. Allen, A. Kamara, P. Mativenga, L. Li, and R. Scudamore, "Finite element modelling of substrate thermal distortion in direct laser additive manufacture of an aero-engine component," *Proceedings of the Institution of Mechanical Engineers, Part C: Journal of Mechanical Engineering Science*, vol. 227, no. 9, pp. 1987–1999, 2013.

[14] M. Ranaiefar, P. Honarmandi, L. Xue, C. Zhang, A. Elwany, I. Karaman, E. Schwalbach, and R. Arroyave, "A differential evaporation model to predict chemistry change of additively manufactured metals," *Available at SSRN 3813432*, 2021.

[15] X. He, T. DebRoy, and P. W. Fuerschbach, "Alloying element vaporization during laser spot welding of stainless steel," *Journal of Physics D: Applied Physics*, vol. 36, no. 23, p. 3079, 2003.

[16] D. L. Reger, S. R. Goode, and D. W. Ball, *Chemistry: principles and practice*. Cengage Learning, 2009.

[17] K. Mundra and T. DebRoy, "Toward understanding alloying element vaporization during laser beam welding of stainless steel," *WELDING JOURNAL-NEW YORK-*, vol. 72, pp. 1–s, 1993.

[18] S. L. Semiatin, V. G. Ivanchenko, and O. M. Ivasishin, "Diffusion models for evaporation losses during electron-beam melting of alpha/beta-titanium alloys," *Metallurgical and Materials Transactions B*, vol. 35, no. 2, pp. 235–245, 2004.

[19] M. J. Matthews, G. Guss, S. A. Khairallah, A. M. Rubenchik, P. J. Depond, and W. E. King, "Denudation of metal powder layers in laser powder bed fusion processes," *Acta Materialia*, vol. 114, pp. 33–42, 2016.

[20] X. He, T. DebRoy, and P. W. Fuerschbach, "Composition change of stainless steel during microjoining with short laser pulse," *Journal of Applied Physics*, vol. 96, no. 8, pp. 4547–4555, 2004.

[21] H. Zhao and T. Debroy, "Weld metal composition change during conduction mode laser welding of aluminum alloy 5182," *Metallurgical and Materials Transactions B*, vol. 32, no. 1, pp. 163–172, 2001.

[22] K. Mundra and T. Debroy, "Calculation of weld metal composition change in high-power conduction mode carbon dioxide laser-welded stainless steels," *Metallurgical Transactions B*, vol. 24, no. 1, pp. 145–155, 1993.

[23] P. Khan, T. DebRoy, and S. David, "Laser beam welding of high-manganese stainless steels—examination of alloying element loss and microstructural changes," *Welding Journal*, vol. 67, pp. 1s–7s, 1988.

[24] R. C. Barclay, *Parameter optimization for controlling aluminum loss when laser depositing Ti-6Al-4V.* Missouri University of Science and Technology, 2013.

[25] M. Jandaghi, P. Parvin, M. Torkamany, and J. Sabbaghzadeh, "Alloying element losses in pulsed nd: Yag laser welding of stainless steel 316," *Journal of Physics D: Applied Physics*, vol. 41, no. 23, p. 235503, 2008.

[26] J. Moore and C. Stanitski, *Chemistry: The Molecular Science.* Cengage Learning, 2014.

[27] T. DebRoy and S. A. David, "Physical processes in fusion welding," *Reviews of Modern Physics*, vol. 67, no. 1, pp. 85–112, 1995.

[28] C. H. Fu and Y. B. Guo, "Three-dimensional temperature gradient mechanism in selective laser melting of ti-6al-4v," *Journal of Manufacturing Science and Engineering*, vol. 136, no. 6, pp. 061004–061004–7, 2014.

[29] S. Kou, *Welding metallurgy.* John Wiley Sons, 2003.

[30] J.-P. Kruth, G. Levy, F. Klocke, and T. Childs, "Consolidation phenomena in laser and powder-bed based layered manufacturing," *CIRP Annals-Manufacturing Technology*, vol. 56, no. 2, pp. 730–759, 2007.

[31] S. Basu and T. DebRoy, “Liquid metal expulsion during laser irradiation,” *Journal of Applied Physics*, vol. 72, no. 8, pp. 3317–3322, 1992.

[32] L. E. Criales, Y. M. Arısoy, and T. Özel, “Sensitivity analysis of material and process parameters in finite element modeling of selective laser melting of inconel 625,” *The International Journal of Advanced Manufacturing Technology*, vol. 86, no. 9-12, pp. 2653–2666, 2016.

[33] P. A. A. Khan and T. Debroy, “Alloying element vaporization and weld pool temperature during laser welding of alsl 202 stainless steel,” *Metallurgical Transactions B*, vol. 15, no. 4, pp. 641–644, 1984.

[34] T. DebRoy, P. W. Fuerschbach, X. He, and J. T. Norris, “Understanding metal vaporizaiton from laser welding,” report, Sandia National Laboratories, 2003.

[35] A. Klassen, V. E. Forster, and C. Körner, “A multi-component evaporation model for beam melting processes,” *Modelling and Simulation in Materials Science and Engineering*, vol. 25, no. 2, p. 025003, 2016.

[36] M. I. Khan, A. Pequegnat, and Y. N. Zhou, “Multiple memory shape memory alloys,” *Advanced Engineering Materials*, vol. 15, no. 5, pp. 386–393, 2013.

[37] T. Mukherjee, J. Zuback, A. De, and T. DebRoy, “Heat and fluid flow modeling to examine 3d-printability of alloys,” in *7th International Symposium on High-Temperature Metallurgical Processing*, pp. 471–478, Springer.

[38] P. Solana, P. Kapadia, J. M. Dowden, and P. J. Marsden, “An analytical model for the laser drilling of metals with absorption within the vapour,” *Journal of Physics D: Applied Physics*, vol. 32, no. 8, p. 942, 1999.

[39] Y. Huang, M. B. Khamesee, and E. Toyserkani, “A comprehensive analytical model for laser powder-fed additive manufacturing,” *Additive Manufacturing*, vol. 12, no. Part A, pp. 90–99, 2016.

[40] F. Verhaeghe, T. Craeghs, J. Heulens, and L. Pandelaers, “A pragmatic model for selective laser melting with evaporation,” *Acta Materialia*, vol. 57, no. 20, pp. 6006–6012, 2009.

[41] V. Manvatkar, A. De, and T. DebRoy, “Heat transfer and material flow during laser assisted

multi-layer additive manufacturing," *Journal of Applied Physics*, vol. 116, no. 12, p. 124905, 2014.

[42] V. Manvatkar, A. De, and T. DebRoy, "Spatial variation of melt pool geometry, peak temperature and solidification parameters during laser assisted additive manufacturing process," *Materials Science and Technology*, vol. 31, no. 8, pp. 924–930, 2015.

[43] H. Qi, J. Mazumder, and H. Ki, "Numerical simulation of heat transfer and fluid flow in coaxial laser cladding process for direct metal deposition," *Journal of Applied Physics*, vol. 100, no. 2, p. 024903, 2006.

[44] Y. Lee and W. Zhang, "Mesoscopic simulation of heat transfer and fluid flow in laser powder bed additive manufacturing," in *International Solid Free Form Fabrication Symposium, Austin*, pp. 1154–1165.

[45] K. Alexander, E. F. Vera, and K. Carolin, "A multi-component evaporation model for beam melting processes," *Modelling and Simulation in Materials Science and Engineering*, vol. 25, no. 2, p. 025003, 2017.

[46] H. Zhao and T. DebRoy, "Weld metal composition change during conduction mode laser welding of aluminum alloy 5182," *Metallurgical and materials transactions B*, vol. 32, no. 1, pp. 163–172, 2001.

[47] F. D. Richardson, *Physical chemistry of melts in metallurgy*. Academic Press (Elsevier), 1974.

[48] S. Dushman and J. M. Lafferty, *Scientific foundations of vacuum technique.* New York; London: John Wiley Sons, second edition ed., 1962.

[49] C. L. Yaws, *The Yaws handbook of vapor pressure: Antoine coefficients*. Gulf Professional Publishing, 2015.

[50] W. E. King, H. D. Barth, V. M. Castillo, G. F. Gallegos, J. W. Gibbs, D. E. Hahn, C. Kamath, and A. M. Rubenchik, "Observation of keyhole-mode laser melting in laser powder-bed fusion additive manufacturing," *Journal of Materials Processing Technology*, vol. 214, no. 12, pp. 2915–2925, 2014.

[51] T. Eagar and N. Tsai, “Temperature fields produced by traveling distributed heat sources,” *Welding journal*, vol. 62, no. 12, pp. 346–355, 1983.

[52] J. Dutta Majumdar and I. Manna, “Laser material processing,” *International Materials Reviews*, vol. 56, no. 5-6, pp. 341–388, 2011.

[53] T. Mukherjee, V. Manvatkar, A. De, and T. DebRoy, “Dimensionless numbers in additive manufacturing,” *Journal of Applied Physics*, vol. 121, no. 6, p. 064904, 2017.

[54] A. Raghavan, H. L. Wei, T. A. Palmer, and T. DebRoy, “Heat transfer and fluid flow in additive manufacturing,” *Journal of Laser Applications*, vol. 25, no. 5, p. 052006, 2013.

[55] T. Mukherjee, V. Manvatkar, A. De, and T. DebRoy, “Mitigation of thermal distortion during additive manufacturing,” *Scripta Materialia*, vol. 127, no. Supplement C, pp. 79–83, 2017.

[56] M. Frewin and D. Scott, “Finite element model of pulsed laser welding,” *WELDING JOURNAL-NEW YORK-*, vol. 78, pp. 15–s, 1999.

[57] S. A. Khairallah, A. T. Anderson, A. Rubenchik, and W. E. King, “Laser powder-bed fusion additive manufacturing: Physics of complex melt flow and formation mechanisms of pores, spatter, and denudation zones,” *Acta Materialia*, vol. 108, no. Supplement C, pp. 36–45, 2016.

[58] W. Zhang, G. G. Roy, J. W. Elmer, and T. DebRoy, “Modeling of heat transfer and fluid flow during gas tungsten arc spot welding of low carbon steel,” *Journal of Applied Physics*, vol. 93, no. 5, pp. 3022–3033, 2003.

[59] C. J. Knight, “Theoretical modeling of rapid surface vaporization with back pressure,” *AIAA j*, vol. 17, no. 5, pp. 519–523, 1979.

[60] L. D. Bobbio, R. A. Otis, J. P. Borgonia, R. P. Dillon, A. A. Shapiro, Z.-K. Liu, and A. M. Beese, “Additive manufacturing of a functionally graded material from ti-6al-4v to invar: Experimental characterization and thermodynamic calculations,” *Acta Materialia*, vol. 127, pp. 133–142, 2017.

[61] T. Kirk, E. Galvan, R. Malak, and R. Arroyave, “Computational design of gradient paths in additively manufactured functionally graded materials,” *Journal of Mechanical Design*,

vol. 140, no. 11, 2018.

[62] N. Guo and M. C. Leu, “Additive manufacturing: technology, applications and research needs,” *Frontiers of Mechanical Engineering*, vol. 8, no. 3, pp. 215–243, 2013.

[63] A. du Plessis, C. Broeckhoven, I. Yadroitsava, I. Yadroitsev, C. H. Hands, R. Kunju, and D. Bhate, “Beautiful and functional: a review of biomimetic design in additive manufacturing,” *Additive Manufacturing*, vol. 27, pp. 408–427, 2019.

[64] J. O. Milewski, “Additive manufacturing of metals,” *From Fundamental Technology to Rocket Nozzles, Medical Implants, and Custom Jewelry,*, pp. 134–157, 2017.

[65] T. DebRoy, H. Wei, J. Zuback, T. Mukherjee, J. Elmer, J. Milewski, A. M. Beese, A. d. Wilson-Heid, A. De, and W. Zhang, “Additive manufacturing of metallic components–process, structure and properties,” *Progress in Materials Science*, vol. 92, pp. 112–224, 2018.

[66] X. He, T. DebRoy, and P. Fuerschbach, “Alloying element vaporization during laser spot welding of stainless steel,” *Journal of Physics D: Applied Physics*, vol. 36, no. 23, p. 3079, 2003.

[67] M. Collur, A. Paul, and T. DebRoy, “Mechanism of alloying element vaporization during laser welding,” *Metallurgical Transactions B*, vol. 18, no. 4, pp. 733–740, 1987.

[68] S. Semiatin, V. Ivanchenko, and O. Ivasishin, “Diffusion models for evaporation losses during electron-beam melting of alpha/beta-titanium alloys,” *Metallurgical and Materials Transactions B*, vol. 35, no. 2, pp. 235–245, 2004.

[69] M. I. Khan, A. Pequegnat, and Y. N. Zhou, “Multiple memory shape memory alloys,” *Advanced Engineering Materials*, vol. 15, no. 5, pp. 386–393, 2013.

[70] J. Frenzel, E. P. George, A. Dlouhy, C. Somsen, M.-X. Wagner, and G. Eggeler, “Influence of ni on martensitic phase transformations in niti shape memory alloys,” *Acta Materialia*, vol. 58, no. 9, pp. 3444–3458, 2010.

[71] W. Tang, “Thermodynamic study of the low-temperature phase b19 and the martensitic transformation in near-equiatomic ti-ni shape memory alloys,” *Metallurgical and materials transactions A*, vol. 28, no. 3, pp. 537–544, 1997.

[72] J. Ma, B. Franco, G. Tapia, K. Karayagiz, L. Johnson, J. Liu, R. Arroyave, I. Karaman, and A. Elwany, "Spatial control of functional response in 4d-printed active metallic structures," *Scientific reports*, vol. 7, p. 46707, 2017.

[73] B. Franco, J. Ma, B. Loveall, G. Tapia, K. Karayagiz, J. Liu, A. Elwany, R. Arroyave, and I. Karaman, "A sensory material approach for reducing variability in additively manufactured metal parts," *Scientific reports*, vol. 7, no. 1, pp. 1–12, 2017.

[74] J. Sam, B. Franco, J. Ma, I. Karaman, A. Elwany, and J. Mabe, "Tensile actuation response of additively manufactured nickel-titanium shape memory alloys," *Scripta Materialia*, vol. 146, pp. 164–168, 2018.

[75] I. D. McCue, G. M. Valentino, D. B. Trigg, A. M. Lennon, C. E. Hebert, D. P. Seker, S. M. Nimer, J. P. Mastandrea, M. M. Trexler, and S. M. Storck, "Realizing controlled, shape-morphing metallic components for deployable structures," *Materials & Design*, p. 109935, 2021.

[76] K. Karayagiz, A. Elwany, G. Tapia, B. Franco, L. Johnson, J. Ma, I. Karaman, and R. Aróyave, "Numerical and experimental analysis of heat distribution in the laser powder bed fusion of ti-6al-4v," *IISE Transactions*, vol. 51, no. 2, pp. 136–152, 2019.

[77] P. Promoppatum, S.-C. Yao, P. C. Pistorius, A. D. Rollett, P. J. Coutts, F. Lia, and R. Martukanitz, "Numerical modeling and experimental validation of thermal history and microstructure for additive manufacturing of an inconel 718 product," *Progress in Additive Manufacturing*, vol. 3, no. 1, pp. 15–32, 2018.

[78] B. Schoinochoritis, D. Chantzis, and K. Salonitis, "Simulation of metallic powder bed additive manufacturing processes with the finite element method: A critical review," *Proceedings of the Institution of Mechanical Engineers, Part B: Journal of Engineering Manufacture*, vol. 231, no. 1, pp. 96–117, 2017.

[79] D. Gu and B. He, "Finite element simulation and experimental investigation of residual stresses in selective laser melted ti–ni shape memory alloy," *Computational Materials Science*, vol. 117, pp. 221–232, 2016.

[80] Y. Huang, L. Yang, X. Du, and Y. Yang, "Finite element analysis of thermal behavior of metal powder during selective laser melting," *International Journal of Thermal Sciences*, vol. 104, pp. 146–157, 2016.

[81] S. A. Khairallah, A. T. Anderson, A. Rubenchik, and W. E. King, "Laser powder-bed fusion additive manufacturing: Physics of complex melt flow and formation mechanisms of pores, spatter, and denudation zones," *Acta Materialia*, vol. 108, pp. 36–45, 2016.

[82] L.-E. Loh, C.-K. Chua, W.-Y. Yeong, J. Song, M. Mapar, S.-L. Sing, Z.-H. Liu, and D.-Q. Zhang, "Numerical investigation and an effective modelling on the selective laser melting (slm) process with aluminium alloy 6061," *International Journal of Heat and Mass Transfer*, vol. 80, pp. 288–300, 2015.

[83] Y. Li and D. Gu, "Parametric analysis of thermal behavior during selective laser melting additive manufacturing of aluminum alloy powder," *Materials & design*, vol. 63, pp. 856–867, 2014.

[84] L. Dong, A. Makradi, S. Ahzi, and Y. Remond, "Three-dimensional transient finite element analysis of the selective laser sintering process," *Journal of materials processing technology*, vol. 209, no. 2, pp. 700–706, 2009.

[85] S. Kolossov, E. Boillat, R. Glardon, P. Fischer, and M. Locher, "3d fe simulation for temperature evolution in the selective laser sintering process," *International Journal of Machine Tools and Manufacture*, vol. 44, no. 2-3, pp. 117–123, 2004.

[86] P. Foteinopoulos, A. Papacharalampopoulos, and P. Stavropoulos, "On thermal modeling of additive manufacturing processes," *CIRP Journal of Manufacturing Science and Technology*, vol. 20, pp. 66–83, 2018.

[87] P. Yuan and D. Gu, "Molten pool behaviour and its physical mechanism during selective laser melting of tic/alsi10mg nanocomposites: simulation and experiments," *Journal of Physics D: Applied Physics*, vol. 48, no. 3, p. 035303, 2015.

[88] D. Dai and D. Gu, "Thermal behavior and densification mechanism during selective laser melting of copper matrix composites: Simulation and experiments," *Materials & Design*,

vol. 55, pp. 482–491, 2014.

[89] S. Mohanty and J. H. Hattel, “Numerical model based reliability estimation of selective laser melting process,” *Physics Procedia*, vol. 56, pp. 379–389, 2014.

[90] L. Johnson, M. Mahmoudi, B. Zhang, R. Seede, X. Huang, J. T. Maier, H. J. Maier, I. Karaman, A. Elwany, and R. Arróyave, “Assessing printability maps in additive manufacturing of metal alloys,” *Acta Mater.*, vol. 176, pp. 199–210, 2019.

[91] R. Seede, D. Shoukr, B. Zhang, A. Whitt, S. Gibbons, P. Flater, A. Elwany, R. Arroyave, and I. Karaman, “An ultra-high strength martensitic steel fabricated using selective laser melting additive manufacturing: Densification, microstructure, and mechanical properties,” *Acta Mater.*, vol. 186, pp. 199–214, 2020.

[92] J. C. Steuben, A. J. Birnbaum, J. G. Michopoulos, and A. P. Iliopoulos, “Enriched analytical solutions for additive manufacturing modeling and simulation,” *Additive Manufacturing*, vol. 25, pp. 437–447, 2019.

[93] J.-N. Zhu, E. Borisov, X. Liang, E. Farber, M. Hermans, and V. Popovich, “Predictive analytical modelling and experimental validation of processing maps in additive manufacturing of nitinol alloys,” *Additive Manufacturing*, vol. 38, p. 101802, 2021.

[94] E. J. Schwalbach, S. P. Donegan, M. G. Chapman, K. J. Chaput, and M. A. Groeber, “A discrete source model of powder bed fusion additive manufacturing thermal history,” *Additive Manufacturing*, vol. 25, pp. 485–498, 2019.

[95] P. Honarmandi, R. Seede, L. Xue, D. Shoukr, P. Morcos, B. Zhang, C. Zhang, A. Elwany, I. Karaman, and R. Arroyave, “A rigorous test and improvement of the eagar-tsai model for melt pool characteristics in laser powder bed fusion additive manufacturing,” *Additive Manufacturing*, vol. 47, p. 102300, 2021.

[96] J. Goldak, A. Chakravarti, and M. Bibby, “A new finite element model for welding heat sources,” *Metallurgical transactions B*, vol. 15, no. 2, pp. 299–305, 1984.

[97] L. Xue, K. Atli, S. Picak, C. Zhang, B. Zhang, A. Elwany, R. Arroyave, and I. Karaman, “Controlling martensitic transformation characteristics in defect-free niti shape memory

alloys fabricated using laser powder bed fusion and a process optimization framework," *Acta Materialia*, p. 117017, 2021.

[98] W. E. King, H. D. Barth, V. M. Castillo, G. F. Gallegos, J. W. Gibbs, D. E. Hahn, C. Kamath, and A. M. Rubenchik, "Observation of keyhole-mode laser melting in laser powder-bed fusion additive manufacturing," *J. Mater. Process. Technol.*, vol. 214, no. 12, pp. 2915–2925, 2014.

[99] G. G. Gladush and I. Smurov, *Physics of laser materials processing: theory and experiment*, vol. 146. Springer Science & Business Media, 2011.

[100] H. Haario, E. Saksman, J. Tamminen, *et al.*, "An adaptive metropolis algorithm," *Bernoulli*, vol. 7, no. 2, pp. 223–242, 2001.

[101] P. Honarmandi and R. Arróyave, "Uncertainty quantification and propagation in computational materials science and simulation-assisted materials design," *Integr. Mater. Manuf. Innov.*, pp. 1–41, 2020.

[102] P. Honarmandi, N. H. Paulson, R. Arróyave, and M. Stan, "Uncertainty quantification and propagation in CALPHAD modeling," *Model. Simul. Mater. Sci. Eng.*, vol. 27, no. 3, p. 034003, 2019.

[103] V. Attari, P. Honarmandi, T. Duong, D. J. Sauceda, D. Allaire, and R. Arroyave, "Uncertainty propagation in a multiscale CALPHAD-reinforced elastochemical phase-field model," *Acta Mater.*, vol. 183, pp. 452–470, 2020.

[104] P. Honarmandi, L. Johnson, and R. Arroyave, "Bayesian probabilistic prediction of precipitation behavior in Ni-Ti shape memory alloys," *Comput. Mater. Sci.*, vol. 172, p. 109334, 2020.

[105] P. Honarmandi, T. C. Duong, S. F. Ghoreishi, D. Allaire, and R. Arroyave, "Bayesian uncertainty quantification and information fusion in CALPHAD-based thermodynamic modeling," *Acta Mater.*, vol. 164, pp. 636–647, 2019.

[106] P. Honarmandi, A. Solomou, R. Arroyave, and D. Lagoudas, "Uncertainty quantification of the parameters and predictions of a phenomenological constitutive model for thermally

induced phase transformation in Ni–Ti shape memory alloys," *Model. Simul. Mater. Sci. Eng.*, vol. 27, no. 3, p. 034001, 2019.

[107] P. Honarmandi and R. Arroyave, "Using bayesian framework to calibrate a physically based model describing strain-stress behavior of TRIP steels," *Comput. Mater. Sci.*, vol. 129, pp. 66–81, 2017.

[108] T. C. Duong, R. E. Hackenberg, A. Landa, P. Honarmandi, A. Talapatra, H. M. Volz, A. Llobet, A. I. Smith, G. King, S. Bajaj, *et al.*, "Revisiting thermodynamics and kinetic diffusivities of uranium–niobium with bayesian uncertainty analysis," *Calphad*, vol. 55, pp. 219–230, 2016.

[109] P. Klemens and R. Williams, "Thermal conductivity of metals and alloys," *International metals reviews*, vol. 31, no. 1, pp. 197–215, 1986.

[110] B. E. Franco, *Variability in the Shape Memory and Mechanical Response of Additively Manufactured NiTi*. PhD thesis, 2019.

[111] S. Dushman, "Scientific foundations of vacuum technique," 1949.

[112] A. F2004-17, "Standard test method for transformation temperature of nickel-titanium alloys by thermal analysis," tech. rep., ASTM International, West Conshohocken, PA, 2017. DOI: 10.1520/F2004-17, `https://www.astm.org`.

[113] O. Benafan, G. Bigelow, and D. Scheiman, "Transformation behavior in niti-20hf shape memory alloys–transformation temperatures and hardness," *Scripta Materialia*, vol. 146, pp. 251–254, 2018.

[114] X. Wang and K. Putyera, "Accurate determination of the chemical composition of nickel-titanium binary alloys by nist high performance inductively coupled plasma – optical emission spectroscopy method," in *Shape Memory and Superelastic Technologies Conference (SMST)*, 2015.

[115] O. Benafan, G. Bigelow, A. Garg, R. Noebe, D. Gaydosh, and R. Rogers, "Processing and scalability of nitihf high-temperature shape memory alloys," *Shape Memory and Superelasticity*, pp. 1–57, 2021.

[116] U. M. Dilberoglu, B. Gharehpapagh, U. Yaman, and M. Dolen, "The role of additive

manufacturing in the era of industry 4.0," *Procedia Manufacturing*, vol. 11, pp. 545–554, 2017.

[117] M. Mehrpouya, A. Dehghanghadikolaei, B. Fotovvati, A. Vosooghnia, S. S. Emamian, and A. Gisario, "The potential of additive manufacturing in the smart factory industrial 4.0: A review," *Applied Sciences*, vol. 9, no. 18, p. 3865, 2019.

[118] H. G. Kia, N. Huang, J. P. Spicer, and J. F. Arinez, "Additive manufacturing of a unibody vehicle," July 17 2018. US Patent 10,022,912.

[119] K. Safaei, H. Abedi, M. Nematollahi, F. Kordizadeh, H. Dabbaghi, P. Bayati, R. Javanbakht, A. Jahadakbar, M. Elahinia, and B. Poorganji, "Additive manufacturing of niti shape memory alloy for biomedical applications: Review of the lpbf process ecosystem," *JOM*, pp. 1–16, 2021.

[120] I. Kaur and P. Singh, "State-of-the-art in heat exchanger additive manufacturing," *International Journal of Heat and Mass Transfer*, vol. 178, p. 121600, 2021.

[121] Y. Bellouard, "Material science & engineering," *A*, pp. 582–589, 2008.

[122] C. Haberland, M. Elahinia, J. M. Walker, H. Meier, and J. Frenzel, "On the development of high quality niti shape memory and pseudoelastic parts by additive manufacturing," *Smart materials and structures*, vol. 23, no. 10, p. 104002, 2014.

[123] J. Ma, B. Franco, G. Tapia, K. Karayagiz, L. Johnson, J. Liu, R. Arroyave, I. Karaman, and A. Elwany, "Spatial control of functional response in 4d-printed active metallic structures," *Scientific Reports*, vol. 7, p. 46707, Apr 2017.

[124] B. E. Franco, J. Ma, B. Loveall, G. A. Tapia, K. Karayagiz, J. Liu, A. Elwany, R. Arroyave, and I. Karaman, "A sensory material approach for reducing variability in additively manufactured metal parts," *Scientific Reports*, vol. 7, p. 3604, Jun 2017.

[125] M. Elahinia, N. S. Moghaddam, M. T. Andani, A. Amerinatanzi, B. A. Bimber, and R. F. Hamilton, "Fabrication of niti through additive manufacturing: A review," *Progress in Materials Science*, vol. 83, pp. 630–663, 2016.

[126] S. M. Hashemi, S. Parvizi, H. Baghbanijavid, A. T. Tan, M. Nematollahi, A. Ramazani,

N. X. Fang, and M. Elahinia, “Computational modelling of process–structure–property–performance relationships in metal additive manufacturing: a review,” *International Materials Reviews*, vol. 67, no. 1, pp. 1–46, 2022.

[127] J. Herman and W. Usher, “SALib: An open-source python library for sensitivity analysis,” *The Journal of Open Source Software*, vol. 2, jan 2017.

[128] F. Pedregosa, G. Varoquaux, A. Gramfort, V. Michel, B. Thirion, O. Grisel, M. Blondel, P. Prettenhofer, R. Weiss, V. Dubourg, *et al.*, “Scikit-learn: Machine learning in python,” *Journal of machine learning research*, vol. 12, no. Oct, pp. 2825–2830, 2011.

[129] J. Ma, I. Karaman, and R. D. Noebe, “High temperature shape memory alloys,” *International Materials Reviews*, vol. 55, no. 5, pp. 257–315, 2010.

[130] R. Santamarta, R. Arróyave, J. Pons, A. Evirgen, I. Karaman, H. Karaca, and R. Noebe, “Tem study of structural and microstructural characteristics of a precipitate phase in Ni-rich Ni–Ti–Hf and Ni–Ti–Zr shape memory alloys,” *Acta Materialia*, vol. 61, no. 16, pp. 6191–6206, 2013.

[131] H. Karaca, E. Acar, H. Tobe, and S. Saghaian, “NiTiHf-based shape memory alloys,” *Materials Science and Technology*, vol. 30, no. 13, pp. 1530–1544, 2014.

[132] H. Sehitoglu, Y. Wu, L. Patriarca, G. Li, A. Ojha, S. Zhang, Y. Chumlyakov, and M. Nishida, “Superelasticity and shape memory behavior of NiTiHf alloys,” *Shape Memory and Superelasticity*, vol. 3, no. 2, pp. 168–187, 2017.

[133] T. Umale, D. Salas, B. Tomes, R. Arroyave, and I. Karaman, “The effects of wide range of compositional changes on the martensitic transformation characteristics of nitihf shape memory alloys,” *Scripta Materialia*, vol. 161, pp. 78–83, 2019.

[134] C. Zhang, L. Xue, S. A. Pestka, M. Ranaiefar, K. C. Atli, P. Honarmandi, R. Arroyave, I. Karaman, and A. Elwany, “Processing parameters and martensitic phase transformation relationships in near defect-free 3d printed nitihf smas,” *Manuscript submitted for publication.*, 2022.

[135] P. Honarmandi, R. Seede, L. Xue, D. Shoukr, P. Morcos, B. Zhang, C. Zhang, A. Elwany,

I. Karaman, and R. Arroyave, “A rigorous test and improvement of the eagar-tsai model for melt pool characteristics in laser powder bed fusion additive manufacturing,” *Additive Manufacturing*, vol. 47, p. 102300, 2021.

[136] P. Honarmandi, M. Hossain, R. Arroyave, and T. Baxevanis, “A top-down characterization of niti single-crystal inelastic properties within confidence bounds through bayesian inference,” *Shape Memory and Superelasticity*, vol. 7, no. 1, pp. 50–64, 2021.

[137] N. H. Paulson, E. Jennings, and M. Stan, “Bayesian strategies for uncertainty quantification of the thermodynamic properties of materials,” *International Journal of Engineering Science*, vol. 142, pp. 74–93, 2019.

[138] R. A. Otis and Z.-K. Liu, “High-throughput thermodynamic modeling and uncertainty quantification for icme,” *JOM*, vol. 69, no. 5, pp. 886–892, 2017.

[139] R. E. Jones, F. Rizzi, B. Boyce, J. A. Templeton, and J. Ostien, “Plasticity models of material variability based on uncertainty quantification techniques,” tech. rep., Sandia National Lab.(SNL-NM), Albuquerque, NM (United States), 2017.

[140] F. Rizzi, R. Jones, B. Debusschere, and O. Knio, “Uncertainty quantification in md simulations of concentration driven ionic flow through a silica nanopore. i. sensitivity to physical parameters of the pore,” *The Journal of chemical physics*, vol. 138, no. 19, p. 194104, 2013.

[141] M. C. Kennedy and A. O’Hagan, “Bayesian calibration of computer models,” *Journal of the Royal Statistical Society: Series B (Statistical Methodology)*, vol. 63, no. 3, pp. 425–464, 2001.

[142] M. Mahmoudi, G. Tapia, K. Karayagiz, B. Franco, J. Ma, R. Arroyave, I. Karaman, and A. Elwany, “Multivariate calibration and experimental validation of a 3d finite element thermal model for laser powder bed fusion metal additive manufacturing,” *Integrating Materials and Manufacturing Innovation*, vol. 7, no. 3, pp. 116–135, 2018.

[143] G. Tapia, L. Johnson, B. Franco, K. Karayagiz, J. Ma, R. Arroyave, I. Karaman, and A. Elwany, “Bayesian calibration and uncertainty quantification for a physics-based precipitation model of nickel–titanium shape-memory alloys,” *Journal of Manufacturing Science and*

Engineering, vol. 139, no. 7, 2017.

[144] B. Zhang, R. Seede, L. Xue, K. C. Atli, C. Zhang, A. Whitt, I. Karaman, R. Arroyave, and A. Elwany, “An efficient framework for printability assessment in laser powder bed fusion metal additive manufacturing,” *Additive Manufacturing*, vol. 46, p. 102018, 2021.

[145] L. Murr, “Computer simulation in materials science and engineering,” in *Handbook of Materials Structures, Properties, Processing and Performance*, pp. 1105–1121, Cham: Springer, 2015.

[146] U. Von Toussaint, “Bayesian inference in physics,” *Reviews of Modern Physics*, vol. 83, no. 3, pp. 943–999, 2011.

[147] S. M. Lynch, *Introduction to applied Bayesian statistics and estimation for social scientists*. Berlin: Springer Science & Business Media, 2007.

[148] A. Gelman, J. B. Carlin, H. S. Stern, and D. B. Rubin, *Bayesian data analysis*. Cambridge: Chapman and Hall/CRC, 1995.

[149] D. Foreman-Mackey, D. W. Hogg, D. Lang, and J. Goodman, “emcee: the mcmc hammer,” *Publications of the Astronomical Society of the Pacific*, vol. 125, no. 925, pp. 306–312, 2013.

[150] S.-K. Au, “Connecting bayesian and frequentist quantification of parameter uncertainty in system identification,” *Mechanical systems and signal processing*, vol. 29, pp. 328–342, 2012.

[151] M. Laine, “Github,” 2018.

[152] H. Haario, M. Laine, A. Mira, and E. Saksman, “Dram: efficient adaptive mcmc,” *Statistics and computing*, vol. 16, no. 4, pp. 339–354, 2006.

[153] S. P. Donegan, E. J. Schwalbach, and M. A. Groeber, “Zoning additive manufacturing process histories using unsupervised machine learning,” *Materials Characterization*, vol. 161, p. 110123, 2020.

[154] M. Nematollahi, G. Toker, S. Saghaian, J. Salazar, M. Mahtabi, O. Benafan, H. Karaca, and M. Elahinia, “Additive manufacturing of ni-rich nitihf20: manufacturability, composition, density, and transformation behavior,” *Shape memory and superelasticity*, vol. 5, no. 1,

pp. 113–124, 2019.

[155] G. P. Toker, M. Nematollahi, S. E. Saghaian, K. S. Baghbaderani, O. Benafan, M. Elahinia, and H. E. Karaca, “Shape memory behavior of nitihf alloys fabricated by selective laser melting,” *Scripta Materialia*, vol. 178, pp. 361–365, 2020.

[156] F. Pedregosa, G. Varoquaux, A. Gramfort, V. Michel, B. Thirion, O. Grisel, M. Blondel, P. Prettenhofer, R. Weiss, V. Dubourg, J. Vanderplas, A. Passos, D. Cournapeau, M. Brucher, M. Perrot, and E. Duchesnay, “Scikit-learn: Machine learning in Python,” *Journal of Machine Learning Research*, vol. 12, pp. 2825–2830, 2011.

[157] J. Salvatier, T. V. Wiecki, and C. Fonnesbeck, “Probabilistic programming in python using pymc3,” *PeerJ Computer Science*, vol. 2, p. e55, 2016.

[158] S. Sheikh, M. Ranaiefar, P. Honarmandi, P. Morcos, D. Shoukr, I. Karaman, and R. Elwany, Alaa andd Arroyave, “A physics-based computational framework to predict printability of nickel - titanium alloys,” *Manuscript submitted for publication.*, 2022.

[159] L. D. Bobbio, R. A. Otis, J. P. Borgonia, R. P. Dillon, A. A. Shapiro, Z.-K. Liu, and A. M. Beese, “Additive manufacturing of a functionally graded material from ti-6al-4v to invar: Experimental characterization and thermodynamic calculations,” *Acta Materialia*, vol. 127, pp. 133–142, 2017.

[160] T. Kirk, E. Galvan, R. Malak, and R. Arroyave, “Computational design of gradient paths in additively manufactured functionally graded materials,” *Journal of Mechanical Design*, vol. 140, no. 11, p. 111410, 2018.